The copyright of this thesis vests in the author. No quotation from it or information derived from it is to be published without full acknowledgement of the source. The thesis is to be used for private study or non-commercial research purposes only.

Published by the University of Cape Town (UCT) in terms of the non-exclusive license granted to UCT by the author.

University of Cape Town

The giant LSB galaxy NGC 1512:

A high resolution analysis of the HI, star formation and dark matter in this nearby interacting galaxy.

Roger P. Deane

Supervisor:
Professor Renée C. Kraan-Korteweg

Department of Astronomy
University of Cape Town
Rondebosch
7701
South Africa

Email: deane.roger@gmail.com

November 28, 2008

University of Cape Town

A dissertation submitted to the University of Cape Town in partial fulfillment of the requirements for the degree of Master of Science, as part of the National Astrophysics and Space Science Programme

To my brother, the first to inspire me to look up at the stars

and

in memory of Prof. Tony Fairall, who convinced me to sign up for a first year undergraduate astronomy course. I will always aim to be the great ambassador for astronomy that he was.

University of Cape Town

Abstract

This thesis presents high resolution HI synthesis data of the nearby (10 Mpc), interacting, low surface brightness galaxy NGC 1512. The galaxy was observed with the Australia Telescope Compact Array for a total of 85 hours on source. Similar sensitivities for the full range of spatial resolutions was achieved by scaling the observation time for the extended antenna configurations appropriately. The HI data products are compared with the GALEX Nearby Galaxy Survey (NGS) and Spitzer Infrared Nearby Galaxy Survey (SINGS) observations.

The GALEX imaging shows recent star formation in the extended 100 kpc HI disk. The sub-kpc resolution of the datasets allows the use of a pixel-by-pixel analysis to probe local conditions for star formation throughout the galaxy. Low star formation efficiencies are found in the outer disk, consistent with its low surface brightness nature in optical wavelengths.

The discovery of a (tidal?) dwarf galaxy is reported as well as low column density HI features, the origin of which is likely attributable to the rich group environment in which NGC 1512 is embedded, as mapped by HIPASS. Furthermore a rotation curve and mass model is derived showing the galaxy is dark matter dominated, consistent with the properties of giant low surface brightness galaxies.

University of Cape Town

Preface

This thesis describes work carried out at the Department of Astronomy of the University of Cape Town between September 2007 and September 2008. This work was funded by a Master of Science scholarship from the South African Square Kilometre Array project. This scholarship is seeded from the SA SKA Human Capital Development Programme. Additional funding was received from the National Astrophysics and Space Science Programme.

I would like to express my sincere gratitude to my supervisor, Prof. Renée Kraan-Korteweg. Her support and guidance has been instrumental not only in this project, but my entire astronomical career to date.

I am deeply indebted to Ed Elson for teaching me the 'dark art' of radio interferometry data reduction and paving the way for UCT radio astronomy students, present and future.

I would like to acknowledge Dr Vince McIntyre who performed the majority of the observations of NGC 1512 over a 10 year period with the ATCA.

To my parents who have given me every opportunity I could have hoped for. May the tides turn and the sun be warm on your backs.

Finally, to my darling Tess: your love and support gave me every ounce of fortitude needed to finish this. Thank you.

University of Cape Town

University of Cape Town

University of Cape Town

List of Figures

University of Cape Town

University of Cape Town

List of Tables

University of Cape Town

Chapter 1

Introduction

1.1 Project Background

'The HI Nearby Galaxy Survey' (THINGS, Walter et al. 2008) is a high resolution survey of HI emission in 34 nearby galaxies using the NRAO[1] Very Large Array (VLA). The VLA is Y-configuration radio interferometer with 27 antennas, each of 25 metre diameter. The THINGS southern sky extension includes a further 6 galaxies using the Australia Telescope Compact Array (ATCA) with very similar resolutions. The ATCA is a 6 antenna East-West configuration interferometer. Each telescope has a diameter of 22 metres. Utilising these two world class instruments, THINGS aims to study a representative sample of galaxies of varying morphology, star formation rate, HI mass, total luminosity, and metallicity (Walter et al., 2008). The southern sky extension is needed to enhance this representative sample.

NGC 1512, one of the 6 southern galaxies, is the focus of this study. It is a nearby (9.8 Mpc) low surface brightness galaxy (LSB) with Hubble type SB(r)ab. Previous single dish radio observations detected a massive ($\sim 10^{10}$ $M_{\odot}$) HI halo over the comparatively small, optical component (Hawarden et al., 1979). The HI halo appears to extend ~100 kpc in diameter, significantly larger than the estimated 11 kpc Holmberg radius. Hawarden et al. (1979) report a mass-to-light ratio, $(M/L_B) = 31$. This massive HI halo is thought to be a quiescent structure, much like the Malin 1 galaxy (Bothun et al. (1987). Discovered serendipitously, Malin 1 is one of the most HI-massive galaxies known to date ($M_{\rm HI} \sim 10^{11}$ $M_{\odot}$, Bothun et al. 1987). It is a giant low surface brightness galaxy with a HI mass-to-light ratio, $(M_{\rm HI}/L)_B \sim 3$ (Impey and Bothun, 1989). Despite its large fuel supply

[1]The National Radio Astronomy Observatory is a facility of the National Science Foundation operated under cooperative agreement by Associated Universities, Inc.

for star formation, Malin 1 exhibits a low surface brightness stellar disk, below the sky noise level. Furthermore, Malin 1 reveals a 'normal' stellar bulge. This presents a challenge to galaxy evolution models as to (1) why such a large quantity of HI gas has not collapsed to form stars, and (2) how such an extended galactic disk could have formed, as shown by the simulations of D'Onghia et al. (2006). NGC 1512 displays similar properties to Malin 1, however is approximately 33 times closer. It therefore presents an opportunity to explore the implications giant LSB galaxies have on galaxy evolution models in further detail.

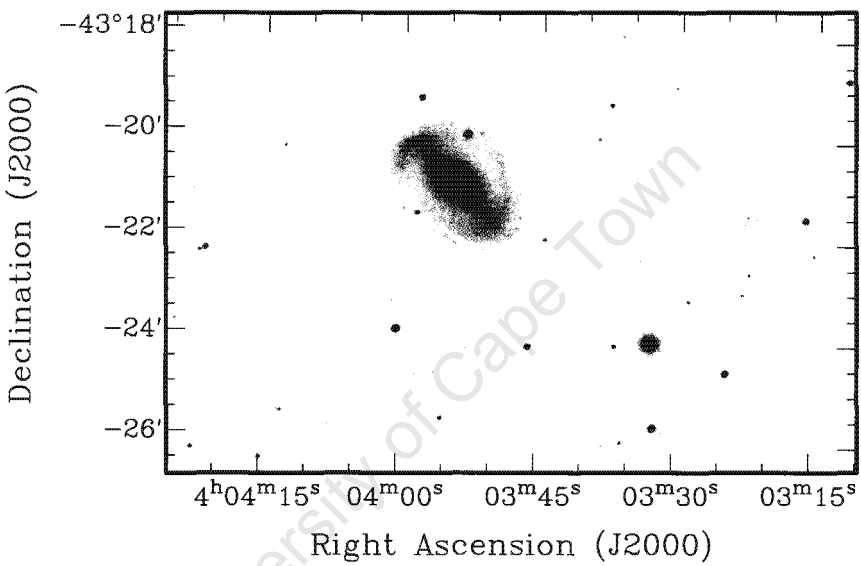

University of Cape Town

Figure 1.1: *R* band image showing NGC 1512 (classification: SB(r)ab) and its ringed structure. Neighbouring galaxy NGC 1510 (dE or BCD) is seen to the south west. The projected distance between the two galaxies is $\sim$ 14 kpc.

NGC 1512 has also been observed by the Galaxy Evolution Explorer space telescope (GALEX), which operates at ultraviolet wavelengths. These observations formed part of the GALEX Nearby Galaxy Survey (NGS). The survey imaged 1034 nearby galaxies in two ultraviolet bands to probe the star formation properties in the local Universe. The NGC 1512 images display strong ultraviolet (UV) emission in the spiral arms (see Fig. 3.1), indicating that very recent star formation has taken place in the extended HI disk (Gil de Paz et al., 2007). This recent star formation is inconsistent with the quiescent HI halo described by previous radio observations. As a case study, this work aims to address the following question: What change in conditions has led to this recent star formation in this hitherto quiescent, extended gas reservoir?

NGC 1512 has an optically disconnected companion galaxy, NGC 1510, seen in the south-west of the R band Digitized Sky Survey[2] map in Fig. 1.1. The two galaxies are separated by an angular scale of 5', corresponding to $\sim$ 14 kpc at the projected distance of NGC 1512 (9.8 Mpc). The two galaxies have very similar recession velocities ($\sim$ 900 km s^{-1}). The high resolution HI data will probe the effect of this companion on NGC 1512's extended HI disk and perhaps provide insight on the cause of the recent star formation activity in both galaxies.

In the following introductory sections the properties and science objectives of THINGS are briefly described, followed by a review on the current understanding of low surface brightness galaxies; rotation curve derivation and mass modeling; and finally the determination of star formation rates.

1.1.1 The HI Nearby Galaxy Survey

The intrinsically low surface brightness of the neutral hydrogen emission line means that high resolution HI imaging requires a great expense in telescope time. Early observations using single dish instruments, with spatial resolutions of order 10' (dish diameter $\sim$ 100 metres), only allowed global statements to be made of galaxies beyond $\sim$ 5 Mpc (Walter et al., 2008).

The advent of aperture synthesis arrays increased the detail to which the radio sky can be studied dramatically. Contributing to this were major surveys performed by the VLA[3] and Westerbork Synthesis Radio Telescope (WSRT)[4] to name just two of the new major facilities of the 1970's (see Hogeveen (1990) for a discussion on the original science objectives of WSRT, which did not include HI imaging as the signal was thought to be too weak.)

The major trade-off with these interferometric instruments is that of brightness sensitivity and spatial resolution. Using a fixed number of receiving elements N, one can increase the brightness sensitivity by using a compact configuration. However, spatial resolution is determined by the interferometer's longest baseline (distance between two receiving elements) resulting that compact configurations

[2]The Digitized Sky Survey was produced at the Space Telescope Science Institute under U.S. Government grant NAG W-2166. The images of these surveys are based on photographic data obtained using the Oschin Schmidt Telescope on Palomar Mountain and the UK Schmidt Telescope. The plates were processed into the present compressed digital form with the permission of these institutions.

[3]*http://www.vla.nrao.edu/*

[4]*http://www.astron.nl/p/WSRT2.htm*

University of Cape Town

have lower spatial resolution. Increasing the baseline length decreases the filling factor,[5] and hence brightness sensitivity, with N receiving elements (Holdaway and Helfer, 1999). By doubling the longest baseline of an interferometer, the observation length must be four-fold to achieve equal sensitivity. This square relationship between spatial resolution and brightness sensitivity (Wrobel and Walker, 1999) limits sensitive ($1\sigma < 5$ mJy), high resolution (< 20") HI observations for a representative number of nearby galaxies.

THINGS aims to address the lack of *sub-kiloparsec* HI imaging by performing homogeneous observations of galaxies in the range $2 < D < 15$ Mpc. These high resolution data are combined with the Spitzer Infrared Nearby Galaxies Survey and the GALEX Nearby Galaxy Survey to probe an array of questions at small spatial scales. The main science goals of THINGS are:

University of Cape Town

- **Star Formation Thresholds**
  The multi-wavelength data of comparable, sub-kpc resolution enable a comparison of local star formation conditions across a wide range of Hubble type. Using star formation recipes and kinematic data products, theoretical predictions can be compared with observed star formation rates and hence the relative importance of local and global conditions quantified (Leroy et al., 2008; Bigiel et al., 2008).

- **Galaxy Mass Distribution**
  The high spatial and spectral resolution kinematic measurements allow the derivation of well sampled rotation curves. Combining these with Spitzer maps enables a study of the dark matter halo distribution as a function of Hubble type, as well as high resolution probe into the highly debated 'core-cusp' discrepancy at the centre of galaxies, leading to greater insight on the validity of the ΛCDM model (Navarro et al., 1996) on galactic scales (de Blok et al., 2008).

- **ISM Energy Budget**
  Super-giant HI shells likely resulting from supernovae explosions allow a measurement of the associated energy release across a large range in Hubble type. Combining this with available multi-wavelength data permits an estimation on secondary star formation resulting from supernovae events, the

[5]Filling factor is defined as the combined collecting area of all individual receiving elements divided by the area of a hypothetical single receiving element that would have a diameter equal to the longest baseline

combination of which allows an approximation on the energy budget of the ISM (Bagetakos et al., 2007; Brinks et al., 2007).

- **ISM Composition**
  The similar resolutions of THINGS and Spitzer observations will enable a comparison of the spatial distributions of gas and dust for the same broad range of Hubble types (Walter et al., 2007).

The data products generated in this thesis will enable an investigation of two of the major THINGS science goals: the kinematics and mass modeling of the galaxy; followed by a *sub-kpc* star formation rate surface density analysis. The former will dissect the mass composition of this giant low surface brightness galaxy candidate; while the latter will probe the cause of the recent star formation evident in ultraviolet images.

University of Cape Town

1.1.2 Low Surface Brightness Galaxies

Historical Perspective

A population of so-called low surface brightness galaxies (LSBs) exists below the optical night sky brightness level. The idea that sky brightness level could significantly influence our view of the extragalactic sky was first proposed by Disney (1976). LSBs are galaxies with faint, dispersed stellar disks and a central surface brightness that lie below the Freeman central surface brightness. Freeman (1970) found this parameter to be constant with low dispersion around the value $SB_{0,B}$, of 21.65 ± 0.30 mag arcsec^{-2}, leading to the so-called Freeman's Law (1970). The exclusion of such LSBs from early galaxy catalogues was purely a selection effect of apparent magnitude limits and isophotal diameter limited galaxy catalogues (Bothun et al., 1997), the effect predicted by Disney's 1976 *Letter to Nature*. This paradigm shift sparked major searches for LSB objects shortly thereafter.

Deep photographic surveys of the nearby Virgo cluster began to show that a distinct class of LSB objects existed (Binggeli et al., 1984; Sandage et al., 1985). Impey and Bothun extended these surveys in collaboration with David Malin to search for even lower surface brightness objects than detected at that point in time. To achieve this Malin developed a photographic amplification process known as 'Malinization' (Bothun et al., 1986). This lead to the discovery of the most famous low surface brightness galaxy to date: Malin 1 (Bothun et al., 1987).

Further innovation by Impey et al. (1996) utilised an Automated Plate Machine (APM) to search for LSBs in the UK Schmidt Sky Survey. This resulted in the

discovery of 693 LSBs - a significant increase in the total population. The results of these surveys have provided strong evidence that LSBs make up to 50% of the general galaxy population.

General Properties

Figure 1.2 taken from McGaugh et al. (1996) shows the space density of galaxies as a function of central surface brightness including data from surveys designed to detect LSBs. The parabola represents Freeman's Empirical Law in the B band, while the horizontal straight line is a fit on the flat distribution from the bright end cutoff of 21.65 mag arcsec^{-2} through to the sky background limit in the B band. This plot illustrates the severity of the selection effects that led to the 'discovery' of Freeman's Law. There appears to be no dependence of galaxy mass or size with central surface brightness (O'Neil et al., 1997), which, when combined with Fig. 1.2, leads to the conclusion that LSBs could make up a significant percentage of the total baryonic content of the Universe (Impey and Bothun, 1997).

University of Cape Town

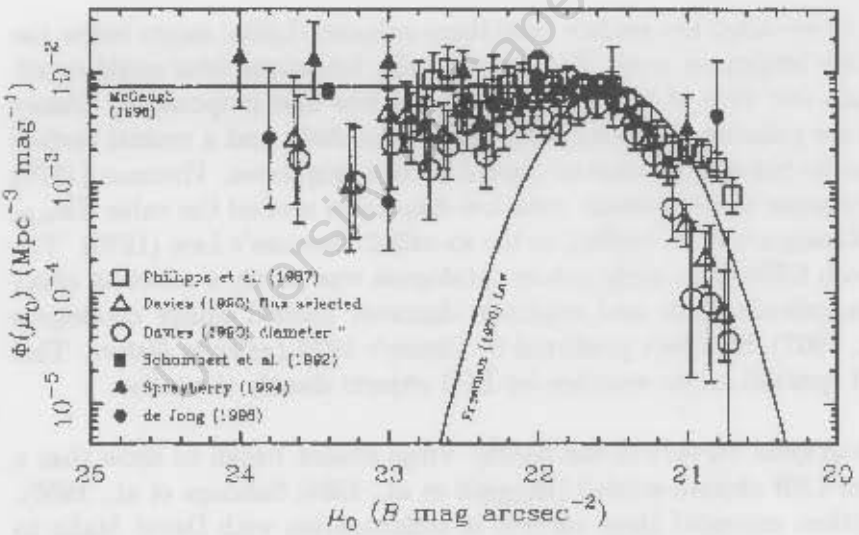

Figure 1.2: Space density of galaxies as a function of central surface brightness reproduced (McGaugh et al. 1996). The solid line indicates the surface brightness distribution as found by Freeman for 'normal' spiral galaxies. The near horizontal line is a fit to the LSB population.

The frequent misconception that LSBs are low mass objects is debunked by the HI velocity widths (and hence dynamical masses) reported in Schombert et al. (1992) which are not distinguishable from high surface brightness (HSB)

galaxies. The total HI content is not unlike those of HSBs, despite the trend that LSB HI surface densities are lower (van der Hulst et al. 1992). However, LSBs are observed to be more gas rich than HSBs for a fixed luminosity. This is linked the finding that LSBs are considerably dark matter dominated (de Blok and McGaugh, 1997a), resulting in the high dynamic stability of the disk. This stability allows the low surface densities in the disk, however hinders star formation as it is more difficult for gas clouds to collapse. The low star formation rate is further accentuated by the lack of chemical enrichment over time, which facilitates gas cooling (de Blok and van der Hulst, 1998).

This moderate chemical enrichment rate is validated in the failure of a number of studies to detect CO (both 2-1 and 1-0) in LSB disks (Schombert et al., 1990; Knezek, 1993). Despite these severely hampered conditions for star formation, the vast majority of the LSB population curiously enough are blue (McGaugh and Bothun, 1994). This paradox is explained by considering that LSBs only have a faint, old population which is not well-developed due to a low star formation history (O'Neil et al., 1997). It follows that LSBs would only need a small number of blue stars to affect the galaxy colour (de Blok, 1997). A lack of a correlation of surface brightness with colour (McGaugh and Bothun, 1994) rules out the possibility that LSBs could be 'faded out' HSBs, galaxies where massive, and hence highly luminous star formation has ceased, resulting in a low surface brightness appearance.

HI aperture synthesis observations of LSBs have shown the dark matter dominance discussed above to be prevalent at almost all radii (Pickering et al., 1997). The mass models derived in these studies suggest that LSB dark matter halos have a lower density and greater extent than that of HSBs, as investigated in Zwaan et al. (1995). Despite these differences, dark matter halos appear to have equivalent dynamical masses (Bothun et al., 1997).

University of Cape Town

1.1.2.1 Giant Low Surface Brightness Galaxies

Combining all the reviewed properties of LSB galaxies strongly suggests that these objects are amongst the least evolved objects in the nearby Universe. A subset of the LSB population are the so-called *giant Low Surface Brightness Galaxies (gLSBs)*. The properties of a sample of these objects are well documented in Sprayberry et al. (1995) and Knezek (1999). The most significant differences from 'normal' counterparts is that giant LSBs have a gas component of greater mass ($M_{\rm HI} > 10^{10}$ $M_\odot$) and extent. This makes them interesting objects to study as case studies for galaxy evolution models.

A prime example is the discovery of the previously discussed Malin 1 galaxy (Bothun et al., 1987) with an HI mass $M_{\rm HI} \sim 10^{11}$ M$_\odot$. The galaxy has a central surface brightness of 25.5 mag arcsec^{-2} and scale length of 55 kpc in the B band. This presented a challenging problem to galaxy evolution models in that such a large reservoir of gas had not collapsed to form a larger quantity of stars. It appeared that 'normal' galaxy formation processes had created a stellar bulge, but no stellar disk (Bothun et al., 1987). Subsequent investigation using the Hubble Space Telescope revealed a normal stellar disk (Barth, 2006) with an extended HI halo likely due to a merger event with a gas rich galaxy.

The galaxy in the current study, NGC 1512 although not quite as massive, has comparable properties to Malin 1. The earlier observations of NGC 1512 (Hawarden et al., 1979) reveal a galaxy similar to Malin 1 in its HI/optical morphology. However, NGC 1512 has the advantage of being approximately 33 times closer. A Schmidt plate with overlaid HI contours is shown in Fig. 1.3 (Hawarden et al., 1979). The HI contours are heavily affected by the large beam size. The HI extent of the $N_{\rm HI} = 10^{19}$ cm^{-2} column density contour is approximately 100 kpc. The comparatively small optical component makes this object intruiging and it appears to have the highly unevolved characteristics of giant LSBs, given the HI mass measured by Hawarden et al. (1979) of 1.1×10^{10} M$_\odot$ and ratio of HI mass to blue luminosity $(M_{\rm HI}/L_B) = 1.4 \pm 0.3$ (cf. Warmels. 1988, Bothun et al. 1988).

Cosmological Significance

Exclusion of such a galaxy population has effects on inferred cosmological parameters. Exclusion of LSBs results in a poorer sampling of the large scale structure of the Universe and therefore any inferred cosmological models based on the measured galaxy clustering. This is particularly relevant in light of the findings of the Mo et al. (1994) and Bothun et al. (1993) that LSBs are not typically found in virialised regions. This leads to significantly less clustering of LSBs on scales $< 3{h_{70}}^{-1}$ Mpc. O'Neil et al. (1997) find LSBs to be located preferentially near the edge of the associated group or cluster, providing independent evidence that these are likely to be unevolved objects. LSBs are not normally found in voids (Bothun et al., 1992). They appear to follow the HSB large-scale structure distribution, with however a slightly weaker correlation (Basilakos et al., 2007). Furthermore, LSBs tend to be more isolated from their nearest neighbour (Bothun et al., 1993).

The above findings offer the speculative evidence that LSBs form in lower density perturbations of the early Universe's energy-density field. This is further supported by the characteristics, described in the previous section, that LSB dark

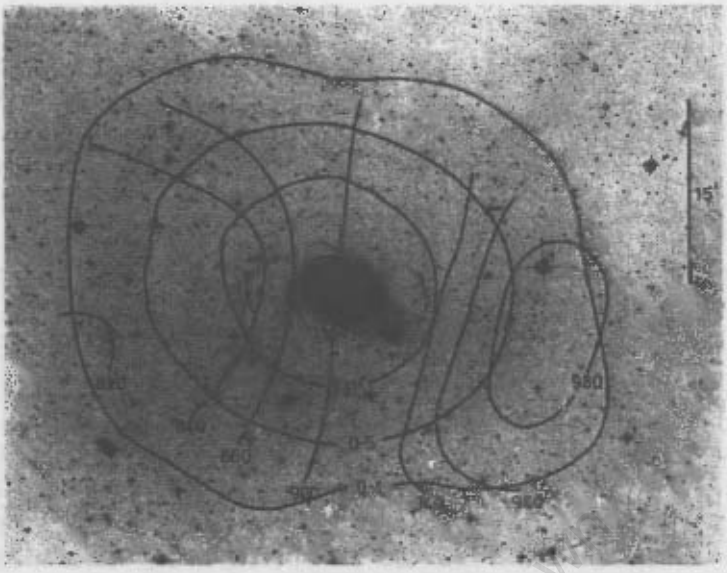

Figure 1.3: Copy of Fig. 3 in Haywarden et al. (1979) showing HI column density and iso-velocity contours of NGC 1512 superimposed on a reproduction of a highly saturated Schmidt plate. The column density contours are in units of of 10^{20} atoms cm^{-2} and the iso-velocity contours are in units of km s^{-1}. The Parkes half power beam width (15') is shown on the right of the map.

matter halos are of lower density and greater spatial extent.

1.1.3 Rotation Curves and Galaxy Mass Modeling

Historical Perspective

The current cosmological concordance model attributes 23% of the energy-density of the Universe to Dark Matter (Spergel et al., 2007). No direct detections of this enigmatic 'missing mass' have been successful, however its gravitational interaction with baryonic matter is frequently observed. The effect of Dark Matter on cluster dynamics was originally inferred by Fritz Zwicky when he derived the dynamical mass of the Coma cluster, yielding an average galaxy mass significantly larger than expected (Zwicky, 1937).

Since the determination of the earliest galaxy rotation curves (Bosma, 1978; Rubin et al., 1978) it has become clear that there is a substantial amount of 'missing mass' associated with *individual* galaxies. Galaxy rotation curves tend to rise to a maximum rotation velocity and remain flat towards the outskirts of the observed baryonic distribution. This implies a great deal more mass outside of the stellar observations.

University of Cape Town

This inferred 'missing mass', or dark matter, has subsequently become a fundamental component in the collisionless Cold Dark Matter framework (ΛCDM), an extraordinary achievement of modern cosmology describing the large and small scale structure of the Universe (Navarro et al., 1996). Problems remain however, in that observations and theory do not agree on the dark matter distribution within a halo at large and small radii, particularly for dwarf and LSB galaxies (de Blok et al., 2008); as well as the on the much debated 'missing satellite' discrepancy (Moore et al., 1999).

Current Status

Rotation curves vary substantially as a function of the stellar and gas content of a galaxy (de Blok et al., 2008). High surface brightness galaxies typically show steeply rising rotation curves as a result of the high density of stellar material in the centre. Low surface brightness galaxies show slowly rising rotation curves, indicative of their low stellar density (Rubin et al., 1978). It is for this reason that LSBs have been used extensively in rotation curve analyses due to their small stellar component and hence lower associated uncertainty with the final mass model. This galaxy population is usually rich in HI gas and their rotation curves derived using HI synthesis observations. This is considerably less challenging than an optically derived rotation curve due to the low surface brightness of the stellar disk and the limited Hα emission associated with LSBs.

Despite its resolution limitations, HI appears to be the tracer of choice to measure high fidelity rotation curves for a number of reasons:

- The HI distribution is usually greater in extent than the optical/IR (Broeils and Rhee, 1997) enabling the associated dark matter halo to be modelled to larger radii.

- HI emission usually fills the entire extent of the disk with a relatively large filling factor, and therefore producing a well sampled velocity field. This decreases the sensitivity to non-circular motions when compared with H_α velocity field determinations (de Blok et al., 2008).

- The emission is unobscured by dust (particularly relevant to the core-cusp discrepancy in the centre of galaxies).

- The dynamical centres of galaxies can be determined independently of, and compared with the optical centres (de Blok et al., 2008).

University of Cape Town

- Atomic hydrogen retains signatures of its dynamical history for long timescales due to its low mass (Morganti et al., 2003).

One of the most recent galaxy rotation curve analyses using HI is the work of de Blok et al. (2008). Rotation curves have been derived for 19 of the 34 galaxies included in the THINGS sample. This represents the largest sample of high resolution rotation curves for a set of homogeneously observed, reduced and analysed galaxies. One of the main aims of de Blok et al. (2008) is to probe the core-cusp discrepancy and to enable the investigation of the effect of non-circular motions (Oh et al., 2008), triaxiality and galaxy centre determinations (Trachternach et al., 2008) on galaxy mass modeling and the implication thereof on the ΛCDM framework.

The current study will study the kinematics of NGC 1512 with the primary aim of determining the presence and effect of an interaction with the neighbouring galaxy NGC 1510. The mass model will give an approximation of the contribution of each mass component (gas, stars, dark matter) towards the total mass budget. Both of these results will add significantly to the understanding of the NGC 1512 system.

University of Cape Town

1.1.4 Star Formation

Star formation lies at the heart of galaxy evolution. It is fueled by gas and thus controls the gas content in galaxies. This can be a slow transition with passively evolving objects (e.g. LSBs), or rapid as in starburst galaxies where significant composition changes can occur on a timescales < 1 Gyr. Star formation converts the galaxy's gas reservoir into heavier elements through nuclear fusion and supernovae explosions. These heavier elements are expelled into the interstellar medium through stellar winds, planetary nebulae and supernovae. Through this gas consumption star formation regulates the enrichment of the interstellar medium. This enrichment enables more efficient cooling in collapsing gas clouds. This enhances subsequent star birth if a sufficient gas reservoir is available. The rate and manner in which galaxies evolve is therefore driven by the star formation rate throughout their lifetime.

Star formation rates have been determined in a wide range of wavelength regimes, from radio to X-ray. Commonly used indicators include:

- **Radio continuum** – the primary contribution in this wavelength regime is synchroton emission, originating from particles accelerated by supernovae explosions and spiralling in large-scale magnetic fields causing them to radiate.

- **CO molecular line emission** – giant molecular clouds, which make up a large percentage of the interstellar medium, are the immediate precursor to star formation.
- **Thermal infrared emission** – starlight absorbed by dust grains (which is more efficient at blue and UV wavelengths) and re-radiated in the mid-to-far infrared.
- **Recombination lines** – e.g. Balmer, characteristic of HII regions around hot stars.
- **Ultraviolet continuum emission** – direct photospheric emission from O and early B type stars peak in the ultraviolet regime.

The majority of star formation rate indicators trace hot, young massive stars (directly or indirectly), a population which by the stellar age-mass relation would only be present if significant recent (< 100 Myr) star formation has taken place. The conversion of this *massive* SFR to a total SFR requires an assumption of the stellar initial mass function (IMF) (Calzetti, 2008).

This large range of SFR indicators is primarily due to the asynchronous improvements of instruments of differing frequency coverage. As these improvements open new galaxy population parameter spaces, methods to derive the SFR for these are developed and the corresponding uncertainties defined (Calzetti, 2008). This suite of different SFR recipes combined with new facilities (e.g., SKA, ALMA, JWST, Herschel, LSST, LMT) will lead to SFR determinations of ground-breaking sensitivity and spatial resolution for a vast range of the electromagnetic spectrum. This allows the cross-calibration of many of the SFR tracers over an extensive redshift range, thus measuring the star formation rate for a large number of galaxy populations as well as their evolution (Calzetti, 2008).

Although the aforementioned facilities are a number of years from construction and commissioning, there has recently been a dramatic increase in high quality data for nearby galaxies. The GALEX Nearby Galaxy Survey (Gil de Paz et al., 2007), Spitzer SINGS (Kennicutt et al., 2003), BIMA Survey of Nearby Galaxies (Helfer et al., 2003) and THINGS (Walter et al., 2008) combine to form an ultraviolet, infrared, millimetre and radio view of a representative sample of nearby galaxies at comparable sensitivities and spatial resolutions. Sensitive observations at sub-kiloparsec scales have been scarce before the above surveys owing particularly to the expense in telescope time for the HI and CO data (Walter et al., 2008; Bigiel et al., 2008). These datasets enable the study of star formation on 'local' scales. 'Local' implies that the galaxy is significantly resolved, unlike the

total integrated flux that make up the majority of the literature.

This study will make use of data from three of these surveys: the ultraviolet, infrared and HI observations. The UV and mid-IR are combined to trace direct photospheric emission from young O and early B type stars, as well as thermal emission from dust which has absorbed predominantly UV and B band photons. The method is described in Chapter 3. The results are compared with the gas distribution in Chapter 5.

1.2 Project Objectives

The primary objective of this thesis is the detailed HI study of NGC 1512. This includes the complete data reduction of ~85 hours on source with ATCA. The high spatial (6") and velocity (3.5 $\mathrm{km\,s^{-1}}$) resolution enable a range of HI data products of substantial detail which will allow the attempt to answer the questions posed about this enigmatic galaxy. These HI data products allow the kinematics of the NGC 1512 system to be modeled. This will provide insight into the presence (and strength) of an interaction, as well as an estimate on the dark matter dominance – which is critical to the theory of formation and evolution of low surface brightness galaxies.

Combining the relevant data sets from the different wavelength regimes, conditions for star formation as a function of HI surface density will be investigated on a sub-kpc scales, as well as its relation to galactocentric radius. This will provide clues for the recent star formation in this hitherto quiescent HI disk.

Ultimately, the aim is to classify NGC 1512 in relation to a 'typical' giant LSB galaxy. This will require a synthesis of all the various analyses quoted above.

1.3 Thesis Outline

Chapter 2 details the HI synthesis data reduction techniques. It presents the derived data products and puts these into context with both the optical and previous single dish radio observations.

Chapter 3 presents further multi-wavelength data used in this study. It will detail the recipe used to generate the star formation rate surface density maps as this is a relatively new multi-wavelength technique to trace both obscured and unobscured star formation.

University of Cape Town

Chapter 4 discusses the methodology used to derive the observed rotation curve from the velocity field, as well as the contributions to this from the total gas and stellar content. These observables are used to fit a pseudo isothermal dark matter halo distribution which allow a description of the mass components of the system.

Chapter 5 utilises a multi-wavelength approach to investigate HI conditions for star formation in NGC 1512. Local star formation conditions are probed using a pixel-by-pixel technique corresponding to spatial scales of 760 pc. Dependencies of the star formation rate and efficiency with galactocentric radius are investigated by binning the data points into radial annuli.

Chapter 6 broadens the study by considering the local environment of NGC 1512 using data from the HI Parkes All Sky Survey (HIPASS). Neighbouring galaxy morphologies are discussed in speculation of previous interactions. The HIPASS detection of NGC 1512 (15' resolution) is compared with the 17" THINGS observations in search of additional low column density HI features. Furthermore, the validity of the Tidal Dwarf Galaxy candidate is explored.

Chapter 7 presents a summary of all results derived in this case study. It outlines future observations and analysis planned to further probe the history of this enigmatic galaxy.

University of Cape Town

Chapter 2

HI Synthesis Observations and Data Reduction

As introduced in Chapter 1, NGC 1512 is an interesting galaxy due to a number of its distinctive properties. Higher resolution HI observations will provide a more detailed view of the extended disk morphology and kinematics. This will aid in the interpretation of NGC 1512's history and interaction with the companion galaxy NGC 1510.

This chapter will detail the observations and reduction of the HI synthesis data obtained with the ATCA. Chapter 3 will present additional multi-wavelength data used in the rotation curve and star formation analyses.

University of Cape Town

2.1 Observations

Table 2.1 summarizes the radio observations of NGC 1512. A total of 13 separate runs were performed on the Australia Telescope Compact Array (ATCA) between September 1996 and July 2007. The array configurations included the 210, 375, 750A, 1.5A/B, 6B/C arrays providing large range in *uv* coverage.

Two of the archival runs were not incorporated (nor included in Table 2.1) because of an incorrect observing frequency used for the secondary calibrator and leading to an incorrect calibrator flux levels. The latter possibly occurred because the observations were performed during maintenance time. Four of the usable eleven runs were obtained as part of the THINGS proposal. Three of these are in the longest baseline configurations (6 km) possible with the ATCA. To achieve comparable sensitivity at both low and high spatial resolutions a great deal of observing time was spent in the long baseline configurations (see Table 2.1).

TABLE 2.1: ATCA OBSERVATION SUMMARY

1 Array	2 Project	3 Date	4 Start h m	5 End h m	6 Duration hrs	7 Cal.	8 Flux Jy	9 RA (J2000) h m s	10 Dec (J2000) ° ' "	11 Bandwidth MHz	12 N_{chan}	13 ΔV km s^{-1}	14 ν_{centre} MHz
210	C570	2000-07-06	17 16	23 09	4.36	0438-436	4.45	04 04 35.28	-43 13 32.6	8.0	512	3.304	1415
								04 04 35.28	-43 28 32.6				
								04 03 12.72	-43 28 32.6				
								04 03 12.72	-43 13 32.6				
375	C570	1996-09-23	11 47	21 02	6.65	0438-436	4.65	04 04 35.28	-43 13 32.6	8.0	512	3.304	1415
								04 04 35.28	-43 28 32.6				
								04 03 12.72	-43 28 32.6				
								04 03 12.72	-43 13 32.6				
375	C570	1996-09-24	11 51	22 48	7.26	0438-436	4.64	04 04 35.28	-43 13 32.6	8.0	512	3.304	1415
								04 04 35.28	-43 28 32.6				
								04 03 12.72	-43 28 32.6				
								04 03 12.72	-43 13 32.6				
375	C570	1996-12-03	13 37	19 28	4.20	0438-436	4.74	04 04 35.28	-43 13 32.6	8.0	512	3.304	1415
								04 04 35.28	-43 28 32.6				
								04 03 12.72	-43 28 32.6				
								04 03 12.72	-43 13 32.6				
750A	C570	1996-11-06	09 18	21 04	7.94	0438-436	4.64	04 04 35.28	-43 13 32.6	8.0	512	3.304	1415
								04 04 35.28	-43 28 32.6				
								04 03 12.72	-43 28 32.6				
								04 03 12.72	-43 13 32.6				
1.5A	C570	1996-10-20	11 03	22 47	8.42	0438-436	4.64	04 04 35.28	-43 13 32.6	8.0	512	3.304	1415
								04 04 35.28	-43 28 32.6				
								04 03 12.72	-43 28 32.6				
								04 03 12.72	-43 13 32.6				
1.5B	C1629	2006-11-26	07 40	17 51	8.80	0438-436	4.38	04 03 54.28	-43 20 55.9	8.0	512	3.304	1415
6B	C570	1996-09-14	12 14	00 14	8.87	0438-436	4.63	04 04 35.28	-43 13 32.6	8.0	512	3.304	1415
								04 04 35.28	-43 28 32.6				
								04 03 12.72	-43 28 32.6				
								04 03 12.72	-43 13 32.6				
6C	C1629	2007-07-18	16 13	02 57	9.07	0438-436	4.43	04 03 54.28	-43 20 55.9	8.0	512	3.304	1415
6C	C1629	2007-07-19	16 51	03 50	9.65	0438-436	4.46	04 03 54.28	-43 20 55.9	8.0	512	3.304	1415
6C	C1629	2007-07-20	18 08	04 58	9.40	0438-436	4.47	04 03 54.28	-43 20 55.9	8.0	512	3.304	1415

Column 1: ATCA array configuration used. Column 2: Project Number(C1629: THINGS, other: archival data). Column 3: Start date observations. Column 4: Start time (UT). Column 5: End time (UT). Column 6: Time on-source (hours). Column 7: Phase Calibrator Name. Column 8: Calibrated flux of phase calibrator. Columns 9 & 10: RA & Dec of pointing centre (J2000). Column 11: Bandwidth (MHz). Column 12: Number of channels. Column 13: Channel width. Column 14: Central observing frequency (MHz).

University of Cape Town

Note that the archival observations consist of four different pointings to search for extended emission (McIntyre, 2008, private communication), whilst the THINGS observations consist of one central pointing. This is illustrated in Fig. 2.1: the four archival pointing centres are separated by an angular offset of 15' and therefore Nyquist sample the sky. The ATCA primary beam is 33' at 1420 MHz. The THINGS single pointing is set to the centre of the four archival pointings. In the reduction process, these five different pointings are combined in the image plane.

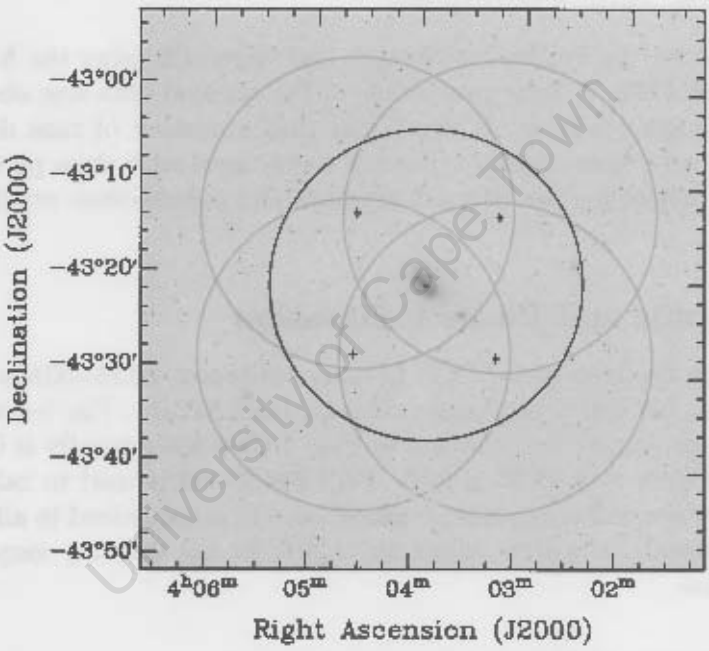

University of Cape Town

Figure 2.1: Optical image of NGC 1512. The circles mark the FWHM of the different pointings. The THINGS observations comprise of a single pointing in the centre of the map depicted by the black circle. The grey circles outline the multiple pointings in search of extended emission (archival data). Their centres are indicated with crosses and are separated by 15'. The ATCA has a primary beamwidth of ∼ 33' at an observing frequency of 1420 MHz.

The five combined pointings cover an area of ~ 0.8 deg^2. The sensitivity varies with position in the combined map due to the mosaicking of the archival data with the THINGS central single pointing. Furthermore, the sensitivity decreases towards the edges of each individual pointing. The noise RMS at the centre of the map is approximately 1.1 mJy, whilst the outer parts have typical values of 2.3 mJy.

cube that is created without continuum subtraction. The 1st order polynomial fit to the continuum emission is then subtracted from the visibility dataset. What remains is the HI line emission at each frequency interval (channel).

2.2.4 Transforming into the Image Domain

Once each observation run has been calibrated and the HI signal isolated, the visibility sets are transformed into the image domain using the INVERT task. The applied baseline weighting is known as 'super-uniform' weighting. This is a trade-off between the sensitivity of natural weighting and the minimum sidelobe level of uniform weighting. In single pointing observations this is achieved with robust weighting (Briggs, 1995). However, an implementation of robust (or uniform) weighting reduces to natural weighting when the mosaicked field-of-view is significantly larger than the primary beam. Super-uniform weighting solves this limitation by de-coupling the weighting from the size of the mosaicked field-of-view (Sault et al., 1996). The weighting scheme is implemented with a sidelobe suppression area set at an angular scale of 42'. This limits the weighting to a 42'×42' square centred on the respective pointing centre. This value is selected to be approximately equal to twice the maximum distance between two pointing centres.

Two cubes of differing resolutions were generated. The high resolution cube has a spatial pixel scale of 4"×4" and a velocity resolution of 3.5 km s^{-1}. This cube includes visibility measurements from all baselines. The low resolution cube has a spatial pixel scale of 40"×40" and a velocity resolution of 25 km s^{-1}. The low resolution cube applies a spatial filter by only including baselines < 361 metres.

Table 2.2 summarizes the mapping parameters and noise statistics of the two cubes.

1 Data Cube	2 B_{maj}	3 B_{min}	4 BPA	5 Noise	6 Size pixels	7 Pixel Scale	8 N_{chan}	9 ΔV km s^{-1}
High Res.	16.9"	16.4"	175.5°	2 mJy	512×512	4"	120	3.5
Low Res.	84.9"	72.5"	−44.6°	1.7 mJy	256×256	40"	20	25

Table 2.2: NGC 1512 mapping parameters. Column 1: Data cube, Columns 2 and 3: Major and Minor axis of synthesised beam in arcseconds, Column 4: Beam position angle of synthesised beam in degrees, Column 5: Noise per channel map in mJy, Column 6: Image size in pixels, Column 7: Pixel scale in arcseconds, Column 8: Number of channels in data cube, Column 9: Velocity width of each channel in km s^{-1}.

University of Cape Town

2.2.5 Deconvolution and Restoring

Deconvolution was performed using the MOSSDI task. This task executes the Steer, Dewdney & Ito (1984) CLEAN algorithm on a mosaicked image. Most variants of the algorithm can be decomposed into five steps. The algorithm iterates through each plane in the data cube to create a new data cube called the *clean component model*. The five steps are:

1. Search an image plane for the pixel with highest flux level, denoted P_{peak}.
2. Subtract a scaled dirty beam centered on P_{peak} from the image.
3. Add the total subtracted flux in (2) to the *clean component model* cube, retaining positional information.
4. Repeat steps 1 - 3 until a user specified condition is met (e.g. minimum RMS or maximum number of iterations).
5. Repeat step 4 for each plane in the data cube.

The high resolution cube is cleaned down to a noise level of 1.5-σ (3 mJy per 3.5 $\mathrm{km\,s^{-1}}$ channel). The residual image after deconvolution is a combination of noise and faint structure below the noise cutoff level. The resultant clean component model is convolved with the clean beam. The clean beam is a Gaussian fit to the synthesised (dirty) beam and hence has no sidelobes. This convolution is performed with the RESTOR task with a specified FWHM of 16.9"×16.4".

The low resolution cube was cleaned to a 1.8σ value of 3 mJy per 25 $\mathrm{km\,s^{-1}}$ channel. The clean model was convolved with the clean beam which has a FWHM of 84.9"×72.5".

This completes all processing done with the **Miriad** package. The remainder of the post-processing is performed with the **GIPSY** package as detailed in the next section.

2.2.6 Isolating HI Emission from Noise

To produce high fidelity maps, HI detected with a high confidence level must be separated from the noise present in each channel map. To accomplish this, each channel map is spatially smoothed by a Gaussian with major and minor FWHM twice that of the clean beam. This enhances lower column density HI, while averaging out the noise. Following this spatial smoothing, a 2.5-σ amplitude cut is

University of Cape Town

applied to the smoothed data cube. Each channel map is inspected by eye using the **GIPSY** task BLOT. Only emission above the 2.5-σ smoothed noise level and apparent in three consecutive channels (of width 3.5 km s^{-1}) is included. All pixels not meeting these criteria are blanked.

The resulting smoothed, blanked cube is used as a template to blank the original, unsmoothed cube. The output is used to generate the moment maps.

2.2.7 Generating Moment Maps

All moment maps are created with the **GIPSY** task MOMENTS. The HI total intensity map is derived from the input data cube using the equation:

$$I_{\rm HI} = \sum_{i}^{n} S_i \times \Delta v_i \qquad [\mathrm{Jy\,beam^{-1}\,km\,s^{-1}}] \tag{2.1}$$

where i corresponds to the i-th channel, n is the total number of channels, S_i is the emission in the i-th channel in units of Jy beam^{-1}, and Δv_i is the channel velocity width. The HI map can be converted to column densities using the equation:

$$N_{\rm HI} \;=\; 1.835 \times 10^{18} \left(\frac{605.7383}{b_x b_y} \right) \times \sum_{i}^{n} S_i \times \Delta v \qquad [\mathrm{cm^{-2}}] \tag{2.2}$$

where b_x and b_y are the major and minor FWHM of the dirty beam, S_i is the flux at a particular position on the map in units of Jy beam^{-1}, Δv is the velocity resolution in km s^{-1}.

HI mass is calculated using Equ. 2.3.

$$M_{\rm HI} \;=\; 2.36 \times 10^5 D^2 \times \frac{\sum_i^n S_i \times \Delta v}{1.13 \frac{b_x b_y}{p_x p_y}} \qquad [\mathrm{M_\odot}] \tag{2.3}$$

where $M_{\rm HI}$ is in units of $\mathrm{M_\odot}$, p_x, p_y are the pixel dimensions in arcsec, and D is distance measured in Mpc.

The same **GIPSY** task (MOMENTS) calculates the velocity field from the equation:

$$< v > = \frac{\sum_i^n S_i \times v}{\sum_i^n S_i} \qquad [\mathrm{km\,s^{-1}}] \tag{2.4}$$

which is the intensity weighted mean velocity.

University of Cape Town

The velocity dispersion field is generated using:

$$\sigma = \left(\frac{\sum_i^n S_i \times (v - < v >)^2}{\sum_i^n S_i} \right)^{\frac{1}{2}} \qquad [\mathrm{km\,s^{-1}}] \qquad (2.5)$$

2.3 Data Products

The resulting data products of the post-processing discussed above are presented in this section. Channel maps and position velocity slices through the galaxy are presented in Appendix A. Recall that two sets of the HI synthesis data products are generated. They differ in spatial and velocity resolutions as well as the subset of antenna baselines used for the measured visibilities.

- High resolution (spatial $\sim$ 17" ; velocity = 3.5 km s^{-1}; all baselines)
- Low resolution (spatial = 2' ; velocity = 25 km s^{-1}; baselines < 361 metres)

This is performed specifically to optimize the analysis of different physical characteristics of the maps.

The high resolution products allow a finer view of the galaxy structure and detailed kinematic analysis. The lower resolution products are primarily aimed at accentuating any low column density HI that may be associated with the galaxy. This low column density HI is put into context of the galaxy's kinematics with the low resolution velocity field.

University of Cape Town

2.3.1 High Resolution Maps

Total Intensity Map

Figure 2.2 displays the total intensity map. Most striking is the detailed HI spiral arm structure, as well as the extent of the HI disk in which NGC 1510 (α, δ = 4h 03m 32.6s, -43° 24' 00") is completely embedded. The total HI mass of the system is 5 $\times$ 10^9 M$_\odot$. This is a factor of 2 lower than the mass determined by Hawarden et al. (1979). Converting to the same cosmology (H$_0$ = 73 km s^{-1} Mpc^{-1}) yields a mass within 2% to that derived here. There is a great deal of tidal material in the outer parts of the HI disk. This may be due to the interaction with NGC 1510. The end of the southern spiral arm splits into two parts. This is also evident in velocity space with a velocity difference of $\sim$ 10 km s^{-1}.

An unexpected discovery was the HI cloud 27' to the south-west of the centre of NGC 1512. It has a mass of $\sim 6.5 \times 10^7$ $M_\odot$. This HI cloud does not appear to be an extension of the main southern spiral arm. The cloud's low mass is consistent with tidal dwarf galaxies as quoted by Schulman et al. (1994) and high velocity clouds (HVC) by Blitz et al. (1999). The cloud's diameter of ~1.5 kpc is considerably smaller than the typical value of 25 kpc quoted by Blitz et al. (1999). The cloud is a projected ~ 72 kpc from the centre of NGC 1512.

Figure 2.2: High resolution total intensity map of NGC 1512. NGC 1510 has co-ordinates 04h 03m 32.6s, -43° 24' 00" and the isolated HI cloud has co-ordinates 04h 02m 36.5s, -43° 39' 41.1". The synthesized beam is shown at the bottom left corner (super-uniform weighting, see text).

University of Cape Town

Optical comparison with HI map

Figure 2.3 shows contours of HI column density superimposed on the R band map of NGC 1512. The lowest contour corresponds to a column density of $N_{\rm HI} = 2.8 \times 10^{20}$ cm^{-2}. The remaining two contours represent column densities of $N_{\rm HI} = 0.7,\ 1$ and 1.3×10^{21} cm^{-2}. The 1×10^{20} cm^{-2} contour has a projected extent of $R \sim 60$ kpc. Fig. 2.3 clearly reveals the remarkably different morphologies of the HI and stellar content in NGC 1512. The galaxy has a HI-optical diameter ratio equal to 2.8. This is the ratio of the 1.25×10^{20} cm^{-2} HI contour to the B band 25 mag arcsec^{-2} isophotal diameter following, for consistency, the definition of Broeils & Rhee (1997). They study the relation between optical and HI diameter in 108 galaxies of varying morphology and find a HI-to-optical diameter

ratio of 1.7. This value is factor of 1.6 lower than that determined for NGC 1512.

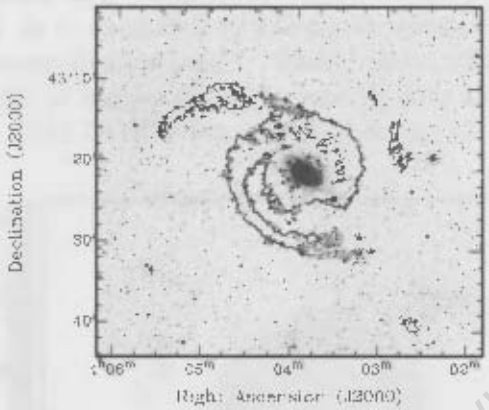

Figure 2.3: *R* band image of NGC 1512 with superimposed HI contours. The two contours correspond to column densities of 3.2 and 6×10^{20} cm^{-2}. The stellar disk can be seen in the centre of the image and NGC 1510 to the south-west of the inner disk. The *R* band image is set to high contrast for ease of comparison with the Hawarden et al. map in Fig. 2.4

The earlier Hawarden et al. (1979) map is reproduced here (Fig. 2.4) for comparison. This substantiates the point made in Sect. 1.1.1 that single dish observations are limited to measuring global properties for galaxies beyond distances of ~ 5 Mpc. The high resolution map shows a tidally disrupted HI disk, a significantly different view to that seen in the lower resolution Parkes map in Hawarden et al. (1979). Fig. 2.3 and Fig. 2.4 are roughly to scale.

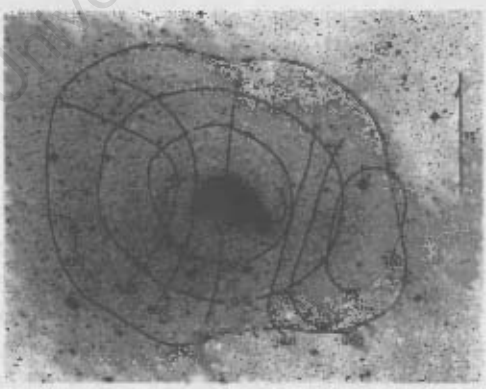

Figure 2.4: Copy of Fig. 3 in Hawarden et al. (1979) showing HI column density and iso-velocity contours of NGC 1512 superimposed on a reproduction of a highly saturated Schmidt plate. The column density contours are in units of 10^{20} cm^{-2} and the iso-velocity contours are in units of km s^{-1}. The Parkes half power beam width (15') is shown on the right of the map.

University of Cape Town

Velocity Field

Figure 2.5 displays the high resolution velocity field of NGC 1512, with superimposed iso-velocity contours. The inner disk shows a relatively regular velocity field, with 'wiggles' in the contours due to streaming motions in the spiral arms. Towards the outer parts of the disk the velocities remain consistent with the overall velocity profile of the galaxy. However, the contours become more chaotic. This is suggestive of tidal material due to a galaxy interaction disturbing the circular rotation, or the outer disk being disrupted by intergalactic material (IGM), and the decreasing signal-to-noise ratio. The isolated HI cloud to the south-west of the map has a velocity that is consistent with NGC 1512. This suggests that it is potentially associated with the galaxy and possibly isolated due to tidal disruption.

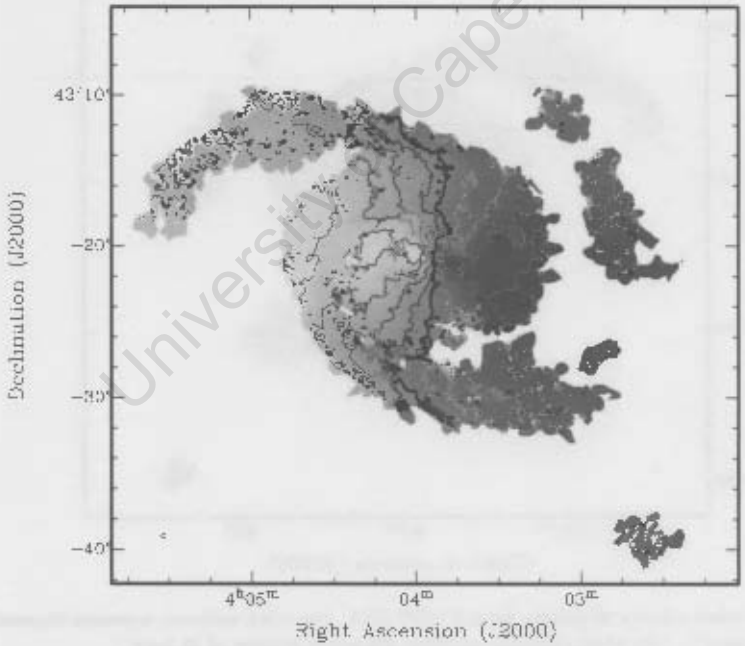

Figure 2.5: High resolution velocity field of NGC 1512. The lighter grey-scale with overlaid black contours represents approaching emission. The thick black line indicates the systemic velocity (898 km s $^{-1}$). The darker grey-scale with overlaid white contours represents receding emission. The white and black contours are spaced by an interval of 30 km s^{-1}.

University of Cape Town

Velocity Dispersion Field

The velocity dispersion field of NGC 1512 is shown in Fig. 2.6. NGC 1510's effect on the system is visible is the south-western part of NGC 1512's inner disk (see white contours). The galaxy has a mean dispersion value of ~ 11 km s^{-1}. This velocity dispersion is consistent with that found in an analysis of all the THINGS galaxies by Walter et al. (2008). This suggests that the HI disk has not been completely disrupted by a major interaction, which would cause increased non-circular motions. These non-circular motions would cause 'widened' velocity profiles and hence larger dispersion values derived from Equation 2.4.

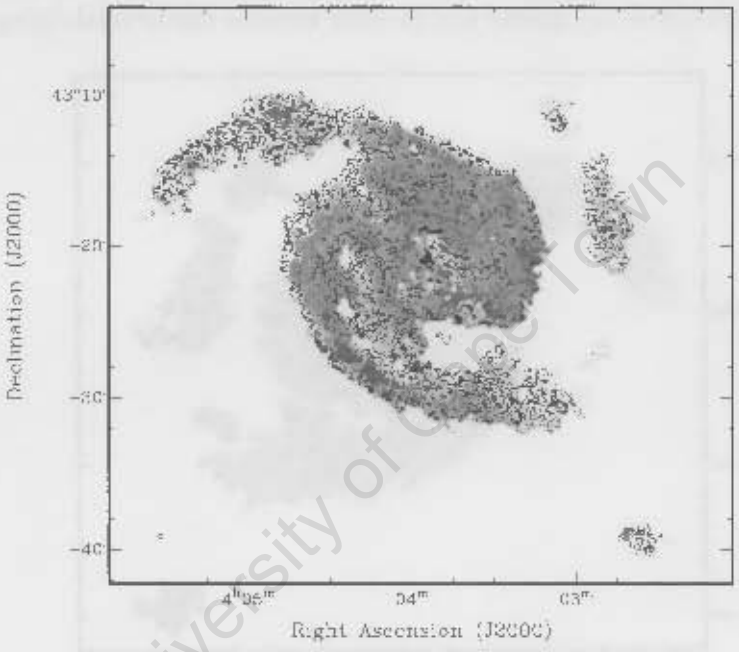

Figure 2.6: High resolution velocity dispersion field of NGC 1512. The black contours represent dispersions of 8 and 16 km s^{-1}. The white contours represent dispersion velocity of 25 km s^{-1}.

University of Cape Town

2.3.2 Low Resolution Maps

Total Intensity Map

Figure 2.7 is the equivalent of Fig. 2.2, generated however, from the low resolution data cube. Contours of total intensity are superimposed, the lowest of which corresponds to $N_{\rm HI} = 3 \times 10^{19}$ cm^{-2}. This map was generated in order to trace low column density HI emission, using baselines < 361 metres and a velocity resolution $\Delta v = 25$ km s^{-1}. An amplitude cut of 3-σ was applied to generate the moment zero map (total intensity). The lowest contour in Fig. 2.7 suggests a connection between the HI disk and the tidal material to the west. Note that there is no low column density connection between NGC 1512 and the HI cloud in the south-west of the map is present, despite the consistency of the cloud's velocity with the kinematics of NGC 1512.

The total measured HI mass of the system is $\sim 4.5 \times 10^9$ M$_\odot$. This is 10% lower than the derived mass from the high resolution map. Thus, excluding baselines > 361 metres does not reach the brightness sensitivity levels of the THINGS observations ($N_{\rm HI} \sim 1 \times 10^{19}$ cm^{-2}).

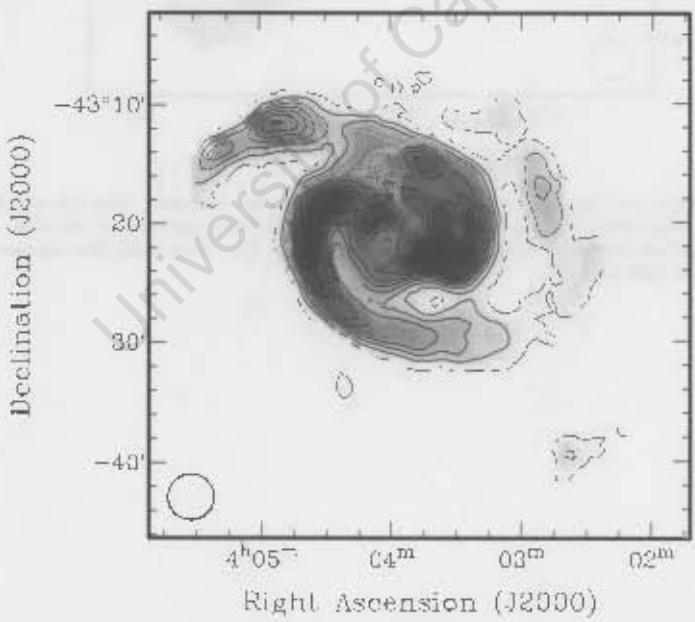

Figure 2.7: Low resolution (2′) map of NGC 1512 (grayscale) with iso-intensity contours superimposed. The contours are spaced by $\Delta N_{\rm HI} = 8 \times 10^{19}$ cm^{-2} and the lowest contour corresponds to $N_{\rm HI} = 3 \times 10^{19}$ cm^{-2} (3-σ). This lowest contour suggests a connection to the tidal material on the western side of the galaxy.

University of Cape Town

Velocity Field

The low resolution velocity field displayed in Fig. 2.8 offers additional evidence that the low column density connection between the western tidal material and NGC 1512 is real. The case for this is strengthened by the connection's consistency in velocity space. The connection is however at a low S/N level ($\sim$3-σ).

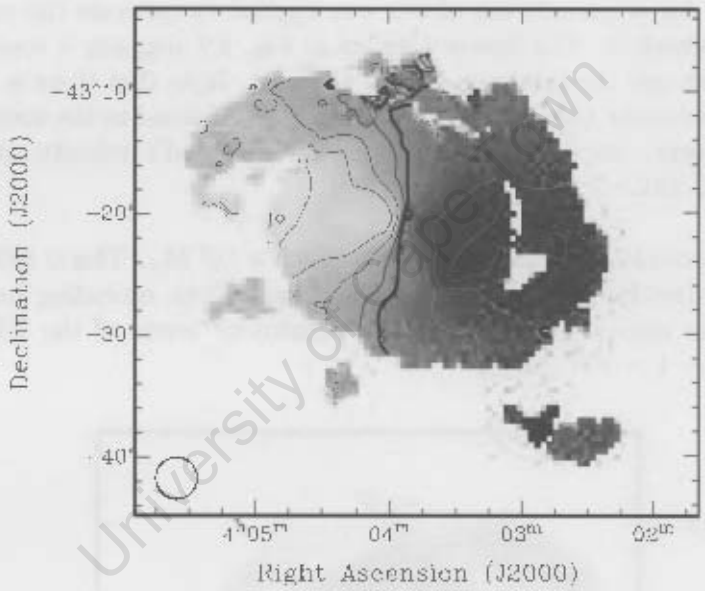

Figure 2.8: The low resolution velocity field with superimposed iso-velocity contours. The colour scheme is as in Fig. 2.5, where black contours and lighter grey-scale indicate approaching emission. White contours and darker grey-scale represent receding emission. The thick black line represents the systemic velocity (898 kms $^{-1}$).

University of Cape Town

Chapter 3

Multi-wavelength Data

Having presented the HI data, the main focus of this thesis, we now turn attention to the suite of multi-wavelength data products available for NGC 1512. One of the most important criteria of the THINGS target selection was the overlap with Spitzer SINGS and GALEX NGS samples. This is in order to combine the respective data sets and probe the science goals listed in Sect. 1.1.1.

This chapter presents all additional multi-wavelength data products used in the analysis of the NGC 1512 system (optical, single dish HI, UV, infrared). The additional HI data, from the HIPASS catalogue, is aimed at exploring the extended environment of the galaxy. The chapter closes with the description of the post-processing techniques used that allow the combination of the mid-infrared and far ultraviolet maps to form a star formation rate density map untrammeled by dust.

University of Cape Town

3.1 Optical Properties

The optical properties of NGC 1512 have been documented previously by Hawarden et al. (1979). The galaxy is classified as a SB(r)ab galaxy. It has an interacting neighbour, NGC 1510, separated by a projected 14 kpc. The Hubble type of the neighbouring NGC 1510 is somewhat uncertain. The source of the ambiguity lies in the current star formation activity. NGC 1510 is either a blue compact dwarf (BCD) or a dwarf elliptical (dE) undergoing a wave of star formation due to newly accreted material from the disk of NGC 1512 (Disney and Pottasch, 1977; Kinman, 1978; Eichendorf and Nieto, 1984). There are a number of possible morphology scenarios presented in the literature, with emphasis on the spectra of the two galaxies. Further detail on the optical study of NGC 1512 and 1510 can be found in Hawarden et al. (1979). Properties of the two galaxies are summarised in Table 3.1.

Galaxy	Right Ascension h m s	Declination ° ′ ″	Velocity km s^{-1}	Distance Mpc	m_v mag	M_V mag	Morphology
NGC 1512	04 03 54.3	-43 20 56	898	9.8±0.7	11.50	-18.45	SB(r)ab
NGC 1510	04 03 32.6	-43 24 00	913	10.0±0.7	13.02	-16.98	BCD/dE

Table 3.1: Basic parameters of NGC 1512 and NGC 1510

3.2 HI Single Dish Data

The HI Parkes All Sky Survey (HIPASS) was the first systematic HI survey of the entire southern sky. The 64 m Parkes radio telescope[1] has a beam FWHM of $\theta \sim$ 14.4 arcmin. The HIPASS observations used a velocity resolution of 18 km s^{-1}, although the channel separation was set to 13.2 km s^{-1} (at z = 0). HIPASS detected a total of 4315 sources (Meyer et al., 2004).

Despite their large extent (8°× 8°), four HIPASS cubes were needed to be merged because NGC 1512 appears in the south west corner of H114. The selected cubes (H078, H079, H113, H114) are centred on NGC 1512 and its companion to create one large data cube. Each of these cubes are from the HIPASS calibration and reduction pipeline (Barnes et al., 2001).

There are three primary reasons for including these data in this analysis:

- Compare the measured flux densities, particularly towards the edges of the ATCA pointings
- Explore the environment for further tidal material outside of the ATCA field of view.
- Put NGC 1512's location in context with its environment.

The strength in these data lies in the comparison with the high resolution data products. They are displayed in Chapter 6 in combination with the interferometric map.

[1]The Parkes telescope is part of the Australia Telescope which is funded by the Commonwealth of Australia for operation as a National Facility managed by CSIRO.

University of Cape Town

3.3 Ultraviolet

3.3.1 GALEX

This study of NGC 1512 will utilise the far and near ultraviolet (FUV and NUV) imaging data products from the GALEX Nearby Galaxy Survey (Gil de Paz et al., 2007). GALEX is a small explorer class mission orbiting at an altitude of 700 km above the Earth. Its Ritchey-Chrétien telescope has an aperture of 50 cm, affording it a field of view of $\theta \sim 1.2°$. A dichroic beam splitter allows simultaneous FUV and NUV imaging at $\lambda_{eff} = 1516$ Å and 2267 Å respectively. The FUV and NUV angular resolutions are $\Delta\theta \sim 4$" and 5.6" respectively. For more detail on the instrument see Morrissy et al. (2005).

A small degree of post processing is performed on the standard output from the GALEX reduction and calibration pipeline as documented by Gil de Paz et al. (2007). The additional processing is required to transform the data into the form required for the star formation analysis.

University of Cape Town

3.3.2 Far UV

The FUV band (1344–1786 Å) is primarily sensitive to photospheric emission from giant O and early B type stars. These short wavelengths are affected by both self-extinction and Galactic dust attenuation. The latter is corrected for with an estimation of the colour excess, $E(B-V)$, from the Schlegel, Finkbeiner & Davis (1998) extinction maps. This is converted to the corresponding FUV extinction using $A_{FUV} = 8.24 \times E(B-V)$ following Wyder et al. (2007). A background is subtracted, calculated by taking the median value of all pixels with a flux level $< 3\text{-}\sigma$. Foreground stars are subtracted using a UV color cut (NUV/FUV > 10) and the blanked regions are replaced with the mean background value.

The FUV map in Fig. 3.1 shows the strong star formation activity in the spiral arms. The extent of this is striking, extending far beyond the optical radius. Fig. 3.1 shows that the FUV emission traces a very similar pattern to the HI map. The FUV map reveals strong star formation in the ring which is prominent at optical wavelengths. However, the FUV does not reveal the stong bar seen in the optical. It is clear that the two galaxies are interacting. There is a discrete fracture in the main eastern spiral arm. The companion galaxy NGC 1510 is a strong source at this wavelength. The FUV morphology in the region of NGC 1510 is suggestive of accretion towards its centre.

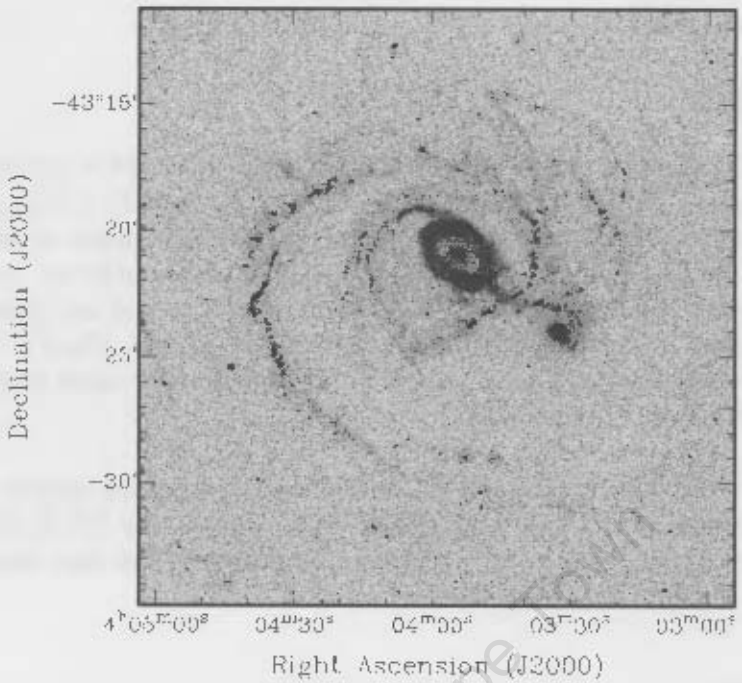

Figure 3.1: The far ultraviolet image above reveals photospheric emission from giant O and early B type stars. Note the extent of this emission compared with optical wavelengths.

3.3.3 Near UV

The NUV map is very similar in morphology to the FUV. The major difference is a stronger presence of foreground Galactic stars in the NUV map as evident in Fig. 3.2. This difference in intensity of the two maps enables foreground star subtraction using the UV colour cut discussed in Sect. 3.3.2.

3.4 Infrared

3.4.1 Spitzer

One of the selection criteria of the THINGS sample was the requirement of these galaxies to overlap with the Spitzer SINGS survey (Kennicutt et al., 2003). The current study will incorporate two data products from the Spitzer Legacy Programme. The 3.6 μm image is used in the kinematic study to model the stellar mass component. The 24 μm image is used to trace obscured star formation. The 3.6μm and 24 μm images are observed with two different instruments onboard the Spitzer spacecraft. The two data products are described below.

University of Cape Town

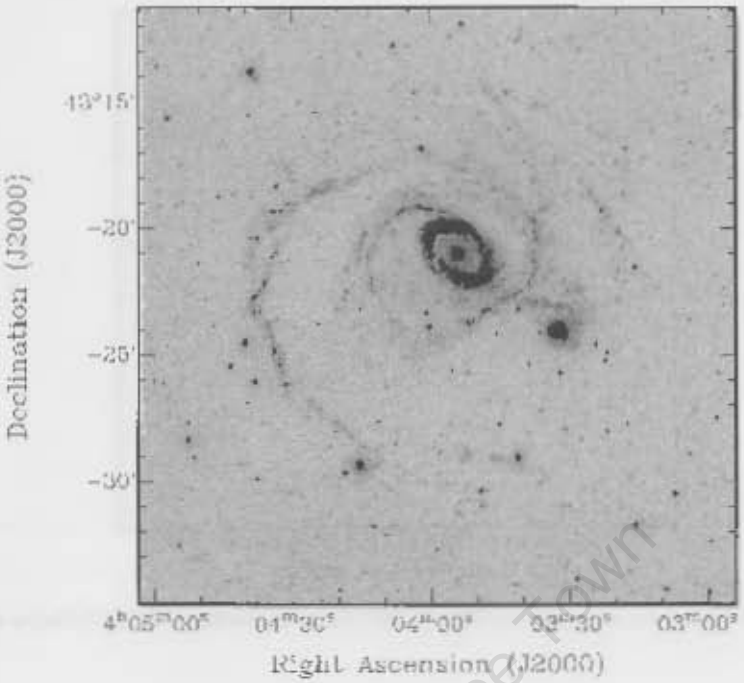

Figure 3.2: The near ultraviolet image. Note the stronger prevalence of Galactic stars

University of Cape Town

3.4.2 3.6 μm Emission

The 3.6 μm imaging was obtained with the Infrared Array Camera (IRAC) onboard Spitzer. Emission at this wavelength is sensitive to the old stellar population. It does include a contribution from polycyclic aromatic hydrocarbons (PAHs), however these are theorized to be a minor fraction of the total emission in this band (Oh et al., 2008). The IRAC instrument has a resolution of $\Delta\theta \sim 4''$ at 3.6 μm (comparable to the THINGS resolution) and a field of view of $\theta = 5.2' \times 5.2'$.

The 3.6 μm map (Fig. 3.3) reveals the bar, which is also seen in the optical. Furthermore, the 3.6 μm map displays a prominent stellar bulge as well as a faint suggestion of the ring which is more prominent in the optical bands. NGC 1510 is also prominent at this wavelength implying that a significant old stellar population is present.

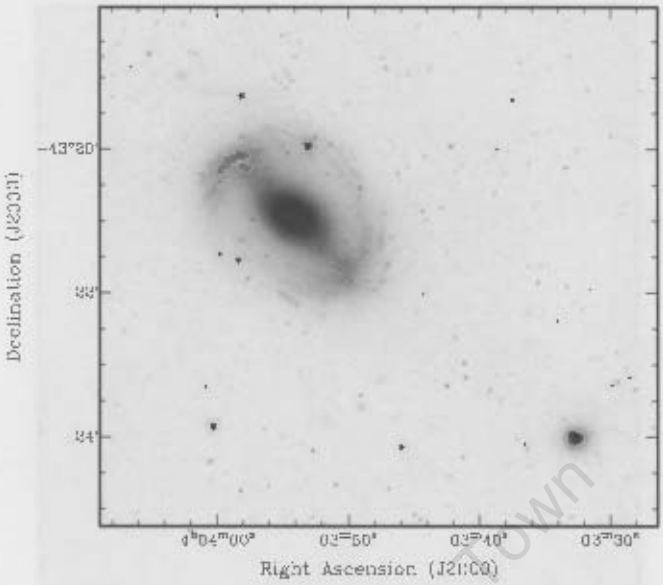

Figure 3.3: Near-infrared (3.6 μm) image of NGC 1512 and NGC 1510 from the Spitzer (SINGS) Nearby Galaxy Survey.

University of Cape Town

3.4.3 24 μm Emission

The 24 μm imaging was performed with the Multiband Imaging Photometer for Spitzer (MIPS) instrument. At 24 μm the instrument has a field of view of 5.4' $\times$ 5.4' and a spatial resolution of 6". The output from the Spitzer calibration pipeline is shown in Fig. 3.4. The reader is referred to Rieke et al. (2004) and Gordon et al. (2004) for further details on the MIPS instrument and the reduction of the 24 μm scan maps.

The map from the standard calibration pipline is used. A background is subtracted using the same procedure as for the ultraviolet maps. The same foreground stars selected from the UV colour cut are subtracted in the 24 μm map. The map is then examined by eye for any remaining bright stars, as well as the frequently evident artefacts seen towards the edges of MIPS scans (parallel with the scan direction). These artefacts are removed manually.

The 24 μm map is displayed in Fig. 3.4. It shows the ring structure in NGC 1512. However, the bar seen in the 3.6 μm map is not evident. There are two faint filaments seen in a north-easterly projection, both inside and outside the ring. The outer filament corresponds to the beginning of the main spiral arm seen in the FUV image (Fig. 3.1), suggests a gradient in the dust content along the

spiral arm, similar to that seen in Messier 81 (Willner et al., 2004). The flux is of highest concentration in the nucleus and at the location where the bar (as seen in the optical and NIR) meets the ring. The peak flux of NGC 1510 in this band is twice that of NGC 1512. Note that the ring around NGC 1510 is an imaging artefact. See the Spitzer MIPS handbook[2] for a description of the point response function (PRF). The PRF is a convolution of the point source function (PSF) and the pixel scale.

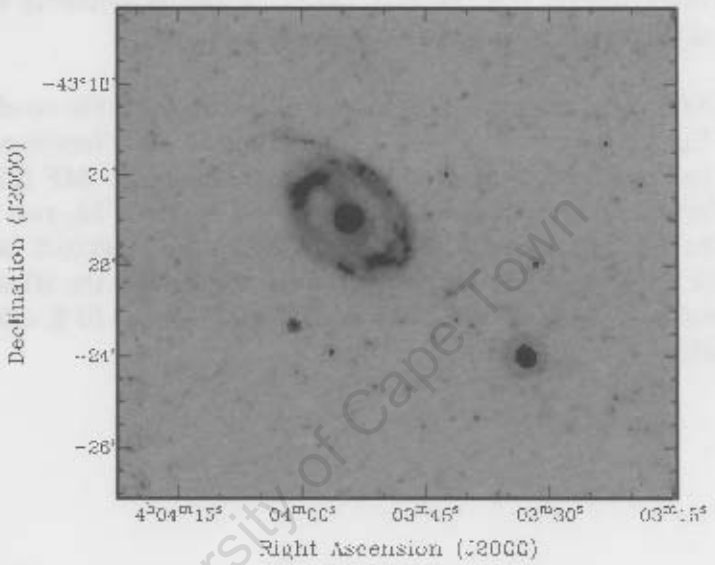

University of Cape Town

Figure 3.4: NGC 1512's ring is clearly visible in the above 24 μm image. The bar seen in the 3.6 μm image is not observed here. Two features of interest are the faint filaments in north-easterly projections, both inside and outside the ring. The outer filament corresponds to the base of the most prominent spiral arm seen in the FUV map.

3.5 Star Formation Rate Density Maps

The FUV and 24 μm maps are combined to form a star formation rate surface density (Σ_{SFR}) map with units $M_\odot\,year^{-1}\,kpc^{-2}$. The aim is to generate a star formation rate density map of comparable resolution to the HI synthesis observations presented in Chapter 2. The combination of the two wavelength regimes requires a robust calibration. Calzetti et al. (2007) and Kennicutt et al. (2007) both derive the correlation between 24 μm emission and H_α extinction due to dust. Leroy et al. (2008) use their calibration and the relation between H_α and

[2] *http://ssc.spitzer.caltech.edu/mips/dh/*

FUV emission to derive an expression for Σ_{SFR} as a function of FUV and 24 μm emission:

$$\Sigma_{SFR} = 8.1 \times 10^{-2} I_{FUV} + 3.2 \times 10^{-3} I_{24\mu m} \tag{3.1}$$

where I_{FUV} and $I_{24\mu m}$ are in units MJy sr^{-1}. The FUV-24μm combination has the advantage of tracing photospheric emission from young ($\sim$ 10 Myr), massive O and early B type stars directly (via the FUV band), as well as indirectly through the reprocessing of this starlight into mid-infrared wavelengths.

Leroy et al. (2008), and references therein, detail the choice of the co-efficients in Eq. 3.1. The Σ_{SFR} derivation assumes a Kroupa initial mass function (IMF) (Kroupa, 2001), and can be converted to the truncated Salpeter IMF (1955) by multiplying by a factor of 1.4. The RMS of the map is $\sim 1.5 \times 10^{-4}$ M$_\odot$ year^{-1} kpc^{-2}, with comparable to the maps in Leroy et al. (2008) which are generated using the same method. The maps are regridded to the same pixel scale as the HI total intensity map derived in Chapter 2. Chapter 6 compares the global SFR calculated from this map with previously determined values.

University of Cape Town

Chapter 4

Kinematics

The HI spectral line observations obtained with an interferometer enable the high resolution measurement of a galaxy's dynamics. These motions are used to derive a rotation curve of the galaxy, assuming a geometric model. Such dynamical studies allow a derivation of the associated mass via the baryonic Tully-Fisher relation (McGaugh et al., 2000); the state of the interstellar medium (Oey, 2002); and the size and distribution of the associated dark matter halo (van Albada and Sancisi, 1986).

With the HI velocity field presented in Chapter 2, this chapter will describe the derivation of the rotation curve model for the inner 55 kpc of NGC 1512, i.e. the observed rotation due to the combination of gas, stars and dark matter. The rotational velocity contribution from gas and stars is inferred from their respective mass distributions. Removing these contributions from the total observed rotation curve allows the mass distribution of the dark matter halo to be modeled.

The last section of this chapter is dedicated to the extension of the inner rotation curve model to the outermost parts. It will model the outer tidal material with respect to inclination and rotation velocity. These models of the outer disk will be put into context to the larger scale environment of NGC 1512 in Chapter 6.

University of Cape Town

4.1 Model of Observed Rotation Velocities

4.1.1 Method

Due to the projection of an observed galaxy on the sky, velocities measured in the plane of the sky are dependent on 6 parameters: the intrinsic rotation velocities, right ascension and declination of the dynamical centre, the inclination, the systemic velocity, and the position angle. The position angle (PA) is defined as the

angle between the north axis and the semi-major axis of the receding side of the galaxy, measured from north to east. The intrinsic rotation velocity is derived by solving for the remaining 5 parameters. For brevity, these 5 parameters will be referred to as the *geometric parameters.*

Internal and external effects influence the motion of matter in a galaxy (e.g. stellar feedback, galaxy interactions, infall of intergalactic material). These effects result in non-circular motions, inclination and position angle changes, etc. With this in mind, a 'best fit' dynamical model will be derived to describe the *global* kinematics in NGC 1512.

To arrive at this global model, a two dimensional velocity field must be transformed into a one dimensional plot of rotational velocity as a function of galactocentric radius. This is achieved through the division of the 2D velocity field into concentric annuli. This is known as a *tilted-ring analysis.* It allows the derivation of a characteristic rotation velocity for each annulus.

Given the high spatial and velocity resolutions of the HI observations presented in Chapter 2 and the inclination ($\sim 40°$), NGC 1512 is well suited to a tilted-ring analysis. Each ring has its own distinct set of the 6 introduced parameters (*rotation velocity*, *inclination*, *PA*, *systemic velocity*, RA_{centre}, Dec_{centre}). The dependence of the measured velocity in the plane of the sky on the geometric parameters and intrinsic rotational velocity is expressed as:

$$V(x,y) = V_{sys} + V_C(R)\sin(i)\cos(\theta) \tag{4.1}$$

assuming that all material is moving in circular orbits. In this expression, V_{sys} is the systemic velocity; V_C(R) is the rotational velocity; θ is the position angle *with respect to the receding major axis* measured in the plane of the galaxy. θ is related to the previously defined position angle (PA) in the plane of the sky by:

$$\cos(\theta) = \frac{-(x-x_0)\sin(PA) + (y-y_0)\cos(PA)}{R} \tag{4.2}$$

$$\sin(\theta) = \frac{-(x-x_0)\cos(PA) - (y-y_0)\sin(PA)}{R\cos(i)} \tag{4.3}$$

where x_0, y_0 are the central pixel co-ordinates of the tilted-ring model. x, y are also in pixel co-ordinates.

Interpretation of the above three equations is sensitive to non-circular motions, tri-axiality and dynamical centre positional uncertainties. See Oh et al. (2008),

Trachternach et al. (2008) and de Blok et al. (2008) for in-depth studies on methods to correct for these uncertainties.

The **GIPSY** task ROTCUR is used to perform the tilted-ring analysis and derive the rotation curve. The parameters are varied for each ring to obtain an optimal fit in a least-squares algorithm[1]. The width of each ring is equal to a synthesised beam. Therefore all rotation curve data points are independent from one another.

The first step in modeling the rotation curve of NGC 1512 allows the geometric parameters and rotation velocity to run as free variables through the least-squares algorithm. The result of this first iteration is plotted in Fig. 4.1. Note that in Fig. 4.1 the uncertainties for the geometric parameters represent the formal least squares error, whereas the uncertainty illustrated with the rotation velocity (V_{rot}) plot is the dispersion in individual velocity measurements along each respective tilted-ring. The latter is found to be a more conservative error estimate (see 19 galaxy rotation curves derived in de Blok et al. 2008).

University of Cape Town

[1]Documented at *http://www.astro.rug.nl/~gipsy/tsk/rotcur.dc1*

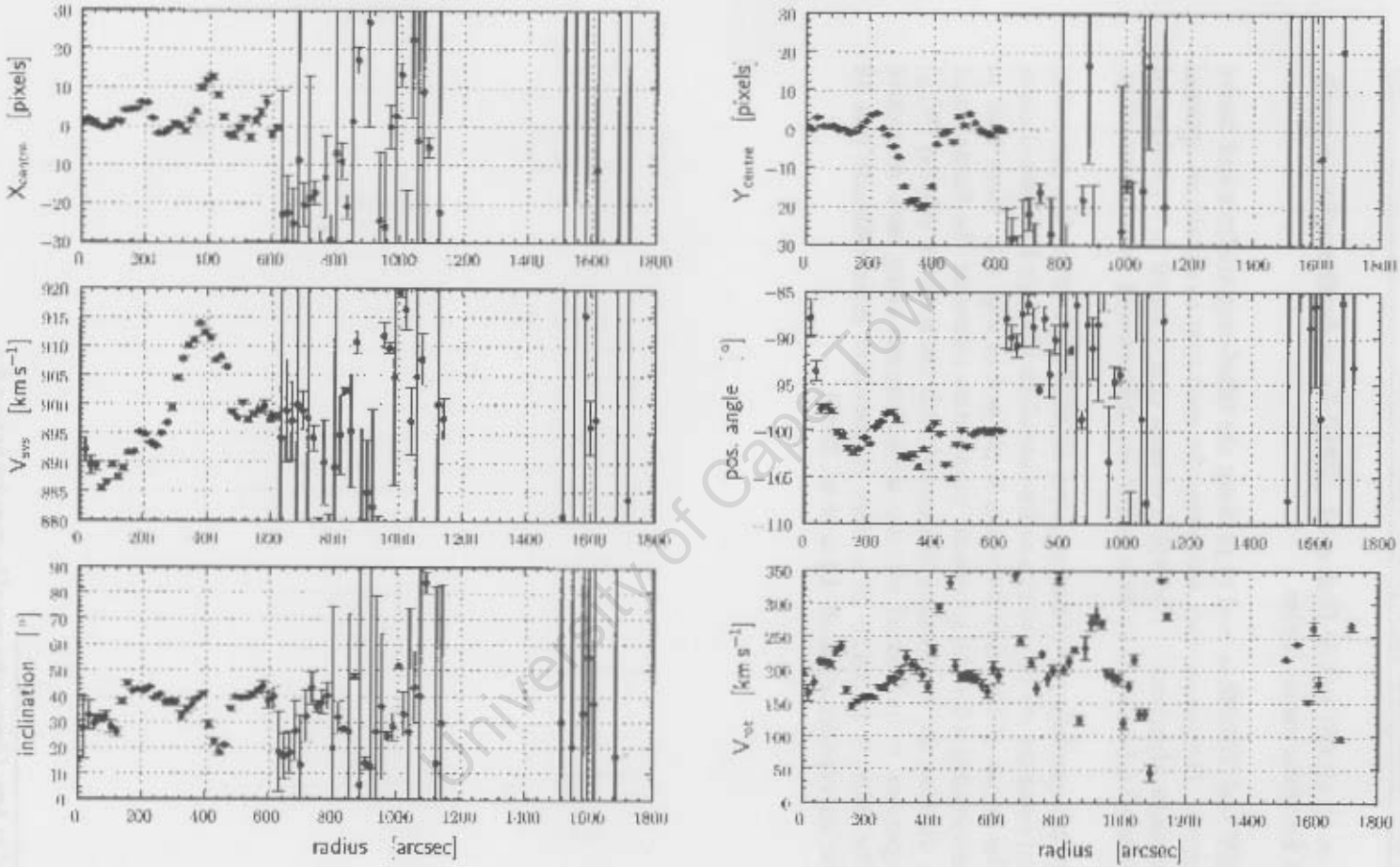

Figure 4.1: Plots of least square fits to the geometric parameters and resulting rotation velocity (bottom right). X_{centre} and Y_{centre} (top left and top right) are the pixel co-ordinates of the dynamical centre (pixel scale = 4"). V_{sys} (middle left) is the systemic velocity; *pos. angle* (middle right) is the position angle; and *inclination* (bottom left). The uncertainties for the geometric parameters are the formal least squares errors, the uncertainty for V_{rot} is the total dispersion along each tilted-ring. Note the jump to higher uncertainties in the geometric parameters beyond $R \sim 600$".

University of Cape Town

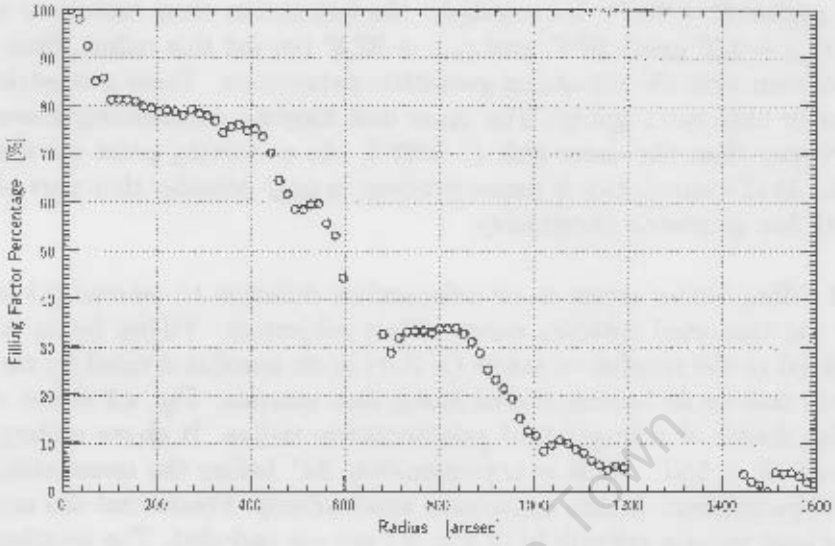

Figure 4.2: Filling factor for each concentric ring, defined as the number of measured data points ($> 3\text{-}\sigma$) divided by the number potential data points in a ring. A steep decrease is seen around 600" and a 60% filling factor criterion is applied to determine a high fidelity rotation curve.

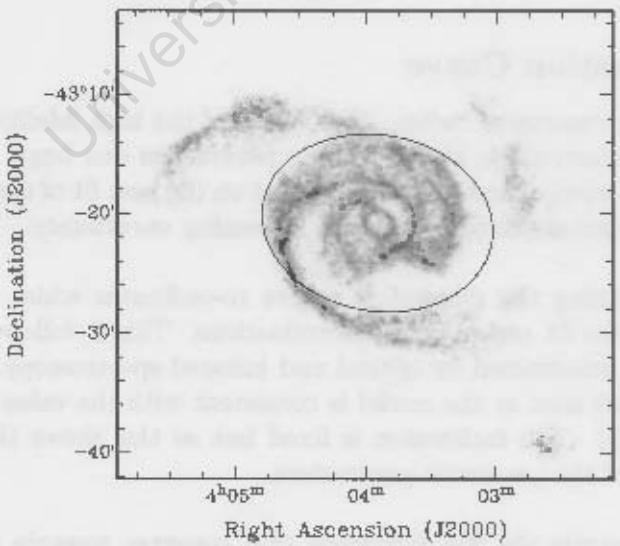

Figure 4.3: Total intensity map of NGC 1512 with superimposed ellipse positioned at a radius of 578" (27.5 kpc). The truncated rotation curve is derived from all points within this ellipse.

University of Cape Town

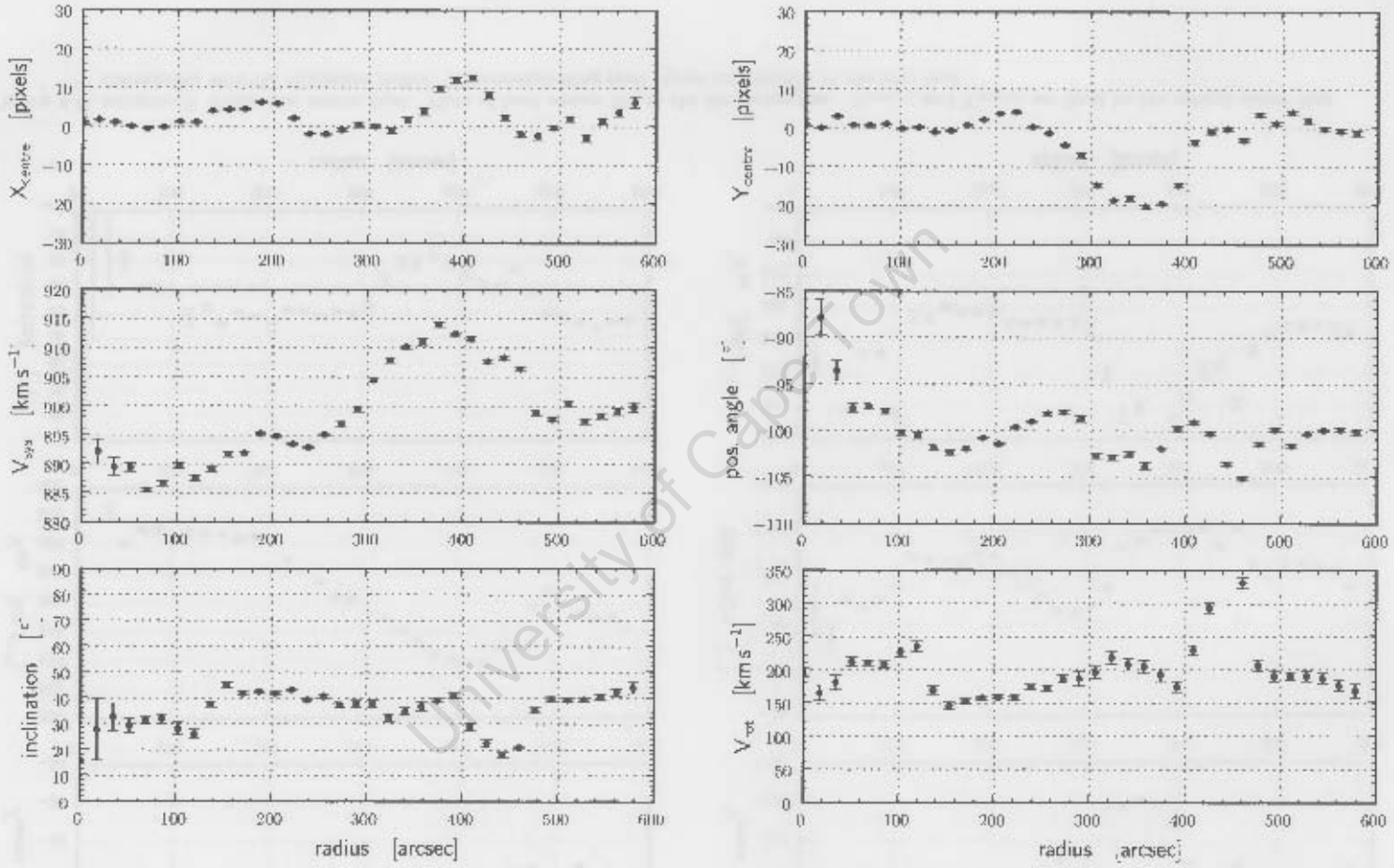

University of Cape Town

Figure 4.4: Iteration 1: No parameters fixed. Least squares fits to the six parameters that determine the observed velocity of HI emission in NGC 1512. Only the inner 578" are considered, as these radii have a filling factor greater than 50%. Plots are laid out as in Fig. 4.3 with uncertainties as defined in Sect. 4.1.1.

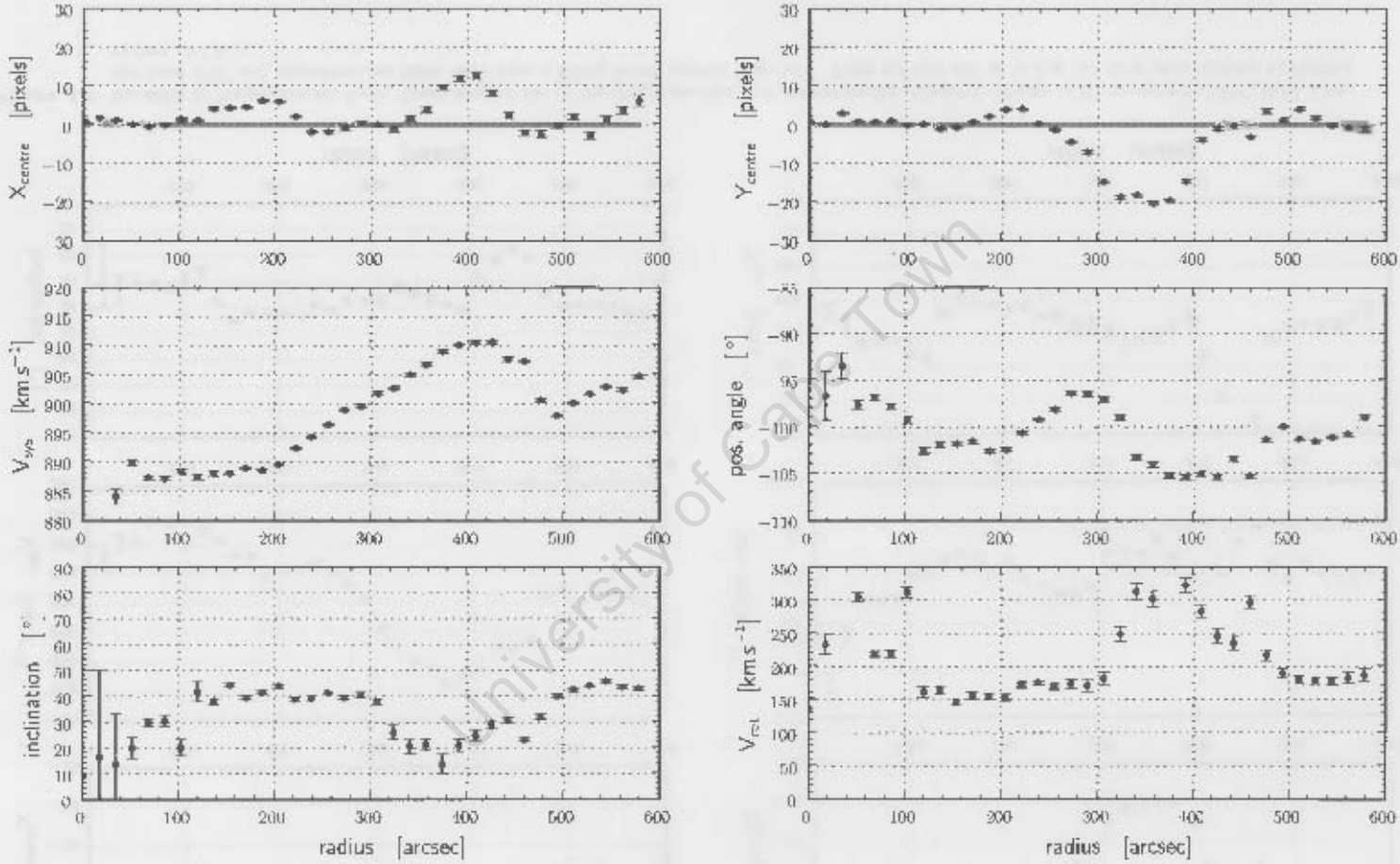

Figure 4.5: Iteration 2: Dynamical centre fixed. Plots of least square fits to the six parameters. X_{centre} and Y_{centre} are fixed to the optical centre that corresponds with the dynamical centre. The corresponding pixel values are depicted by the grey lines

University of Cape Town

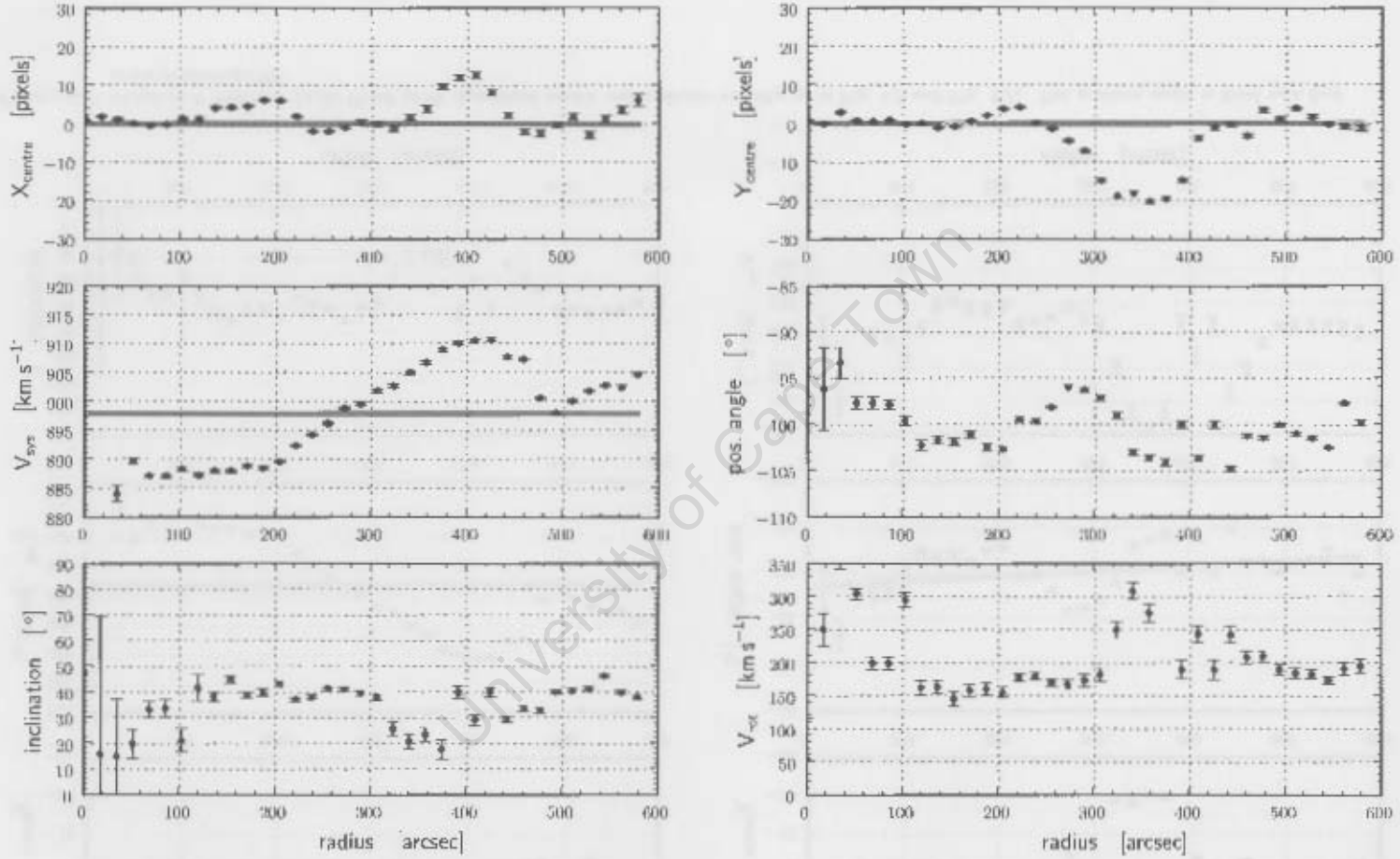

Figure 4.6: Iteration 3: Systemic Velocity Fixed. With same X_{centre} and Y_{centre} from Iteration 2. This iteration additional fixes the systemic velocity, V_{sys}, to 898 km s^{-1}, the best fit value (excluding the inner 51"). It is consistent with previously determined recession velocities for NGC 1512.

University of Cape Town

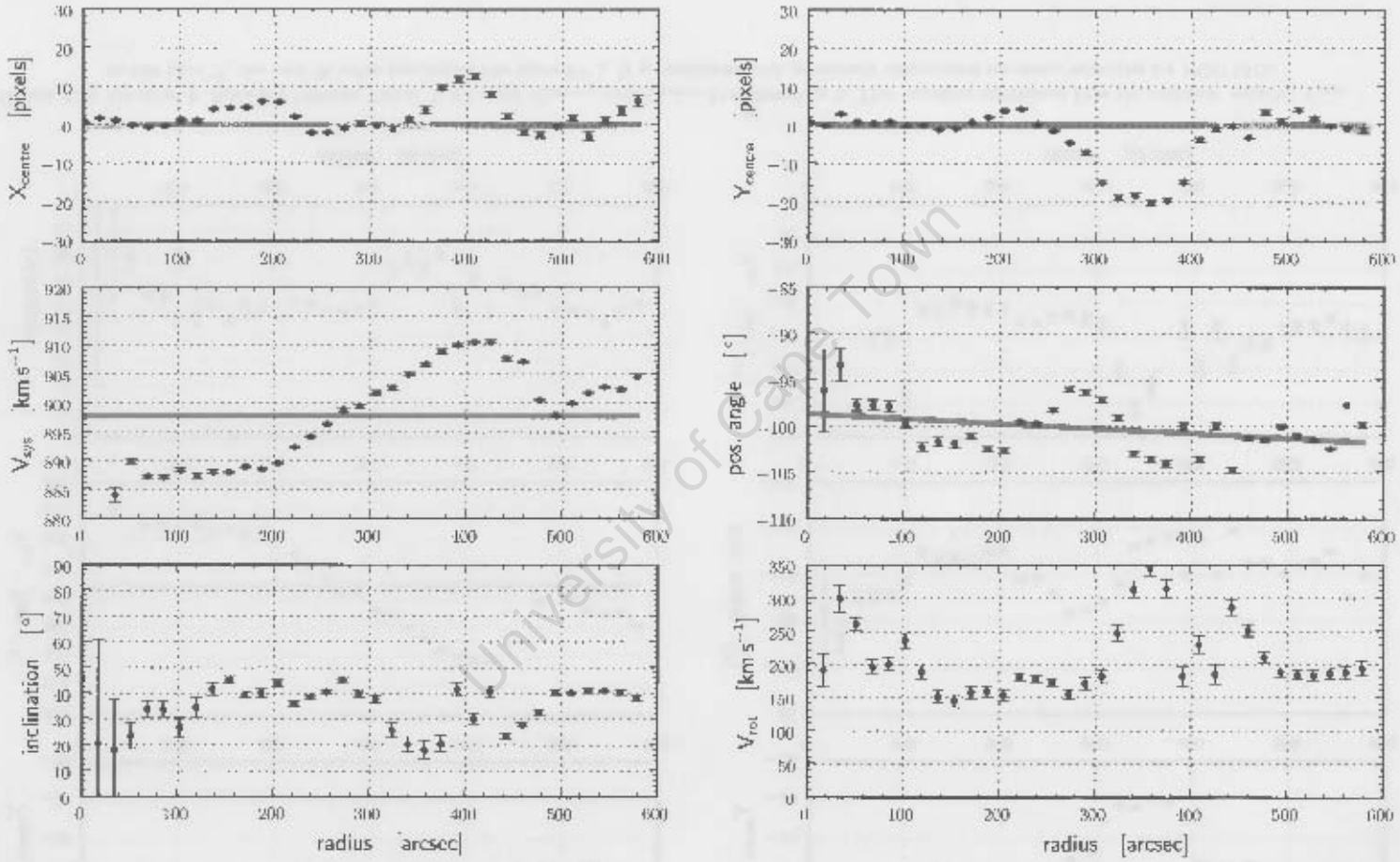

Figure 4.7: Iteration 4: Position Angle Fixed (with dynamical centre and systemic velocity as in Fig. 4.5 and Fig. 4.6). The position angle is fixed to a first order polynomial fit.

University of Cape Town

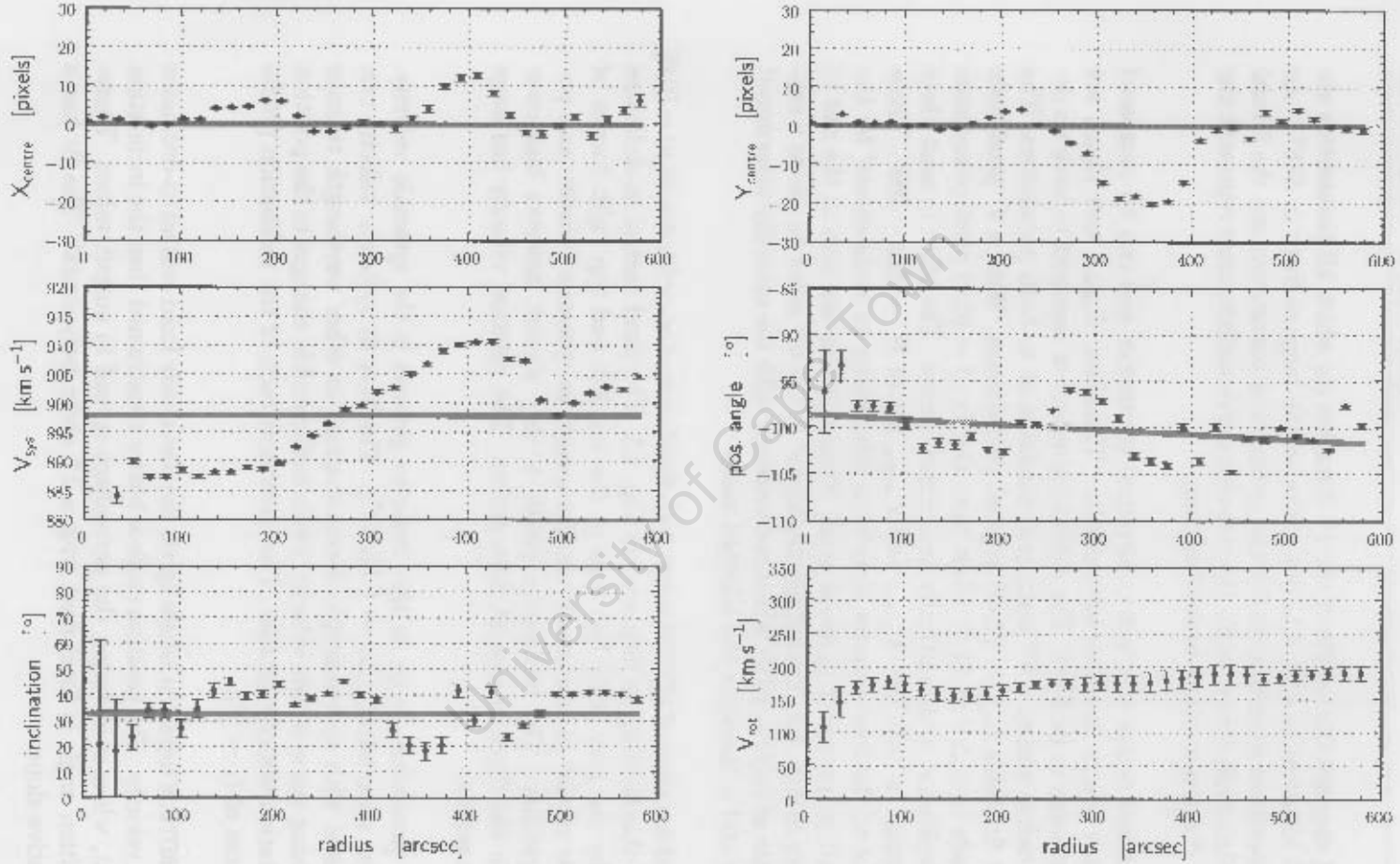

University of Cape Town

Figure 4.8: Iteration 5: Inclination Fixed. Inclination is fit to a first order polynomial which yields a virtually flat gradient. This concludes the iterative fitting procedure of the geometric parameters and yields a best fit rotation curve model (bottom right).

Figure 4.4 displays the results of the 1^{st} iteration (in which all parameters are free). This is identical to Fig. 4.1, but excludes the large radii ($r > 578$"). As before, the associated uncertainties for the geometrical parameters are the formal least-square algorithm errors, while the rotation curve uncertainties represent the total velocity dispersion along each tilted-ring.

The dynamical centre is a well constrained parameter and can be compared with the galaxy centre at other wavelengths. Therefore, X_{centre} and Y_{centre} are the first parameters to be fixed. The dynamical centre is assumed to have no dependence on radius and so a 0^{th} order polynomial is fit to both parameters. The resulting best fit yields (x,y) = (2,-3) in pixel co-ordinates. With a 4" pixel-scale this corresponds to a $\Delta R = 14.4$" offset from the (x,y) = (0,0) pixel co-ordinate which, by coincidence, is the optically determined centre. The offset is most likely due to the 'kinks' in both the X_{centre} and Y_{centre} fits at $R \sim 300 - 400$". These 'kinks' are due to the least squares algorithm attempting to 'compensate' for the streaming motions prevalent in spiral arms. Similar 'kinks' are seen in the rest of the parameters in Fig. 4.4. Excluding the 'kinks' in the 0^{th} order fit yields a central co-ordinate of (x,y) = (0,0) which is consistent with the optically determined galaxy centre and is therefore the adopted value.

The second iteration of ROTCUR is run with fixed central co-ordinates (x,y) = (0,0). The result of this iteration is displayed in Fig. 4.5. The fixed central co-ordinates are marked by the grey solid line seen in the top left and top right frames of Fig. 4.5. This results in marginally smaller ranges in systemic velocity and position angle profiles. The inclination profile is very similar, however has lower uncertainty in the three innermost data points. The rotation velocity has large 'kinks' in the profile.

The next parameter to fix in this iterative process is the systemic velocity. This has a low uncertainty ($\Delta v \sim 1$ km s^{-1}). The best fit systemic velocity can be cross-checked with spectroscopic determinations in other wavelength regimes (e.g. H_α). Fixing the systemic velocity yields indiscernible changes in the position angle and rotation velocity profiles. The outermost radii of the inclination profile show differences of ($i \sim 4°$).

The next ROTCUR iteration builds up on the previously fixed central co-ordinates and systemic velocity. The position angle is better constrained than the inclination in this output, when considering the percentage spread in output values. Therefore, the position angle is fixed next with a 1^{st} order polynomial. The fit has a shallow, negative slope.

University of Oxford

ROTCUR is run once more with central co-ordinates, systemic velocity and position angle fixed. This results in a larger amplitude ($v \sim 350$ km s^{-1}) 'kink' in the rotation velocity seen at $R \sim 350" - 450"$. The innermost 'kink' at $R \sim 40"$ decreases by approximately $\Delta v = 50$ km s^{-1}. The changes in inclination are indiscernible. As in the previous iterations, the inclination shows characteristic 'wiggles'. These most likely correspond to streaming motions within the galaxy's spiral arms. The least squares algorithm in ROTCUR computes a better overall fit by varying both the inclination and rotation velocity to model these streaming motions, despite it being a less physical model (de Blok et al., 2008). The first order fit of the inclination values is made, excluding $R < 51"$ and the 'kink' between $R = 323" - 391"$. This yields an inclination fit of $i = 38.5°$.

A final iteration is run with the ROTCUR task to derive a rotation curve based on the iteratively fit and physically motivated galaxy parameters.

University of Cape Town

4.1.3 Results

The procedure outlined in the previous section results in the rotation curve for the inner 27.5 kpc (R =578" assuming D = 9.8 Mpc) of NGC 1512 displayed in Fig. 4.9. The uncertainties in this plot represent the dispersion of individual velocity data points along each tilted-ring. The rotation curve has typically uncertainties of 11 km s^{-1}. This value is consistent with the typical dispersion velocity derived by de Blok et al. (2008) for the 19 galaxies studies at similar resolution in The HI Nearby Galaxy Survey (THINGS). The resulting rotation curve is relatively smooth and regular given that this is an interacting, asymmetric galaxy.

4.2 Derived Mass Model

The observed galaxy rotation is due to the combined mass of gas, stars and dark matter. The primary aim of a rotation curve analysis is to disentangle these and quantify each component as a function of radius, with emphasis on the dark matter distribution. This requires three main inputs: the observed rotation curve derived in the previous section, the gas mass density profile and the stellar mass density profile. The latter two can be derived from the HI total intensity and Spitzer near-infrared (3.6 μm) maps respectively. This section describes the procedure in combining these inputs to derive a galaxy mass model.

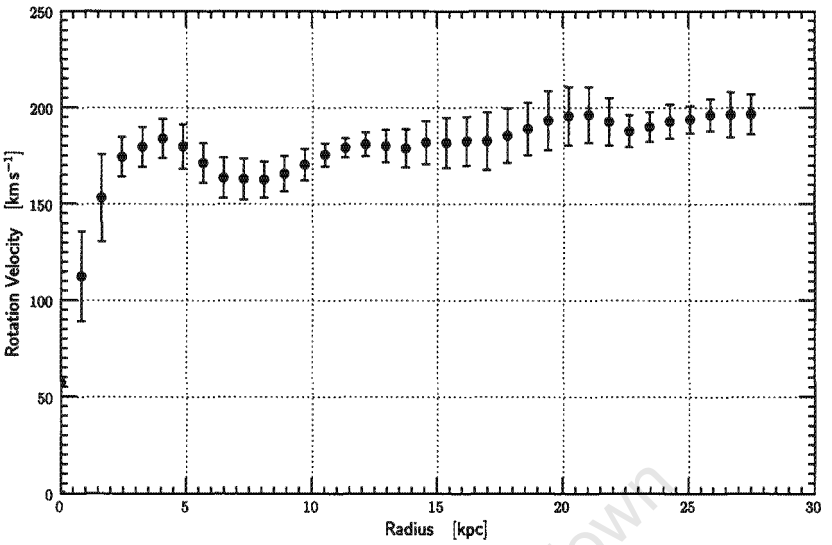

Figure 4.9: Derived rotation curve of the inner 27.5 kpc of NGC 1512 based on central co-ordinates, systemic velocity, position angle and inclination constrained by a least-squares algorithm. The plot shows undulations in velocity attributable to the streaming motions in the spiral arms of the galaxy. The associated uncertainty is derived from the dispersion of the velocity measurements along each annulus.

University of Cape Town

4.2.1 Method

Gas Distribution

The same tilted-ring parameters applied to the HI velocity field are now applied to the HI total intensity map using the ELLINT task. This task bins a input map into elliptical rings, the orientation of which is derived from the tilted-ring analysis described in the previous section. The average HI flux within each concentric ring is corrected for inclination and converted into its corresponding surface density. The result is scaled by a factor of 1.36 to account for helium and metals. The conversion from HI flux to mass is given by Equations 2.2 and 2.3.

The radial HI surface density distribution is used to calculate corresponding rotational velocities using the task ROTMOD, assuming an infinitely thin disk. ROTMOD is a task that converts the radial HI flux profile into rotation velocities resulting from the enclosed mass (Casertano, 1983). The output values represent the rotational velocity of each ring assuming the gas to be the only mass component.

Stellar Distribution

The conversion of stellar emission to a corresponding stellar mass has a considerably larger associated uncertainty than that of the neutral gas. The stellar mass-to-light ratio, $(M/L)_\star$, is a function of parameters including wavelength, stellar population age, star formation history, dust extinction, metal content and the stellar initial mass function. These uncertainties decline with increasing wavelength towards the near-IR. This wavelength regime is predominantly sensitive to the old stellar population and therefore is a good tracer of the total stellar mass contribution (Bell and de Jong, 2001). Both Bell & de Jong (2001) and Verheijen (1997) find a small range in the K band mass-to-light ratios ($(M/L)_\star = 0.5\pm0.2$, 0.7 ± 0.2 respectively). Observations in the near-IR are not strongly affected by the young stellar population, dust and metallicity. The near-IR is therefore the optimal wavelength range of choice to constrain the total stellar mass component.

The near-IR imaging data is available from 3.6 μm Spitzer SINGS Legacy Programme (see Sect. 3.4.2). The foreground Galactic stars were manually removed, as well as the emission of NGC 1510. The same tilted-ring elliptical integration applied to the HI intensity map is repeated on the star subtracted 3.6 μm map, resulting in a mean radial distribution of 3.6 μm flux in units of MJy steradian^{-1}. Following the method adopted in Oh et al. (2008), the $(M/L)_\star$ is calculated to convert the 3.6 μm flux profile into a mass distribution profile. Oh et al. (2008) derive an empirical relation between the K band and 3.6 μm $(M/L)_\star$ values. The K band $(M/L)_\star$ is calculated from Eq. 4.4 using $(J - K)$ colours from the 2MASS Large Galaxy Atlas (Jarrett et al., 2003).

$$\log (M/L)^\star{}_K = 1.43(J - K) - 1.38 \tag{4.4}$$

The empirical relation,

$$(M/L)^\star{}_{3.6\mu m} = 0.92(M/L)^\star{}_K - 0.05 \tag{4.5}$$

is adopted from Oh et al. (2008). The radial stellar mass distribution serves as an input into the `ROTMOD` task. The stellar distribution is split into two exponential components, loosely labeled the 'disk' and the 'bulge'. This is required as the stellar radial profile reveals a distinct steep inner component ($R < 700$ pc) and a flatter outer disk ($R > 700$ pc) typical of LSBs. Therefore, a two-component model of the stellar radial profile enables a more accurate determination of the total stellar flux.

University of Cape Town

A $sech^2$ vertical distribution is assumed for these two stellar components. The vertical scale length is set to $z_0 = h/5$ where h is the exponential radial scale length (van der Kruit and Searle, 1981a; van der Kruit and Searle, 1981b). These inputs enable the ROTMOD task to compute the rotation velocity attributable to the stellar components if they existed in isolation.

Dark Matter Halo Distribution

As described previously, the total observed rotation in a galaxy is primarily due to three components:

$$V_{obs}^2 = V_{gas}^2 + V_{stellar}^2 + V_{dark}^2 \tag{4.6}$$

where V_{obs} is the total rotation curve modeled from the HI velocity field; V_{gas} and $V_{stellar}$ are the rotation curves of the gas and stellar components, as derived from the respective intensity maps. The last term in Equation 4.6, V_{dark}, is the rotational velocity contribution due to the mass of the dark matter halo. It can be derived from Equation 4.6 given the measured observables V_{obs}, V_{gas} and $V_{stellar}$. Its distribution is fit to a given halo distribution model. This study assumes a pseudo-isothermal dark matter halo of the form:

$$\rho_{ISO} = \rho_0 \left(1 + \left(\frac{R}{R_C}\right)^2\right)^{-1} \tag{4.7}$$

In this equation, ρ_0 is the central surface density and R_C, the core radius. The rotation velocity of this dark matter halo as a function of radius is expressed as:

$$\mathrm{V}(R) = \left(4\pi G \rho_0 {R_C}^2 \left[1 - \frac{R_C}{R} \arctan\left(\frac{R}{R_C}\right)\right]\right)^{\frac{1}{2}} \tag{4.8}$$

Two fits are made within the GIPSY task ROTMAS: the first uses the derived $(M/L)_\star$ value described in Sect. 4.2.1; the second fit sets $(M/L)_\star$ to the maximum possible value allowed by the observed rotation curve. The latter is often referred to as the maximum disk fit and is a lower limit on the dark matter content of the galaxy. ROTMAS is the task that fits the 'residual' rotation velocity, V_{dark} from Equation 4.6 to the user defined dark matter halo distribution function, which in this study is the pseudo-isothermal halo (Eq. 4.8).

University of Groningen

4.2.2 Results

Mass Model Based on the Derived Stellar Mass-to-Light Ratio

This model adopts a mass-to-light ratio derived from the $J - K$ colour described in Oh et al. (2008). The resulting value of $(M/L)_{\star} = 0.59$ is consistent with the mass-to-light ratios determined for the 19 galaxies in the Northern THINGS sample, as illustrated in Fig. 4.10.

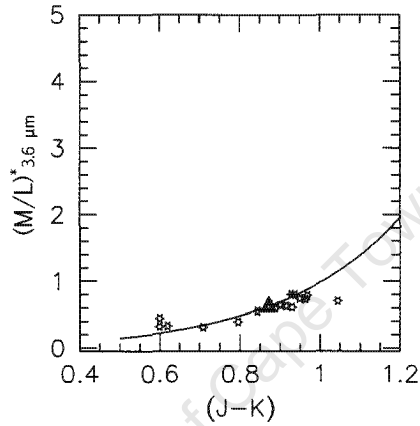

Figure 4.10: The stars in this plot represent derived $(M/L)^{*}_{3.6\ \mu m}$ values as a function of $J - K$ colour from de Blok et al. (2008). The triangle corresponds to the value derived for NGC 1512 in this analysis. The solid line is the predicated values which assumes constant colour throughout individual gaalaxies. The scatter is due the observed colour gradient in the sample.

The output of the ROTMAS task is a fit to a pseudo isothermal dark matter halo. This is plotted in Fig. 4.11 as a thick, black solid line. It is based on the value derived in Sect. 4.2.1 of $(M/L)^{\star}_{3.6\ \mu m} = 0.59$. The observed, gas and stellar rotation curves are also plotted.

The mass model based on this $(M/L)^{\star}_{3.6\ \mu m}$ value finds NGC 1512 to be dark matter dominated at 27.5 kpc ($M_{DM}/M_{baryons} = 2.1$). De Blok and McGaugh (1997b) find 15 of their sample of 23 LSBs to have a larger $M_{DM}/M_{baryons}$ value. This suggests that while NGC 1512's dark matter content is consistent with LSB galaxies, its $M_{DM}/M_{baryons}$ value is less than the average found by de Blok and McGaugh (1997) of $M_{DM}/M_{baryons} = 2.6$. The relative fraction of dark matter to gas and stars will increase if the limiting radius is extended beyond 27.5 kpc. The HI rotation curve shows a number of negative values in the inner 9 kpc. This results from the conversion of HI mass distribution to velocities in the ROTMOD task. A negative sign is denoted to velocity values if the associated acceleration is a net force away from the centre of the galaxy.

University of Cape Town

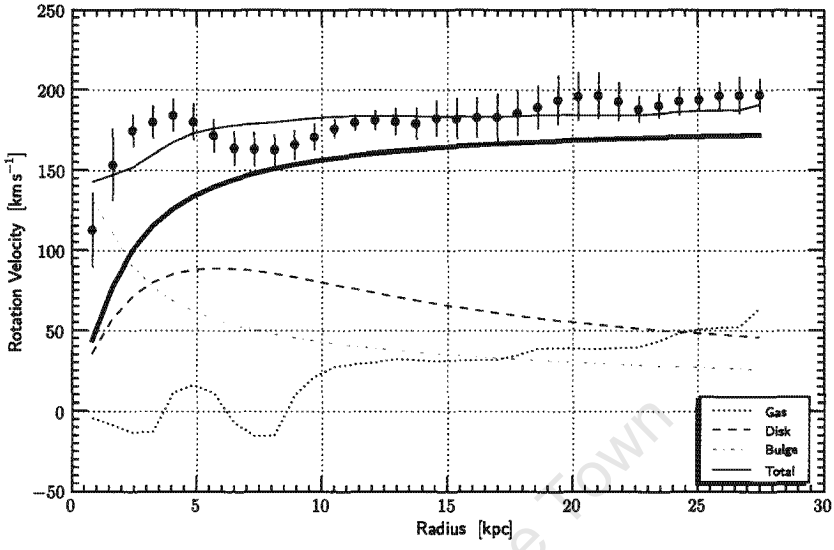

Figure 4.11: Mass model of NGC 1512. Circles represent the total mass derived from the HI observations; the thick solid line the dark matter with an pseudo iso-thermal sphere distribution; the dotted line the gas, the dashed and dot-dashed lines the stellar disk and bulge components respectively, and the thin solid line represents the total mass derived as a quadratic sum of these modeled components.

University of Cape Town

The mass model is summarised quantitatively by the dynamical mass calculation, the baryon-dark matter ratio, and mass-to-light ratio (M/L_B). The maximum rotation velocity (196.7 km s^{-1}) is found at the largest radius considered, $R = 27.5$ kpc. Equating centripetal and gravitational forces for the mass within a given radius implies a dynamical mass $M_{dyn} = 2.5 \times 10^{11}$ M$_\odot$.

$$\frac{GMm}{r^2} = \frac{mV^2}{r} \tag{4.9}$$

$$M_{dyn} = \frac{V^2 R}{\mathrm{G}} \tag{4.10}$$

where V is the rotational velocity of the outermost data point in units of km s^{-1}; R is the radius at which V is measured in kpc; and G is the gravitational constant in units of kpc^3 kg^{-2} s^{-2}.

Roberts & Haynes (1994) studied galaxy properties as a function of morphological type. Their sample included $\sim$ 5000 galaxies which part of the Local

Supercluster ($v < 3000$ km s^{-1}). They found the mass of Sab galaxies to range between $0.4 - 2 \times 10^{11}$ M$_\odot$ (25 and 75 percentiles respectively). The derived dynamical mass $M = 2.5 \times 10^{11}$ M$_\odot$ of NGC 1512 makes it a high mass galaxy for its morphological type, particularly as only mass within $R = 27.5$ kpc is considered. This implies a total mass-to-light ratio of, $(M/L)_B = 86$, based on the apparent magnitude, $m_B = 11.5$ (as adopted by Hawarden et al. 1979).

The ratio of baryons and dark matter in NGC 1512 is calculated using the outermost rotation velocity of the observed rotation curve.

$$\frac{M_{baryons}}{M_{DM}} = \left(\frac{V_{HI}^2 + V_{stellar}^2}{V_{obs}^2 - V_{HI}^2 - V_{stellar}^2} \right)^{\frac{1}{2}} \tag{4.11}$$

where V_{obs}, V_{HI} and $V_{stellar}$ are the outermost velocities for the relevant mass components. The determined value of $\frac{M_{baryons}}{M_{DM}}$ is 0.47, assuming the derived $(M/L)^{\star}_{3.6\ \mu m}$ value in Sect. 4.2.1. Comparison with de Blok and McGaugh (1997) finds this $\frac{M_{baryons}}{M_{DM}}$ value to be larger than 17 of their sample of 23 LSBs. The average baryon-to-DM ratio in their sample is $\frac{M_{baryons}}{M_{DM}} = 0.39$.

Maximum Disk Mass Model

The maximum disk fit is plotted in Fig. 4.13. The maximum disk model scales the outer stellar disk component to the maximum value allowed by the observed rotation curve. The inner stellar component (bulge) is not scaled as it is already constrained to its maximum value by the observed rotation curve. Scaling the outer stellar component requires scaling the derived $(M/L)^{\star}_{3.6\ \mu m}$ value by a factor of 3.77. While this scenario is inconsistent with stellar population synthesis models, it is a useful method of deriving a lower limit to the dark matter halo mass. Fig. 4.12 is the repeated plot from de Blok et al. (2008) showing all the derived $(M/L)^{\star}_{3.6\ \mu m}$ values for a selection of the THINGS galaxies with star-shaped symbols as before. Two points are overlaid on this plot: (1) the derived $(M/L)^{\star}_{3.6\ \mu m}$ value for NGC 1512 used in Fig. 4.11; and (2) the value required by the maximum disk model plotted in Fig. 4.13. It is clear that the maximum disk assumption requires a substantial deviation of $(M/L)^{\star}_{3.6\ \mu m}$ from what is observed for galaxies of similar $J - K$ colour.

The maximum disk fit, shown in Fig. 4.13, reveals NGC 1512 to be dark matter dominated at a radius $R \sim 27.5$ kpc. At this radius, the mass of the dark matter halo is approximately 4 times greater than the baryonic material (Mass $\propto$ V^2).

University of Cape Town

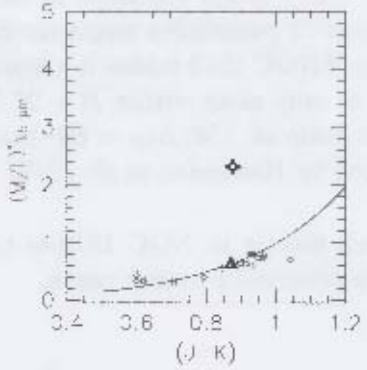

Figure 4.12: The stars in this plot represent derived $(M/L)^{*}_{3.6\ \mu m}$ values as function of $J - K$ colour from de Blok et al. (2008). The solid line line represents the theoretical prediction. The triangle corresponds the value derived for NGC 1512 with the same method, while the large, four-sided star represents the value required if a maximum stellar disk is assumed.

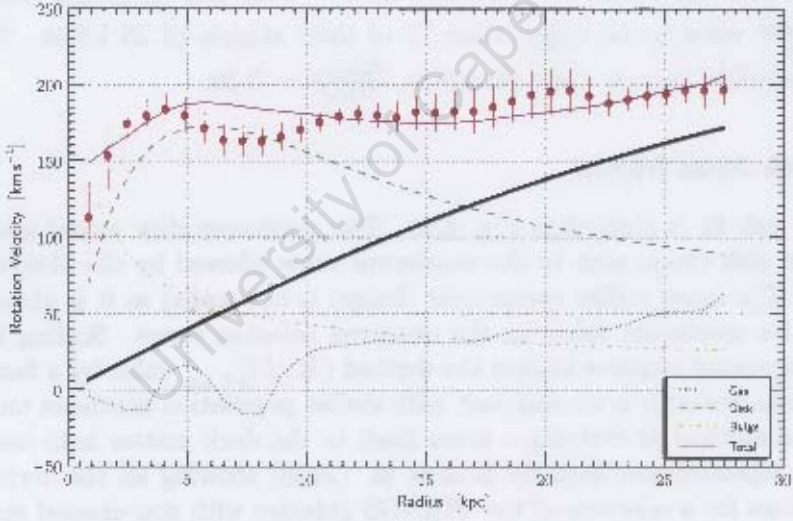

Figure 4.13: Mass component distribution as a function of galactocentric radius using the maximum stellar disk assumption. The line styles are the same as in Fig. 4.11. The outer stellar disk component has been scaled by a factor of 3.77 resulting in a $(M/L)^{*}_{3.6\ \mu m} = 2.22$. With this adopted maximum stellar contribution, dark matter still dominates the outer parts of NGC 1512 ($R > 17$ kpc)

This factor of 4 is expected to increase for the remainder of the HI disk. The maximum disk model has $\frac{M_{baryons}}{M_{DM}} = 0.70$. Comparison with de Blok and McGaugh (1997) finds this maximum disk $\frac{M_{baryons}}{M_{DM}}$ value to be larger than 20 of their sample

of 23 LSBs. The $\frac{M_{Baryons}}{M_{DM}}$ ratios calculated from both the mass models lie within the range of the de Blok and McGaugh sample. Both values are however towards the high end as illustrated by the histogram in Fig. 4.14.

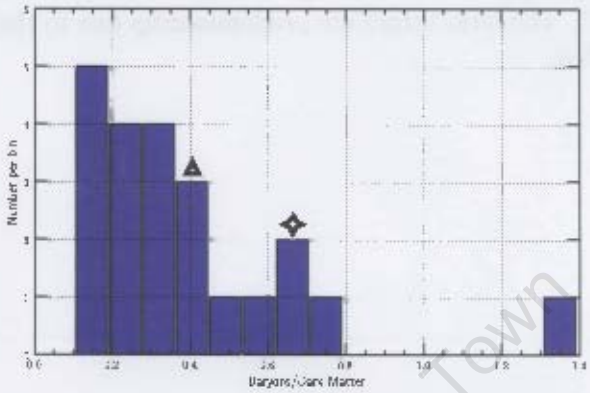

Figure 4.14: Histogram of the baryon-DM ratio of 23 LSBs from de Blok and McGaugh (1997). The triangle represents NGC 1512's baryon-DM ratio of 0.47 assuming the derived $(M/L)^{*}_{3.6\ \mu m} = 0.59$. The star represents the baryon-DM ratio assuming the maximum disk model, which implies a $(M/L)^{*}_{3.6\ \mu m} = 2.22$.

These results find NGC 1512 to be a dark matter dominated galaxy, however less so than than values determined for a sample of 23 LSB galaxies. This dominance is also prevalent when the $(M/L)^{*}_{3.6\ \mu m}$ value is set to its upper limit, but only at $R > 17$ kpc.

4.3 Extended Rotation Curve Models

The rotation curve and mass models in the previous section only considered the inner radii < 27.5 kpc (filling factor > 50 %). This limit was used to work with a high fidelity rotation curve. The analysis is now expanded to incorporate the outer part of the HI disk, as well as the isolated HI cloud at $R = 1600''$ to investigate the kinematics and study of the outer dark matter halo. It assumes that the gas is moving in circular orbits. Although this is unlikely, it does provide a qualitative view of the global kinematics.

The same method as for the inner rotation curve is applied to determine the extended rotation curve. The adopted dynamical centre and systemic velocity values are identical to the inner 27.5 kpc determination. This is an assumption, as the dynamical centre could in principle vary as a function of radius (e.g. galaxy

University of Cape Town

warps, lopsidedness).

With the dynamical centre and systemic velocity in place, the extended rotation curve analysis begins with the above parameters fixed. This is illustrated in Fig. 4.15. Immediately apparent in these plots is the increase in uncertainty beyond a radius of 1000". The large errors are predominantly due to the low filling factor of the outer HI disk.

University of Cape Town

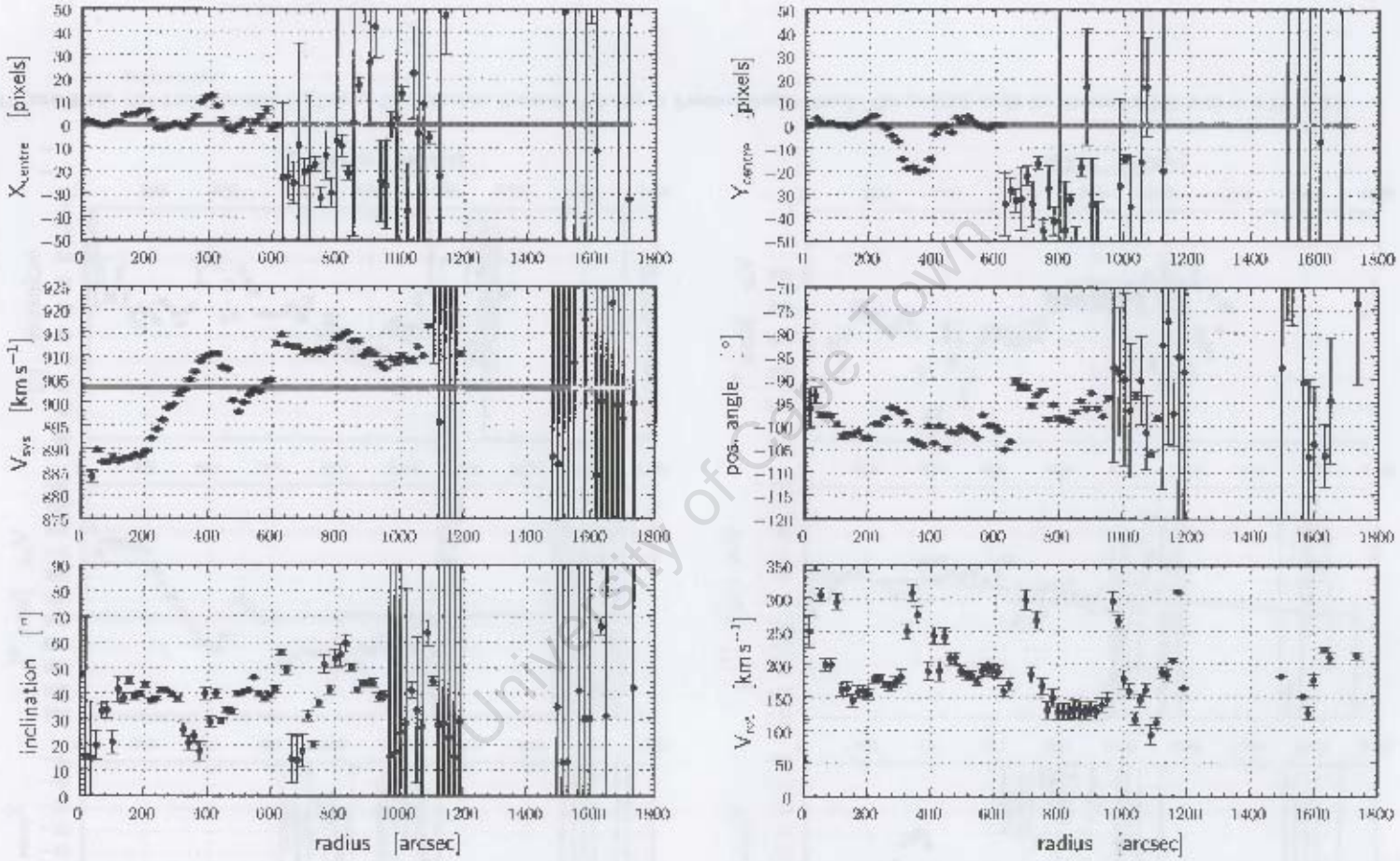

University of Cape Town

Figure 4.15: Full Disk Iteration 3: Central Co-ordinates and Systemic Velocity are fixed as the inner 27.5 kpc model. The y-axis limits are chosen for consistency with later plots, causing some data points and error bars to extend beyond the figure.

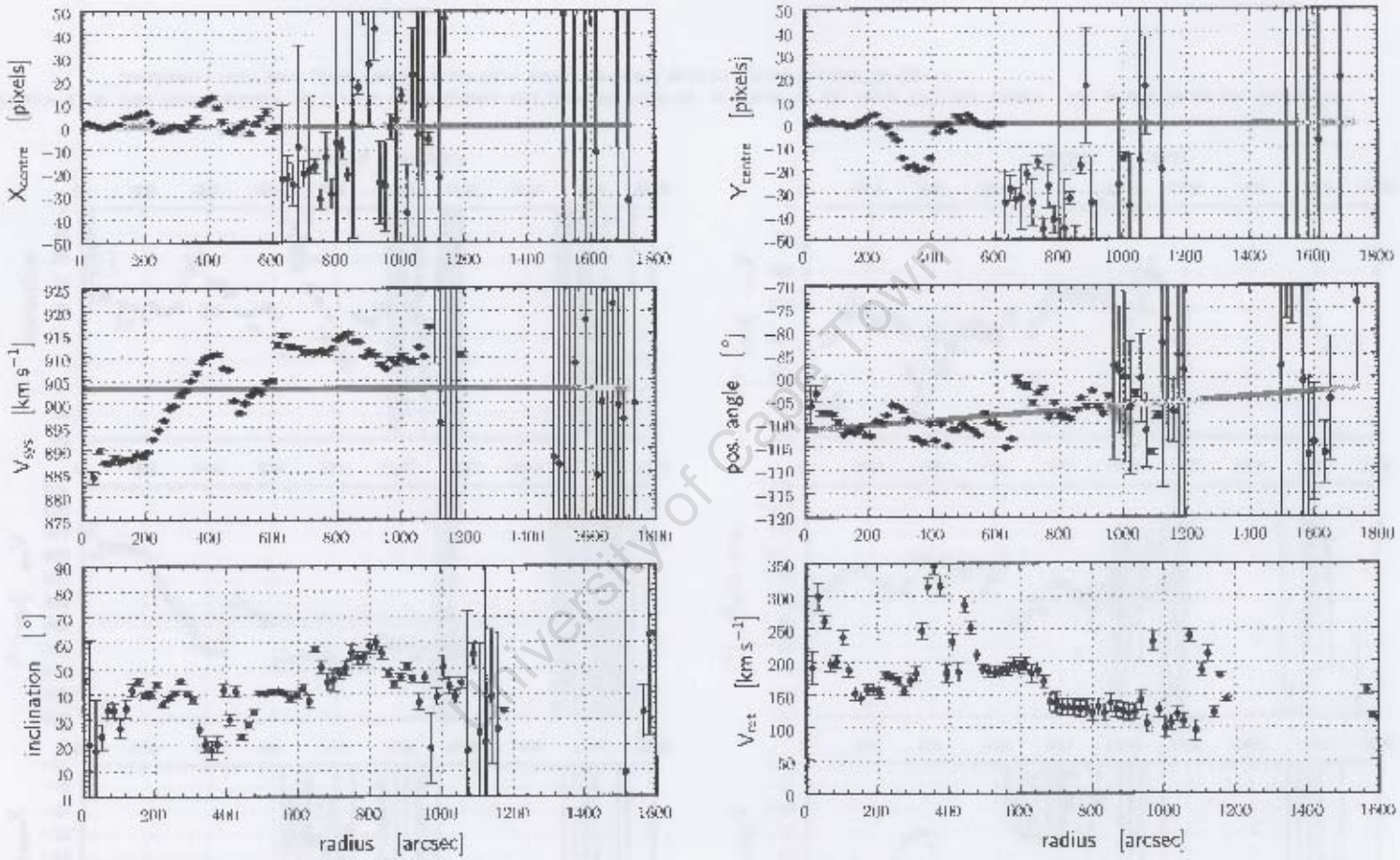

University of Cape Town

Figure 4.16: Full Disk Iteration 4: Central Co-ordinates, Systemic Velocity & Position Angle Fixed. The position angle for the entire disk is fit to a 1st order polynomial.

Inspection of the three dimensional HI cube indicates that the gas in the outer disk is in a different plane (in position-velocity space) to the galaxy. This could be as a result of a tidal history or interaction with the intergalactic medium. Two of the range of possible models are investigated in this study:

Model (a) assumes that the outer disk of NGC 1512 has lost angular momentum due to the tidal or intergalactic medium interaction, and therefore lost rotation velocity. This first model will assume a constant inclination value as derived from the inner 27.5 kpc rotation curve model. This will be labeled the **Bootstrap Model**.

Model (b) assumes a flat rotation curve, which is observed for the majority of galaxies. This model will be referred to as the **Inclination Free Model**.

Fig. 4.16 illustrates the case where the central co-ordinates, systemic velocity and position angle of the entire HI disk have been modeled and fixed.

University of Cape Town

4.3.1 Bootstrap Model

There are a number of effects that would invalidate applying the same inclination model to the outer half of the HI disk (e.g. interaction with the intergalactic medium, galaxy interactions), but it does have the advantage of providing a 'benchmark' to compare the dynamics of the outer and inner halves of the disk. In Fig. 4.17, the result of applying such a fixed inclination to the gas in the outer disk is displayed. The adopted model is illustrated by the thick, grey line in the bottom left panel. The resultant rotation velocities show a sharp decrease at $R \sim 30$ kpc to an approximate value of $V_{rot} \sim 140\ \mathrm{km\,s^{-1}}$.

This can be interpreted as gas that has experienced a decrease in angular momentum. A change in angular momentum could likely have resulted from a tidal interaction with a neighbouring galaxy (NGC 1510 or others). This scenario is explored further in Chapter 6, where the local environment of NGC 1512 is studied on a larger scale.

The total dynamical mass derived from the Bootstrap Model is $M_{dyn} = 2.8 \times 10^{11}\ \mathrm{M}_{\odot}$. This value is comparable to the dynamical mass inferred for the inner 27.5 kpc ($M_{dyn} = 2.5 \times 10^{11}\ \mathrm{M}_{\odot}$). These are high masses for NGC 1512's morphological type, however they are still within a plausible range compared with the Sab sample of Roberts & Haynes (1994).

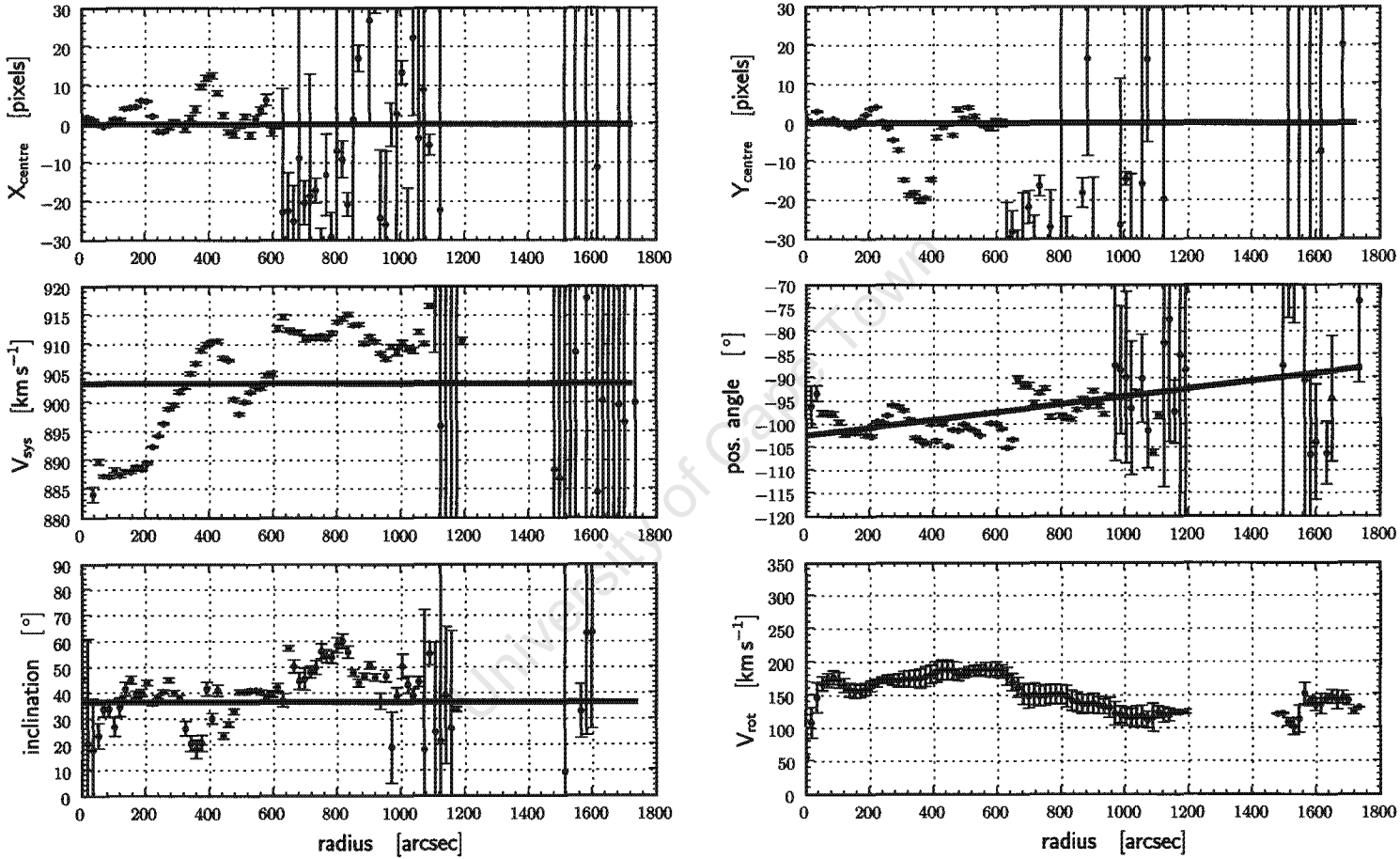

Figure 4.17: Iteration 5A: Inclination Fixed. Inclination is fixed to the model determined for the inner 27.5 kpc of the HI disk. Note the resultant rotation velocities (bottom right).

Figure 4.18 displays the extended version (out to $R = 76$ kpc, compared to $R = 27.5$ kpc) of the rotation velocities as derived with the Bootstrap model. If a constant inclination is assumed, the isolated HI cloud appears to be at a similar rotational velocity. This is explored further in Chapter 6 utilising single dish radio observations of a much larger volume around NGC 1512.

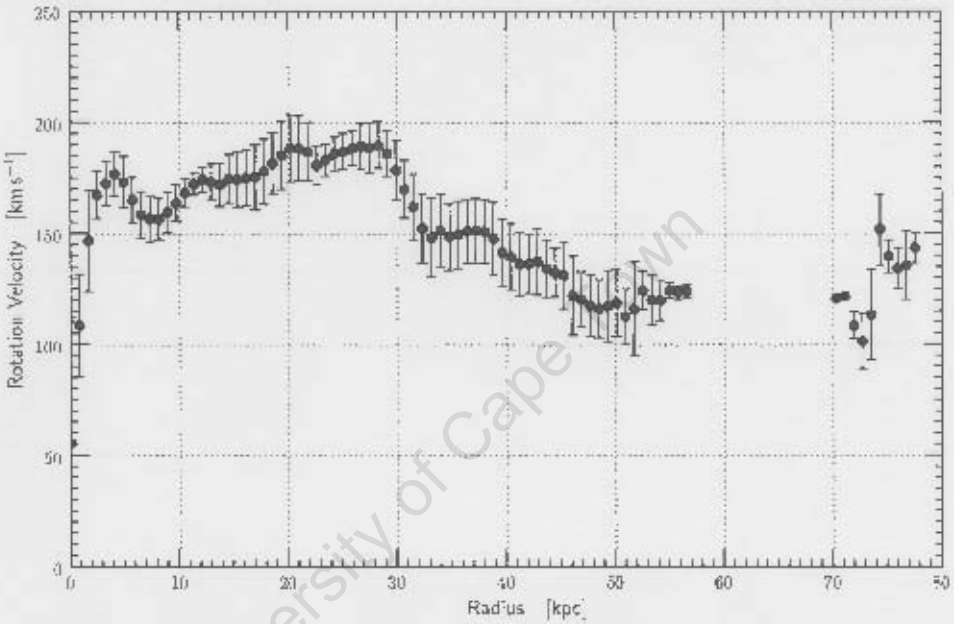

University of Cape Town

Figure 4.18: Larger version of the resultant velocities derived in the Bootstrap Model (Fig. 4.17).

4.3.2 Inclination Free Model

The Inclination Free Model is based on the assumption that the rotation curve remains flat out to the outermost radii ($R \sim 80$ kpc). Therefore, the outer half of the HI disk and the isolated HI cloud will have a fixed rotation velocity $V = 196.7$ km s^{-1}. Such an extended flat rotation curve implies a dynamical mass of $M_{dyn} = 7 \times 10^{11}$ M$_\odot$ and therefore a dark matter halo mass 2.5 times greater than that of the Bootstrap Model ($M_{dyn} = 2.8 \times 10^{11}$ M$_\odot$). The inferred dynamical mass is a factor ~ 3.5 greater than the mass range 75 percentile for Sab galaxies found by Roberts & Haynes (1994). Such a large deviation may imply that the Inclination Free Model is not consistent with the derived masses

of galaxies of the same morphological type. However, it must be considered that the total mass has been sampled to large radii due to the extended HI distribution of NGC 1512. It therefore appears that dynamical mass may not be the most accurate method to make deductions on the geometrical model of the galaxy.

Figure 4.19 displays the result of fixing this assumed flat rotation curve allowing inclination to be a free parameter.

University of Cape Town

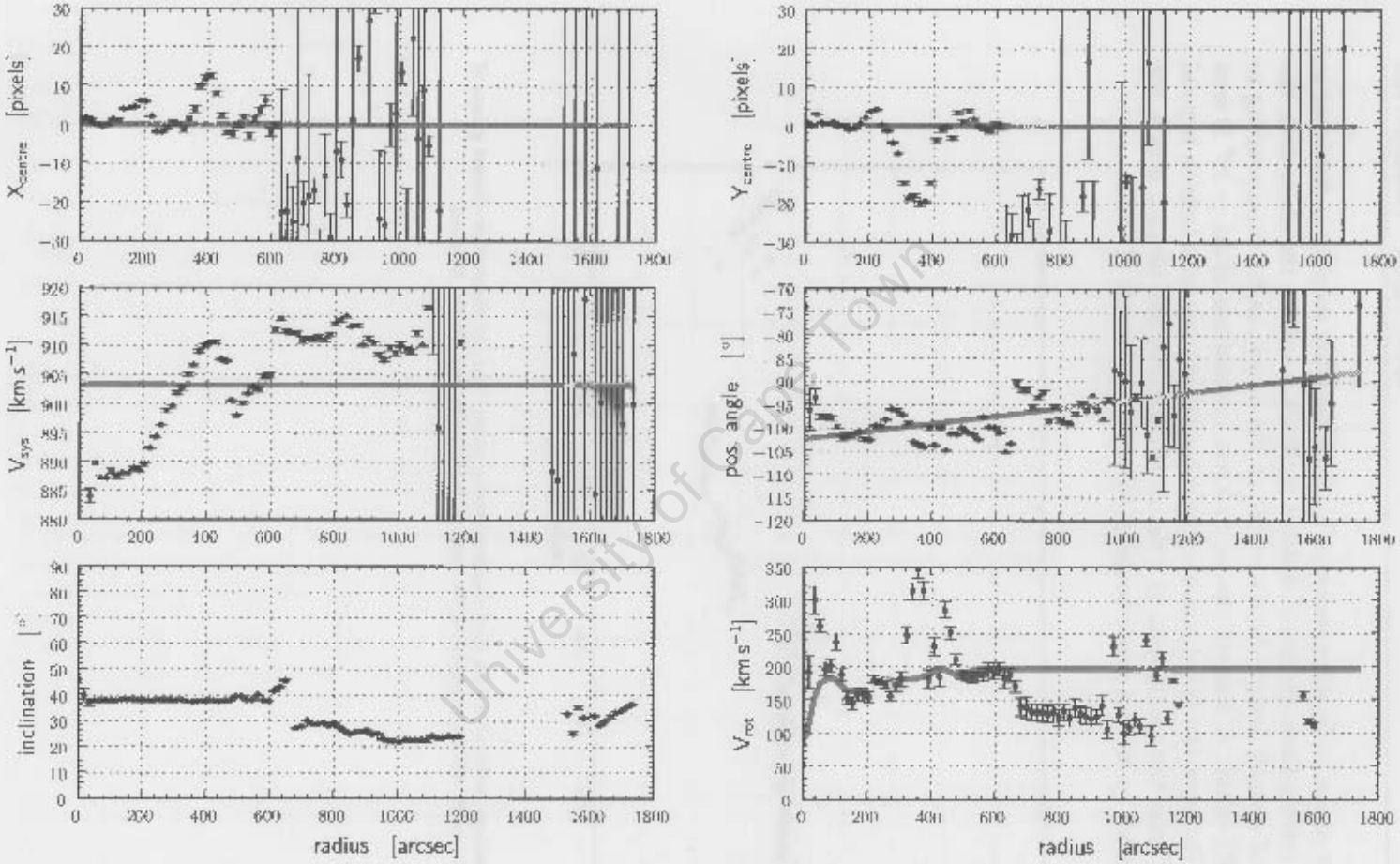

University of Cape Town

Figure 4.19: Iteration 5B: Rotation Velocity Fixed. The derived rotation curve from the inner 27.5 kpc is extended under the assumption that it remains flat (grey line, bottom right panel). These velocities are fixed to calculate the resultant inclination fits (bottom left).

The result of the inclination variation for fixed rotation velocity is displayed in Fig. 4.20. It reveals three groups of distinct inclination values, the inner disk, the outer disk and a small group of data points at the largest radii corresponding to the isolated HI cloud. A discrete change to lower inclinations of $\Delta i \sim 10^{\circ}$ is seen at 27.5 kpc. However the fitted values vary in a relatively smooth fashion beyond this radius. Under the assumption of a flat rotation curve and circular orbits, the HI cloud appears to be in a plane between the inner and outer HI disk.

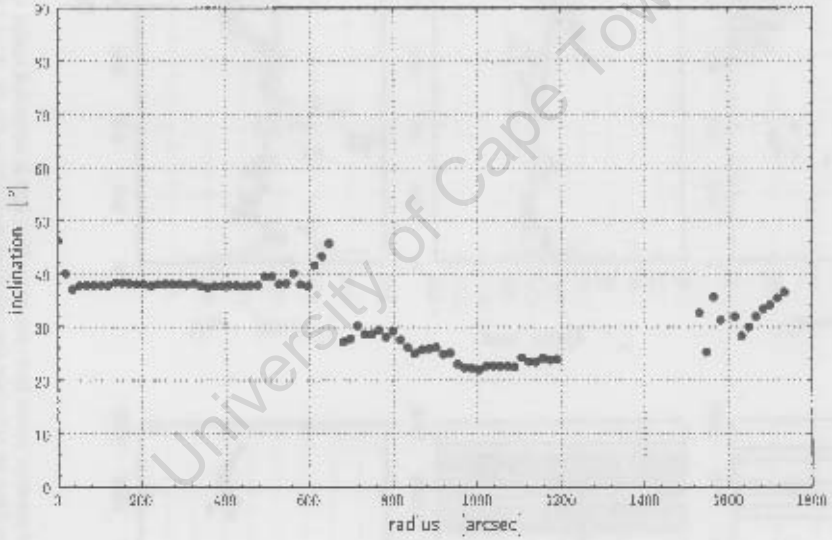

University of Cape Town

Figure 4.20: Resultant inclinations for a fixed rotation velocity model. The plot shows three distinct groups of data points which correspond to the inner disk, outer disk and isolated HI cloud.

Chapter 5

Star Formation

This chapter will investigate the relation between HI and the instantaneous star formation rate in NGC 1512. Combining this with the kinematic analysis from Chapter 4 will aid the understanding of the galaxy's recent star formation and the interaction scenario. The combined ultraviolet and mid-infrared star formation rate indicators are introduced, followed by an overview of the currently understood HI-SFR correlation. The HI-SFR relation in NGC 1512 is probed at local scales and using radial bins. Environmental effects, both internal and external, will be probed with the use of radial profiles of the star formation efficiency.

5.1 Ultraviolet and Infrared Star Formation Rate Indicators

The intensity of emission from young, massive stars peaks in the ultraviolet region of the electro-magnetic spectrum. Flux measured in this band is an excellent indicator of the current *massive* star formation rate in spiral and irregular galaxies (Kennicutt, 1998; Donas et al., 1987). However, short wavelengths ($\lambda < 7000$ Å) are increasingly affected by dust attenuation, and the ultraviolet is only an optimal tracer of unobscured star formation (Calzetti, 2008).

Regions of star formation are frequently observed to be high in dust content. Therefore, a second SFR indicator must be used to overcome the dust attenuation. Dust is heated by UV photons, and re-radiates this energy in the mid-IR (Calzetti et al., 2007; Kennicutt, 2008). Spitzer has a 24 μm observing wavelength aimed at investigating exactly this. Combined with the FUV, one can create star formation rate maps of a hybrid nature that are strongly complementary in that they trace both obscured and unobscured star formation.

University of Cape Town

This was noted by Kennicutt (1998), however has not been implemented until recently (Bigiel et al., 2008; Leroy et al., 2008). We will employ this method of SFR estimation in this study. This is particularly relevant in the case of NGC 1512 when considering the extent of the UV emission which is significantly larger than in the optical. Furthermore, as NGC 1512 is a LSB galaxy, it is likely to be relatively low in dust content, favouring the use of star formation indicators not exclusively reliant on the radiation from dust itself.

5.2 SFR-HI Surface Density Relation

Schmidt (1959) was the first to derive a relation between gas and star formation. He compared the stellar and gas *volume density*, ρ, perpendicular to the Galactic plane. In his formalism of $\rho_{SFR} \propto (\rho_{gas})^N$, Schmidt found $N \sim 2$.

Kennicutt (1989, 1998) took the work of Schmidt a step further through a study of star formation and gas content in 61 nearby 'normal' spiral galaxies and 36 starburst galaxies. He determined the relation between the disk-averaged total gas surface density, Σ_{gas}, and star formation rate surface density, Σ_{SFR}. The gas surface density is comprised of both molecular and atomic hydrogen components ($\Sigma_{gas} = \Sigma_{HI} + \Sigma_{H2}$). For his subsample of 'normal' spiral galaxies, Kennicutt found $N = 2.47 \pm 0.39$.

Since then increasing research has been put into the relation of gas and star formation. Approaches can be roughly divided into three groups: those that attempt to relate either Σ_{HI}, or Σ_{H2}, or both (Σ_{gas}) to the ongoing star formation activity.

Results from these studies are varied, with a derived value of N typically in the range 1 – 3. The large scatter is likely due to the differing spatial resolutions and diverse methodologies adopted in star formation rate estimation which probe a range of different physical phenomena. It must be noted, that only a limited number of studies have investigated the $\Sigma_{HI/H2/gas} - \Sigma_{SFR}$ relation at high spatial resolution (< 1 kpc).

In the following we will investigate the Σ_{HI} relation to Σ_{SFR} in the NGC 1512 system. An advantageous aspect of our multi-wavelength data is that all data products are of high spatial resolution. This enables local small-scale (760 pc) comparisons of the star formation rate surface density and HI surface density. Furthermore, it enables the radial profile to be investigated in relatively fine

University of Cape Town

(760 pc) radial bins.

While the pixel-by-pixel method probes the HI-SFR surface density relation on these small scales, the radial profiles enable these quantities to be put into context of their environment. The latter is particularly applicable in the galaxy interaction scenario of NGC 1512 with NGC 1510.

5.2.1 Pixel-By-Pixel Analysis

Section 3.5 described the method for combining the far ultraviolet and mid-IR maps of NGC 1512 which will allow the comparison of star formation with the HI total intensity map. Fig. 5.1 displays a pixel-by-pixel plot of star formation rate surface density, Σ_{SFR}, as a function of HI surface density, Σ_{HI}. These points are colour-coded into three domains of the galaxy - the core (crosses), the regularly rotating outer disk (squares), and the tidal debris (filled circles). The core is defined as all radii within the optical ring ($R < 7$ kpc). The outer radius of the regularly rotating disk is defined as in Sec. 4.1.1. The noise level of the Σ_{SFR} is 1.5×10^{-4} $M_\odot\,pc^{-2}\,year^{-1}$.

Figure 5.1 reveals two distinct Σ_{SFR} peaks occurring at different HI surface densities. The two peaks belong to two regions in the galaxy: the core and the regularly rotating HI disk. The peaks are separated by over an order of magnitude in Σ_{HI}. This is likely due to the core being dominated by molecular, not atomic, hydrogen (Bigiel et al., 2008; Goldsmith et al., 2007). Bigiel et al. (2008) find their sample of 8 spiral galaxies to all be dominated by molecular hydrogen inside of 0.4 R_{25}. If we assume the x-axis in Fig. 5.1 to represent the sum of both atomic and molecular hydrogen, Σ_{gas}, the lower peak may well be shifted closer to $\Sigma_{HI} \sim 10$ $M_\odot\,pc^{-2}$. Bigiel et al. (2008) derive radial profiles of the HI and H_2 mass surface density for their sample of 13 spiral galaxies. They find their sample of 8 spiral galaxies to have a H_2/HI ratio of ~10 in the galaxy centre. This is roughly consistent with the difference in the Σ_{HI} peaks seen in Fig. 5.1.

Figure 5.1 also reveals a sharp HI upper limit at $\Sigma_{HI} \sim 10$ $M_\odot\,pc^{-2}$. This value most likely coincides with the critical density at which atomic hydrogen converts to molecular form. The value is consistent with Bigiel et al. (2008) who find 95% of the neutral gas to have a surface density $\Sigma_{HI} < 9$ $M_\odot\,pc^{-2}$ for their sample of 8 spiral galaxies. Similar results were found at lower spatial resolutions by Wong & Blitz (2002) and Martin & Kennicutt (2001). A histogram of the HI surface density in each of the three regions is displayed in Fig. 5.2. This illustrates how the HI density varies in these regions. The HI surface density has its peak value at $\Sigma_{HI} = 12.7$ $M_\odot\,pc^{-2}$. This is significantly larger than that quoted by van der

University of Cape Town

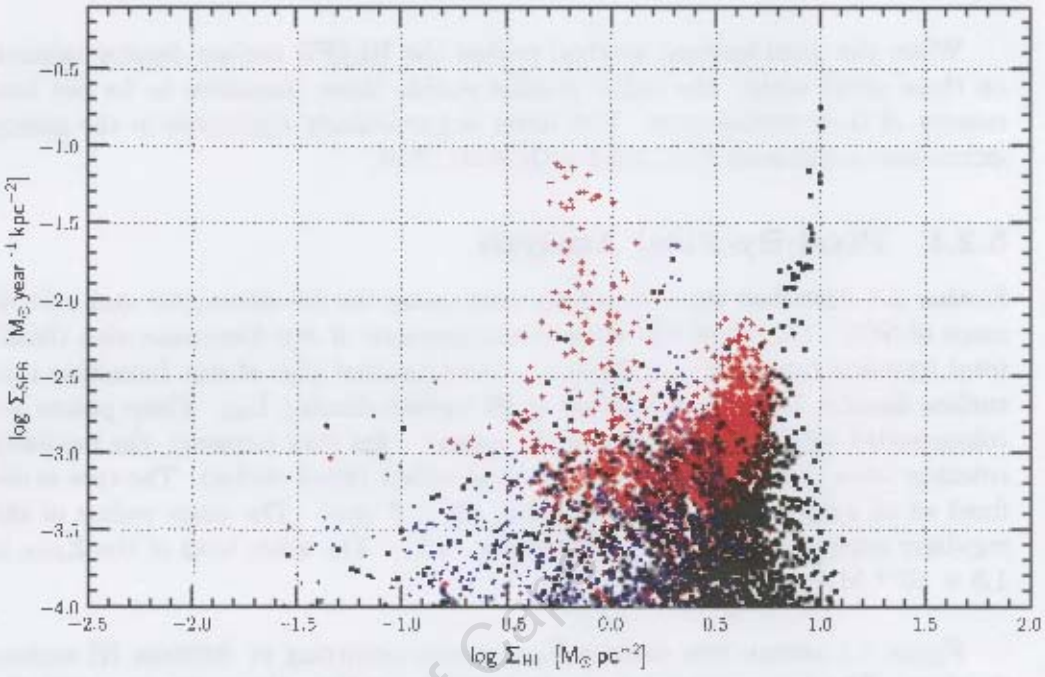

Figure 5.1: Star formation rate surface density as a function of corresponding HI density. Red crosshairs represent points in the core of the galaxy, black squares correspond to the regularly rotating HI disk, and blue circles to what is considered to be tidal material.

Hulst et al. (1992) who investigated the HI surface density of 8 LSBs with the VLA. He found typical peak values of $\Sigma_{HI} \sim 4 - 6$ $M_\odot$ pc^{-2} (log $\Sigma_{HI} \sim 0.6 - 0.78$ in log space). They find this to be below the critical density for star formation following Kennicutt (1989), and suggest this as the reason for the low surface brightness disk. The slightly higher Σ_{HI} values observed in NGC 1512 may be due to: (1) The larger gas density frequently observed in the spiral arms of interacting spiral galaxies (e.g. M81, Yun, Ho & Lo 1994), (2) NGC 1512's HI surface density is not that of a typical LSB described in van der Hulst (1992). The bin centred at $\Sigma_{HI} \sim 4$ $M_\odot$ pc^{-2} (log $\Sigma_{HI} = 0.6$) contains the greatest number of data HI data points.

Figure 5.1 reveals no obvious relation on local (760 pc) scales as both quantities vary by ~ 2.5 orders of magnitude. This is consistent with the findings of Bigiel et al. (2008). But, this result is in stark contrast with the observed *global* correlation of Σ_{HI} with star formation derived by Kennicutt (1998). While this

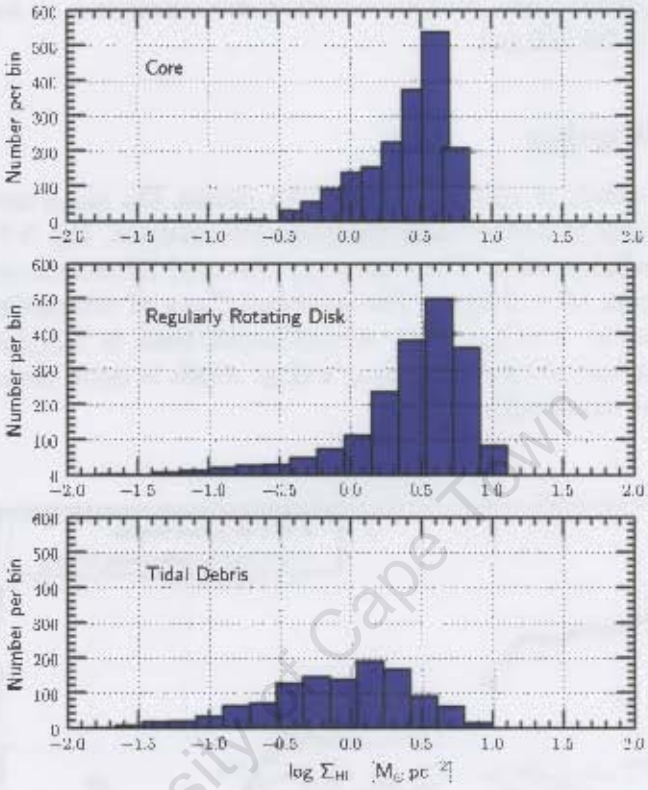

Figure 5.2: Histogram of HI surface density within each defined region.

University of Cape Town

global relation between total gas and total SFR for galaxies is relatively well constrained (assuming a conversion from neutral to total gas), this does not seem to hold on local scales as suggested by Fig. 5.1.

Stars form in giant molecular clouds (GMCs). Therefore, we expect an anti-correlation between Σ_{HI} and Σ_{SFR} if GMCs are resolved. However, the scale of GMCs is typically $\sim$ 50–100 pc, substantially smaller than 760 pc resolution of the HI and SFR surface density maps. Tamburro et al. (2008) investigate the distance between HI and star formation rate peaks using high resolution (6") HI maps and the same star formation rate map recipe as the current study. They find typical offsets of $\sim$ 100 pc.

Figure 5.1 may be suggestive of a continuum between the strong relationship of Σ_{HI} and Σ_{SFR} on global scales, and the expected anti-correlation on scales that GMCs are resolved ($\sim$ 50–100 pc).

5.2.2 Radial Binning

To identify possible trends of Σ_{HI} and Σ_{SFR} with radius, the maps are divided into the same tilted-rings as derived from the kinematic analysis. Fig. 5.3 displays a plot of these two radial profiles. The commonly observed HI central depression is seen in the inner radii ($R < 3$ kpc). The increased Σ_{SFR} of companion galaxy NGC 1510 can be seen at $\sim$ 14 kpc. The second largest peak in Σ_{SFR} is located at $R \sim 3$ kpc and originates from the galaxy's ring, which is quite prominant in optical and ultraviolet wavelengths.

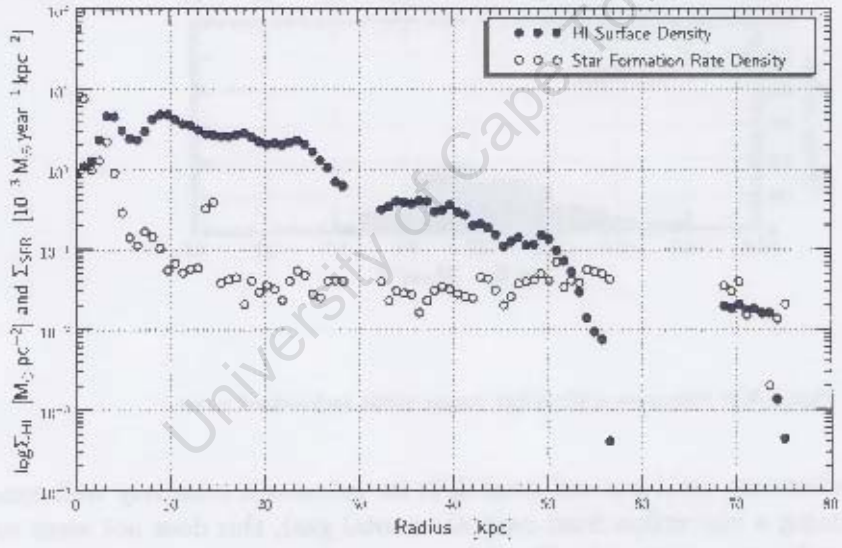

Figure 5.3: Radial profiles of Σ_{HI} and Σ_{SFR}. Note that Σ_{SFR} is scaled by 10^3 to enable easier visual comparison of the two profiles.

Figure 5.4 displays the relation between the radial profiles of Σ_{HI} and Σ_{SFR}. This is the equivalent of the pixel-by-pixel plot in Fig. 5.1, however, all pixels have been averaged into radial bins, each the width of the resolution of the HI map. This averaging effect loses the local information, however it increases the signal-to-noise, particularly towards the outer radii.

University of Cape Town

Binning the pixels into radial ellipses appears to reveal a clearer picture than the pixel-by-pixel plot (Fig. 5.1). It suggests a star formation threshold at ~ 2.5 $M_\odot\,pc^{-2}$ ($\log \Sigma_{SFR} \sim 0.4$). It must be reiterated that the core (red crosses) of a typical (< Scd) spiral galaxy is usually dominated by molecular hydrogen.

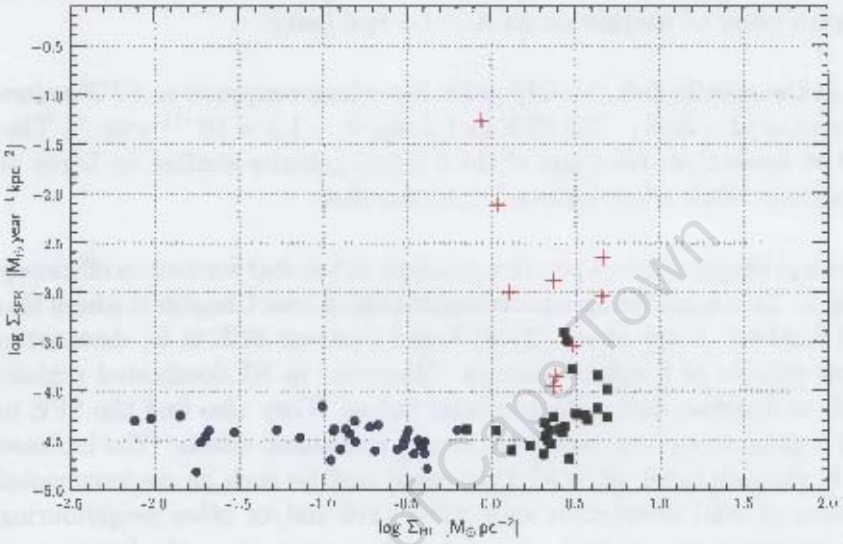

Figure 5.4: Star formation rate surface density as a function of corresponding HI surface density. Pixels from Fig. 5.1 are binned up in radial annuli of width 17". The three regions of star formation are denoted with the same symbols as in Fig. 5.1. Note Σ_{SFR} shows a significant increase at $\Sigma_{HI} \sim 2.5$ $M_\odot$ pc^{-2} ($\log \Sigma_{SFR} \sim 0.4$).

University of Cape Town

5.3 Star Formation Efficiency

The star formation analysis is expanded further by regarding the star formation efficiency parameter (SFE). This is defined as the percentage of presently available gas converted into stars per year. It is calculated with the expression:

$$SFE = \frac{\Sigma_{SFR}}{\Sigma_{HI}} \qquad \left[\text{year}^{-1}\right] \tag{5.1}$$

where Σ_{SFR} has units $M_\odot\,\text{year}^{-1}\,\text{pc}^{-2}$; and Σ_{HI} has units $M_\odot\,\text{pc}^{-2}$. Following Leroy et al. (2008), the errors are defined as:

$$\sigma = \frac{\sigma_{RMS}}{\sqrt{N_{pix,ring}/N_{pix,beam}}} \tag{5.2}$$

where σ_{RMS} is the RMS scatter within each tilted ring, $N_{pix,ring}$ is the number of pixels in the ring, and $N_{pix,beam}$ is the number of pixels per resolution element.

The star formation efficiency (SFE) shows a clear dependence on radius. The SFE decreases out to a radius of $1.2 \times R_{25}$ ($R = 15.2$ kpc). There is a distinct local effect in the vicinity of NGC 1510 at $R \sim 14$ kpc. The SFE increases by approximately an order of magnitude for a ~ 1.5 kpc band.

The SFE in the middle disk (15–23 kpc) is low when compared to SFE values reported in Leroy et al. (2008). The SFE at $1.2\ R_{25}$ is $\sim 1.2 \times 10^{-11}$ year^{-1}. This is a factor of two lower than than any of the 8 spiral galaxies studied by Leroy et al. (2008), consistent with a low surface brightness disk.

Figure 5.5 surprisingly shows a positive gradient in the star formation efficiency from 23 – 50 kpc. This could be an environmental effect (see Chapter 6 where this is investigated further). Leroy et al. (2008) found constant SFE in H_2 dominated regions in their sample of 8 spiral galaxies. However, in HI dominated regions they find SFE to decrease with galactocentric radius. They also find the SFE in HI-dominated regions to be more sensitive to environmental effects. The increase in SFE seen in the outer disk of NGC 1512 could well be such an environmental effect in the form of tidal interaction with NGC 1510 and/or other neighbouring galaxies. This interpretation must be treated with caution given the large errorbars.

NGC 1512's interaction with neighbouring NGC 1510 has clearly initiated recent star formation as traced by the GALEX FUV and Spitzer MIPS 24mum maps. There appears to be a weak HI-SFR correlation at small-scales, however there is an apparent star formation threshold if the pixels are averaged into radial bins. The increase in star formation efficiency in the outer radii could tentatively be interpreted as a larger interaction scenario. An analysis of the local environment is the theme of Chapter 6.

University of Cape Town

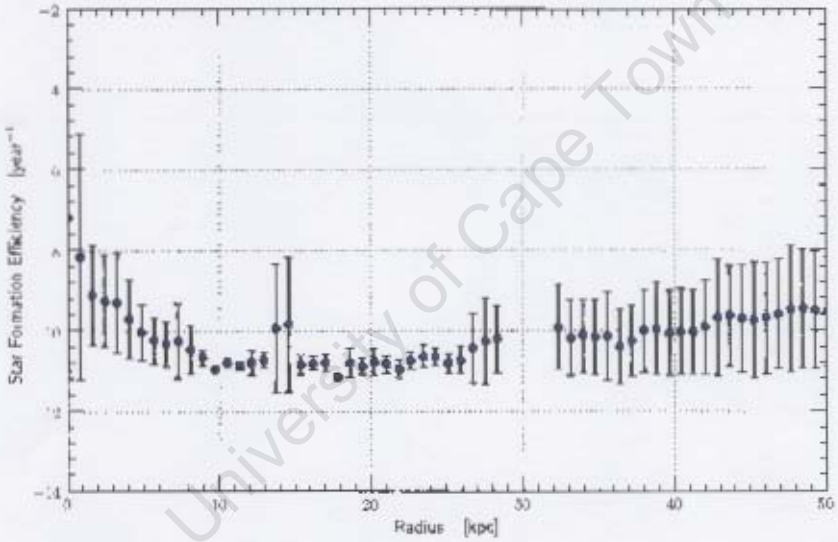

University of Cape Town

Figure 5.5: Star formation efficiency as a function of radius. Note the local effect of neighbouring galaxy NGC 1510 at ~ 14 kpc, as well as the apparent 1.5 dex increase in star formation efficiency between 23 – 30 kpc.

Chapter 6

The Tidal Dwarf Galaxy and Local Environment

Environmental effects have a strong influence on a galaxy's morphology, kinematics and star formation history. This is seen through a galaxy's interaction with the intergalactic medium (IGM), strong radiation fields, and with other galaxies (Jones and Forman, 1990; Hickson, 1999; Feretti and Venturi, 2002). This chapter investigates the environment of NGC 1512, beginning with a more detailed analysis of the newly discovered HI cloud discussed in Chapter 2. Additionally, the HI Parkes All Sky Survey (HIPASS) detection of NGC 1512 is compared to the ATCA HI map. These HIPASS observations enable a larger area coverage of the NGC 1512 system, however with much lower spatial resolution (~15'). The goal of including HIPASS observations in this study is to search for additional diffuse HI emission outside the field-of-view of the ATCA observations. Intergalactic HI is observed to trace galaxy interactions (e.g. the M81 group; Yun, Ho and Lo 1994) and low column density features may provide clues to the history of the NGC 1512 group.

University of Cape Town

6.1 Tidal Dwarf Galaxy?

6.1.1 HI Data

Chapter 2 reported the discovery of an isolated HI cloud associated with the NGC 1512 system. The cloud is at a projected distance of 72 kpc south-west of the centre NGC 1512 and has an HI mass of $M_{\rm HI} = 6.5 \times 10^7$ (D/9.8 Mpc)^2 $M_\odot$. Its angular extent of $\Delta\theta \sim 6' \times 4'$ corresponds to a physical extent of $\Delta R = 1.1 \times 1.7$ kpc (in the plane of the sky). The cloud spans $\Delta v \sim 21$ km s^{-1} in velocity

Chapter 6

The Tidal Dwarf Galaxy and Local Environment

Environmental effects have a strong influence on a galaxy's morphology, kinematics and star formation history. This is seen through a galaxy's interaction with the intergalactic medium (IGM), strong radiation fields, and with other galaxies (Jones and Forman, 1990; Hickson, 1999; Feretti and Venturi, 2002). This chapter investigates the environment of NGC 1512, beginning with a more detailed analysis of the newly discovered HI cloud discussed in Chapter 2. Additionally, the HI Parkes All Sky Survey (HIPASS) detection of NGC 1512 is compared to the ATCA HI map. These HIPASS observations enable a larger area coverage of the NGC 1512 system, however with much lower spatial resolution (~15'). The goal of including HIPASS observations in this study is to search for additional diffuse HI emission outside the field-of-view of the ATCA observations. Intergalactic HI is observed to trace galaxy interactions (e.g. the M81 group; Yun, Ho and Lo 1994) and low column density features may provide clues to the history of the NGC 1512 group.

University of Canterbury Library

6.1 Tidal Dwarf Galaxy?

6.1.1 HI Data

Chapter 2 reported the discovery of an isolated HI cloud associated with the NGC 1512 system. The cloud is at a projected distance of 72 kpc south-west of the centre NGC 1512 and has an HI mass of $M_{\rm HI} = 6.5 \times 10^7$ (D/9.8 Mpc)^2 $M_\odot$. Its angular extent of $\Delta\theta \sim 6' \times 4'$ corresponds to a physical extent of $\Delta R =$ 1.1×1.7 kpc (in the plane of the sky). The cloud spans $\Delta v \sim 21$ km s^{-1} in velocity

space.

Figure 6.1 displays the ATCA HI map of the cloud in grayscale. Superimposed are contours of HI column density. The map shows two HI peaks, both of which have column density $N_{\rm HI} \sim 10^{21}$ cm^{-2}. The cloud appears to be quite fragmented, as defined by the 1.7×10^{20}cm^{-2} contour which is at a 5-σ confidence level for that region of the map. HI in irregular galaxies is observed to be 'clumpy', as reported in a catalogue of HI complexes within the Large Magellanic Cloud (Kim et. al., 2007).

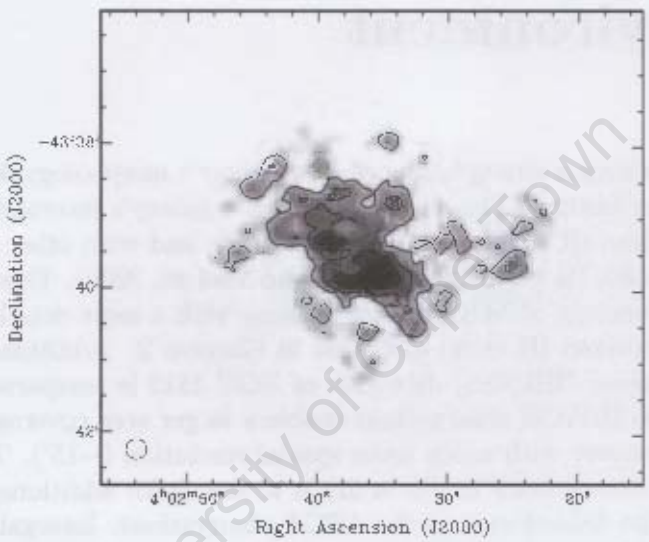

Figure 6.1: HI map of isolated HI cloud shown in grayscale with superimposed contours of HI column density which range from $N_{HI} - 1.7$ and 8.5×10^{20} cm^{-2} and increase in steps of $\Delta N_{\rm HI} = 1.7 \times 10^{20}$ cm^{-2}. The ATCA synthesised beam is shown in the bottom-left.

If the data is taken at face value, there are roughly eight 'detached', $D > 17'$ (760 pc) HI complexes surrounding the HI cloud in Fig. 6.1, as defined by the 1.7×10^{20}cm^{-2} contour. The masses of each of these HI complexes are compared to the 195 in the LMC catalogue generated by Kim et al. (2007) in Fig. 6.2. Rectangular bars represent a histogram of the mass of LMC HI complexes. Each star ($\star$) represents one of the eight loosely defined HI complexes seen in Fig. 6.1. The stars are placed in the corresponding mass bin. The comparison illustrates that the HI complexes detected around the HI cloud are towards the high mass end of the distribution of the LMC. Assuming the HI complex mass distribution of the LMC is similar to that of the isolated HI cloud, then it appears we are observing

the high mass end of these complexes. This is as we would expect with a low signal-to-noise ratio and is illustrated in Fig. 6.2. Furthermore, the HI complexes are all comparable to the systhesised beam (bottom left of Fig. 6.2).

It is not the intention to compare the isolated HI cloud with the LMC. The aim is to put the HI complexes into context with arguably the most well-studied irregular galaxy in HI.

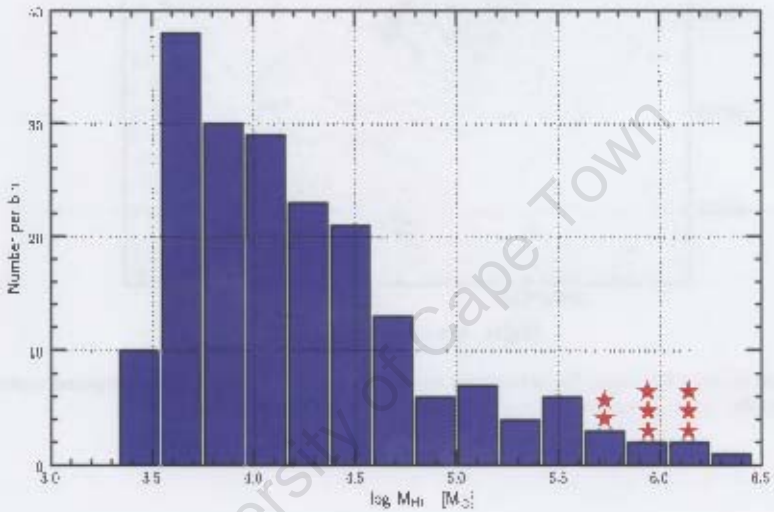

Figure 6.2: Histogram of the mass of HI complexes measured in the Large Magellanic Cloud by Kim et al. (2007). Stars (right) signify masses of HI complexes in the isolated HI cloud from Fig. 6.1.

University of Cape Town

6.1.2 Multi-Wavelength Data

The HI cloud has no optical counterpart in the B and R band Digitized Sky Survey (DSS) fields. There does however appear to be a faint far ultraviolet component. Figure 6.3 displays the GALEX FUV map of the cloud in grayscale with superimposed contours of HI column density. The map reveals FUV emission in the centre of the cloud, between the two HI column density peaks. The peak FUV pixels are at 3-σ above the noise level. No traces of associated FUV emission are seen for the rest of the tidal material in NGC 1512.

The cloud lies outside the field-of-view of the Spitzer IRAC instrument observations of NGC 1512. However, the 24 μm and 70 μm scans of NGC 1512 with the Spitzer MIPS instrument did overlap with the position of the HI cloud. The

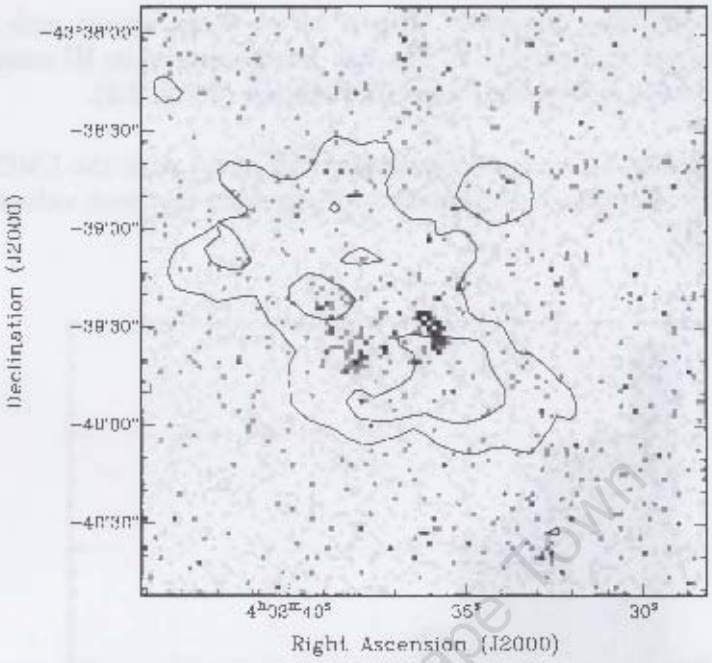

Figure 6.3: Zoom in on isolated HI cloud. Far ultraviolet map shown in grayscale with superimposed contours of HI intensity. Contour values are $N_{HI} = 1.4$ and 3.1×10^{20} cm^{-2}.

University of Cape Town

24 μm map, sensitive to dust heated by star formation, reveals no detection. The 70 μm emission traces cold dust in thermal equilibrium, with a blackbody temperature of 30 – 60 K (Dale et al., 2007). The 70 μm map reveals a 2-σ peak which is co-spatial with the southern peak in the HI cloud. Clearly, deeper observations are required as no deductions can be made from the data currently available.

Tentatively the data can be interpretated as recent star formation (~10 – 100 Myr) occuring in the centre of the cloud. This timescale is based the stellar age-mass relation and continuum UV flux evolution (Kennicutt, 1998; Salim et al., 2007). NGC 1512 has a tidally disrupted disk and the isolated HI cloud is the likely product of an interaction. The isolated HI cloud is therefore a Tidal Dwarf Galaxy candidate (TDGc). Future observations to probe this candidacy are outlined in Chapter 7.

6.2 Comparison of HIPASS and ATCA Maps of NGC 1512

The spatial resolution of the HIPASS and ATCA maps differ by a factor of ~50. The reason for the comparison of these two maps is to probe emission outside the ATCA field-of-view. Furthermore, interferometers are only sensitive to a limiting spatial scale dependent on the intrument's configuration and geometry. This is because an interferometer is a spatial filter that is only sensitive to emission on scales smaller than the angle $\Delta\theta_{max}$. This angle is inversely proportional to the shortest baseline in the array, l_{min}, and is calculated to first order with the equation:

$$\Delta\theta_{max} = \frac{\lambda_{obs}}{l_{min}} \qquad \text{[radians]} \tag{6.1}$$

where λ_{obs} is the wavelength observed. The ATCA HI observations presented in Sect. 2.3.1 have a shortest baseline $l_{min} = 31$ m (in the **210 array**), corresponding to a maximum angular scale of $\theta_{max} = 23.3'$ (66.4 kpc at a distance of 9.8 Mpc). Single dish radio telescopes do not have an upper limit to the spatial scales to which they are sensitive. This is one of the reasons single dish observations frequently measure higher flux levels than interferometers (Wrobel and Walker, 1999; Thompson, 1999).

This phenomenon, combined with the extent of the HIPASS observations, make it complementary to compare the interferometric and single dish HI maps. Fig. 6.2 shows the ATCA map in grayscale. Superimposed are contours of HI column density from a HIPASS total intensity map. The HIPASS map (contours) is made from the summation of 40 velocity channels ($\Delta v = 528$ km s^{-1}) centred on the systemic velocity of NGC 1512, $v_{sys} = 898$ km s^{-1}.

The lowest contour in Fig. 6.2 suggests HI column densities beyond the isolated HI cloud to the south-west. The column density of this lowest contour is > 3-σ of the channel noise level ($N_{chan} = 12.5$ mJy beam^{-1}).

The HIPASS catalogue lists a total mass $M_{\rm HI} = 5.5 \times 10^9$ M$_\odot$ for this galaxy, with a quoted uncertainty of 5% (Koribalski et al., 2004). This mass estimate is 10% larger than the mass determined from the ATCA observations ($M_{\rm HI} = 5 \times 10^9$ M$_\odot$). Although this mass discrepancy is not significant, two contributing factors may be: (a) ATCA's lack of sensitivity to emission of angular scale $\Delta\theta > 23.3'$; and (b) the tenable presence of low column density tidal debris outside of the field-of-view of the ATCA observations.

University of Cape Town

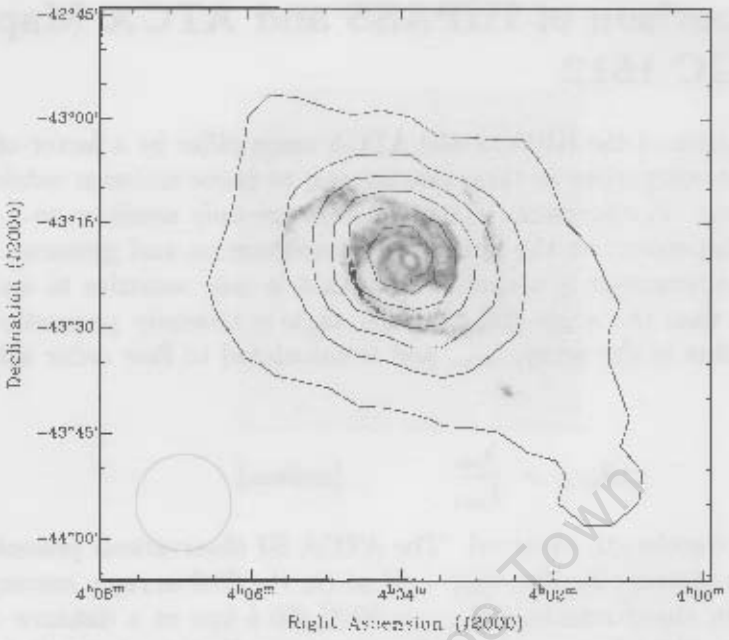

Figure 6.4: ATCA HI map in greyscale. Contours of total HI intensity from HIPASS map made from the summation of 40 velocity channels ($\Delta v = 528$ km s^{-1}). Contours range from $N_{\rm HI} = 3.4 - 23 \times 10^{20}$ cm^{-2} and increase in steps of $\Delta N_{\rm HI} = 4 \times 10^{20}$ cm^{-2}. The contour levels illustrate extended HI emission beyond the isolated HI cloud (south-west). Parkes primary beamwidth is displayed at the bottom left.

Of course, the above two reasons are speculative and further observations are required to probe their validity. These future observations are discussed in Chapter 7.

6.3 Speculation on Previous Interactions

Chapter 2 showed the companion galaxy NGC 1510 to be embedded in the gas disk of NGC 1512. The HI velocity field and ultraviolet maps illustrate this galaxy interaction most clearly. The baryonic mass ratio of the two galaxies is $M_{\rm N1512}/M_{\rm N1310} \sim 100$. As noted already by Hawarden et al. (1979), the relative mass of companion galaxy NGC 1510 may be insufficient for the observed tidal effect of such an extended HI disk. If correct, the companion galaxy NGC 1510 may not be the solitary cause of NGC 1512's disrupted disk. To explore this further we investigate the neighbouring galaxies around NGC 1512.

A $\sim 5° \times 3°$ HIPASS map of the extended environment of NGC 1512 is dis-

played in Fig. 6.5 (grayscale). This is made from the four combined HIPASS cubes described in Sect. 3.2. The map in Fig. 6.5 results from the summation of 89 velocity channels, leading to a total $\Delta v = 1175$ km s^{-1}, to include the full velocity width of the galaxy group. The map is centred on 1108 km s^{-1} in velocity space. White contours from the ATCA HI map are superimposed. The map includes neighbouring galaxies NGC 1487, NGC 1495, ESO 249- G 026 and ARS B035343-440501 (see labels). All the galaxies are within an angular diameter $\theta \sim 160'$, which corresponds to 465 kpc at a distance of 10 Mpc.

The contrast of the map is saturated in order to show the extent of emission beyond the NGC 1512 system. The map is suggestive of intergalactic HI emission, particularly in the proximity of NGC 1512. However, the reality of this emission is uncertain. The intergalactic emission seen in Fig. 6.5 may well be an artifact RFI, continuum ripple and/or solar interference. Here we explore the intergalactic emission in relation to the neighbouring galaxies.

University of Cape Town

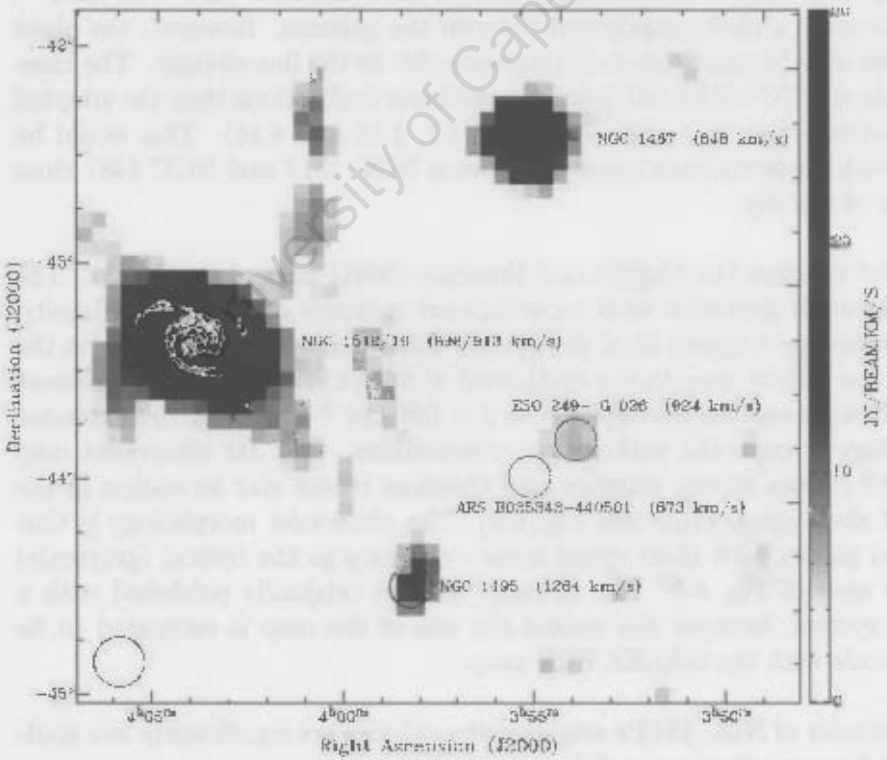

Figure 6.5: HIPASS map of NGC 1512 group with white superimposed contours of total intensity from ATCA observations (this study). The Parkes primary beam is displayed at the bottom left. See labels for galaxy identification and systemic velocities.

There appears to be emission to the south-west of NGC 1512, in a continuation of the Tidal Dwarf Galaxy candidate. This is suggestive of additional tidal material in the direction of NGC 1495, a galaxy of morphological type Sc? sp. There is also a continuation of the tidal material north-west of NGC 1512. This appears to extend in the rough direction of NGC 1487, a disrupted Peculiar galaxy with an HI mass $M_{\rm HI} = 1.1 \times 10^9$ M$_\odot$ (Koribalski et al., 2004).

NGC 1487 is the most well-studied of the neighbouring galaxies in Fig. 6.5. The angular separation between the *centres* of NGC 1512 and NGC 1487 is $\Delta\theta = 107'$. This corresponds to physical separation of 300 kpc at the distance of NGC 1487, $D = 9.5$ Mpc (Aguero and Paolantonio, 1997). NGC 1487 is a blue galaxy, B–V = 0.11 – 0.38, suggestive of ongoing star formation (Aguero and Paolantonio, 1997). This is confirmed by strong far ultraviolet emission as mapped by GALEX (see Fig. 6.7). Three nuclei are observed in the optical which lead Aguero & Paolantonio (1997) to the conclusion that it is the product of a merger of at least two late type galaxies. Mengel et al. (2008) find the age of these 'nuclei' to be ∼10 Myr. The small velocity difference between NGC 1512 and NGC 1487 ($\Delta V = 50$ km s^{-1}) does not advocate a likely interaction between the galaxies. However, the plane of interaction may be approximately perpendicular to the line-of-sight. The kinematic models of NGC 1512's full disk favoured lower inclinations than the adopted $i = 38.5°$ towards the outer radii (see Figs. 4.1, 4.15 and 4.16). This would be consistent with an interaction scenario between NGC 1512 and NGC 1487 close to the plane of the sky.

Figure 6.3 displays the English and Freeman (2001) map of NGC 1487. The optical is shown in grayscale with superimposed contours of HI column density. The HI morphology suggests tidal disruption, with two isolated HI clouds in the direction of the 'debris' seen to the north-west of NGC 1512. Note that the lowest HI column density contour corresponds to 2×10^{20} cm^{-2} and so a more extended HI morphology is expected with deeper observations. The far ultraviolet map of NGC 1487 reveals strong emission and therefore recent star formation in the nucleus and short spiral arms (see Fig. 6.7). The ultraviolet morphology is that of perturbed galaxy with short spiral arms – contrary to the optical (grayscale) morphology seen in Fig. 6.3. The HI map was not originally published with a co-ordinate system, however the spatial the size of the map is estimated to be roughly to scale with the GALEX FUV map.

The remainder of NGC 1512's neighbouring galaxies are significantly less studied. Table 6.3 summarises some of their properties.

The galaxies in the proximity of NGC 1512 are clearly part of a rich group.

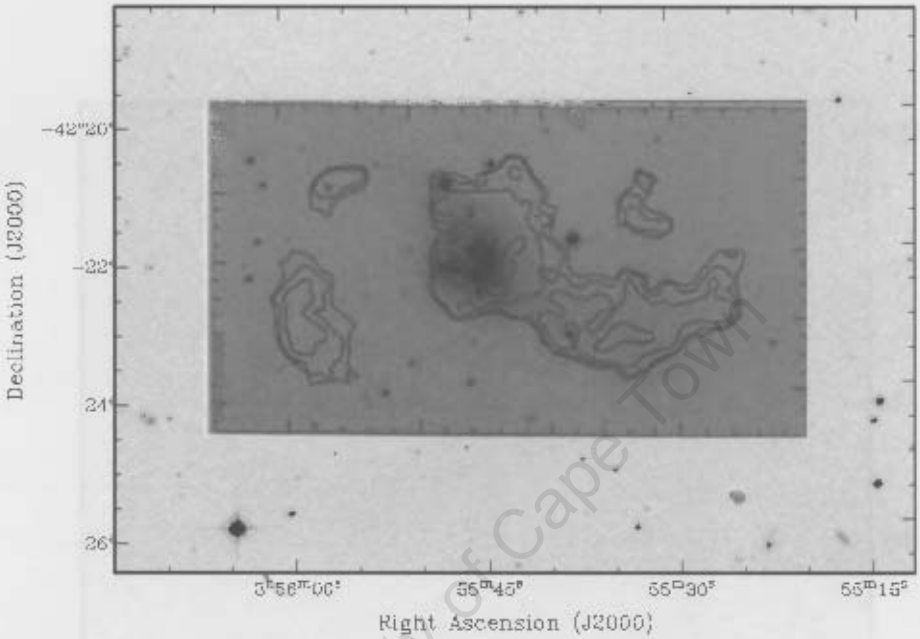

Figure 6.6: Copy of NGC 1487 map from English and Freeman (2001) (center). R band map (grayscale) with superimposed with HI column density contours. These levels are 2, 4, 6, 8 $\times$ 10^{20} cm^{-2}. The English and Freeman map is overlaid on a DSS R band map (by aligning bright stars) in order to view the spatial scale.

University of Cape Town

The morphology, gas distribution, star formation activity of some of these galaxies, combined with the intergalactic HI emission suggested by the HIPASS map are indicative of interactions, not necessarily with NGC 1512. These are speculations however and will be tested with deeper observations as outlined in the closing chapter.

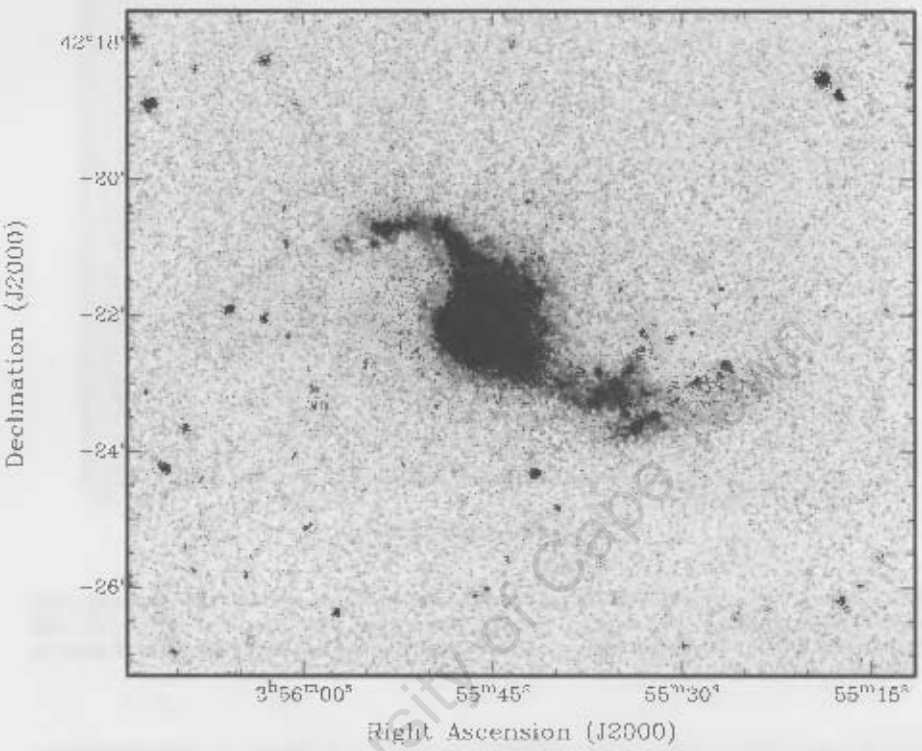

Figure 6.7: GALEX FUV map of NGC 1487. Note disrupted morphology.

University of Cape Town

Galaxy	RA h m s	Dec. ° ′ ″	Velocity km s^{-1}	Distance[1] Mpc	M_{HI} $M_{\odot}$	m_V mag	M_V[2] mag	Morphology
NGC 1512	04 03 54.3	-43 20 56	898	9.8±0.7	5×10^9	11.50	-18.45	SB(r)ab
NGC 1510	04 03 32.6	-43 24 00	913	10.0±0.7	-	13.02	-16.98	BCD/dE
NGC 1512 TDGc	04 02 36.5	-43 39 41	933	-	6.5×10^7	-	-	TDGc
NGC 1487	03 55 46.1	-42 22 05	848	9.5±0.6	1.1×10^8	11.83	-18.0	Peculiar
NGC 1495	03 58 21.8	-44 27 59	1284	14.9±1.0	9.4×10^8	12.64	-18.23	Sc? sp
ESO 249- G 026	03 54 12.9	-43 45 28	924	10.2±0.7	9.4×10^8	15.11	-14.93	S?
ARS B035343-440501	03 53 21.7	-43 36 19	873	9.5±0.7	-	16.40	-13.49	Sa

Table 6.1: Basic parameters of galaxies in Fig. 6.5. (1): Distances from NASA Extragalactic Database (Virgo Infall Only); (2) Absolute magnitude calculated from distances quoted in (1).

Chapter 7

Discussion and Conclusions

7.1 Summary of Results

The high resolution, multi-wavelength observations provide a substantially improved insight into the properties of NGC 1512. The ATCA HI map reveals a tidally disrupted, 100 kpc disk with detailed spiral structure far beyond the optical extent. The morphology is significantly different from that revealed by the single dish observations of Hawarden et al. (1979). The HI mass derived for the system is $M_{HI} = 5 \times 10^9$ M$_\odot$. This is comparable (within errorbars) to the Hawarden et al. calculation, adopting the Spergel et al. (2007) value of $H_0 = 73$ km s^{-1}. This HI mass is typical for a Sab galaxy (Roberts and Haynes, 1994), which perhaps confutes the view that this galaxy is part of the so-called class of giant LSBs. The adjusted Hawarden HI mass estimate is also close to the recent HIPASS measurement of 5.5×10^9 M$_\odot$.

The kinematic models show NGC 1512 has two distinct regions: a 'regularly rotating' inner disk and a tidally disrupted outer disk – consistent with the appearance of the HI map. The inner, regularly rotating disk has a dynamical mass of $M_{dyn} = 2.5 \times 10^{11}$ M$_\odot$, a value consistent, but at the high mass end of typical Sab galaxies (Roberts and Haynes, 1994). This implies a dynamical mass-to-light ratio $(M/L_B) = 86$ and a HI mass-to-light ratio $(M_{\rm HI}/L_B) = 1.7$. Both of these values lie at the very high end of their respective distributions compared with both 'normal' and giant LSB galaxies (O'Neil et al., 2004). The galaxy was found to be dark matter dominated at a radius of 27.5 kpc ($M_{dark}/M_{baryons} = 2.1$). This is lower than average when compared to 23 LSBs DM-to-baryon ($M_{dark}/M_{baryons}$) values determined by de Blok and McGaugh (1997b). Because of the degeneracy between the inclination and rotation velocity of the outermost radii, two models were derived. One assumes a flat rotation curve out to radii $R = 75$ kpc; the

other assumes constant inclination throughout the disk and applied the $i = 38.5°$ value derived for the inner disk. Both these models find the isolated HI disk to be roughly consistent in inclination and rotation velocity with the outer HI disk ($\pm 10°$ and ± 25 km s^{-1} respectively). This assumes that the HI cloud is in a circular orbit with NGC 1512.

The GALEX FUV map of NGC 1512 displays regions of massive star formation throughout the HI disk. The Spitzer 24 μm emission reveals a bright inner ring, however no obvious emission beyond the optical/near-infrared extent. This implies low dust content in the outer disk, consistent with the general properties of LSBs. The combination of the FUV and 24 μm provides a map optimised to trace star formation rate surface density in both dust obscured and dust free regions. The similar spatial resolutions of the FUV, 24 μm and HI maps enables the SFR-HI relation to be probed at sub-kpc (760 pc) scales – such analyses have only recently become possible thanks to the significant increase in high resolution, high quality data for nearby galaxies.

The comparison of the SFR surface density with HI surface density reveals two peaks in the Σ_{SFR}, separated by an order of magnitude in HI surface density. This is likely due to the core of NGC 1512 being dominated by molecular hydrogen. Besides these two peaks, there appears to be no obvious correlation between SFR and HI on local scales. Binning the pixels up into radial annuli reveals a significantly different view. A clear SFR threshold is seen at $\Sigma_{HI} \sim 2.5$ M$_\odot$ pc^{-2}.

There is a clear dependence of star formation efficiency with radius. A decreasing trend is seen from the nucleus to a galaxy radius of $1.2 \times R_{25}$. The Star Formation Efficiency in the proximity of the R_{25} radius is found to be $SFE \sim 1.2 \times 10^{-11}$ year^{-1}. This is a lower value than that derived for 8 spiral galaxies in a similar study by Leroy et al. (2008) and therefore appears consistent with the expectation for a low surface brightness disk. The SFE shows an increase towards the outermost radii. This is suggestive of external effects having a significant impact at these outer radii, given that the SFE is expected to decrease with the decrease in metallicity observed in the outer radii of galaxies (Searle, 1971).

One possibility for this increase in SFE may be previous galaxy interactions, certainly – but likely not only –with NGC 1510 whose relatively small local effect on SFE is seen at a radius of 14 kpc. A HIPASS map of the region illustrates that NGC 1512 is embedded in a rich galaxy group. The HI map suggests the existence of intergalactic gas, which could be the signatures of past interactions. This intergalactic emission is at a very low level and may well be a spurious data artifact.

An HI cloud of mass $M_{\rm HI} = 6.5 \times 10^7$ M$_\odot$ was discovered at a projected distance of 72 kpc from NGC 1512's centre. The cloud has no obvious optical/infrared counterpart. Low level far ultraviolet emission in the centre of the cloud, combined with a rough consistency in rotation velocity and inclination suggest that it may be of tidal origin.

The notion that NGC 1512 is a giant LSB is not supported by the HI mass determination from this study ($M_{\rm HI} = 5 \times 10^9$ M$_\odot$). This is lower than the average HI mass ($M_{\rm HI} = 6.1 \times 10^9$ M$_\odot$) determined for a sample of 80 '*normal*' LSBs by O'Neil et al. (2004). NGC 1512 is more likely a 'normal' LSB with a giant LSB morphology due to its minor interaction with NGC 1510 (other interactions cannot be considered at this point due to a lack of evidence).

This study supports current idea that giant LSBs are transient phenomena due to minor mergers and not quiescently evolving galaxies. Furthermore, the study indicates that a giant LSB morphology can be observed without the requirement that the galaxy need be substantially massive in HI.

The current evidence suggests that a minor merger with NGC 1510 has had a substantial influence on the morphology, star formation rate, and hence evolution of NGC 1512. This advocates current theories that minor interactions are of great importance through their role in the initiation of inside-out galaxy evolution (Thilker et al., 2007).

University of Cape Town

7.2 Future Prospects

The 12 month timescale of this project did not allow for a full analysis of all the high quality data products available for NGC 1512. There is a substantial scope for future research on this galaxy in a large range of wavelengths.

A wealth of high quality Spitzer infrared data of NGC 1512 is available from the SINGS Legacy programme. This includes imaging in the 3.6, 4.5, 5.8, 8.0, 24, 70, 160 μm wavelengths. Studies in the infrared enable the derivation of the dust mass and hence dust-to-gas ratio and its radial profile. The spatial distribution of the cold dust, which is in thermal equilibrium with the system (Dale et al., 2007), may provide further clues to the interaction scenario. This will enable a comparison with a study of the infrared properties of a sample of 3 giant LSBs (including Malin 1) also observed with the Spitzer Space Telescope (Rahman et al., 2007).

Deep near-infrared observations of the Tidal Dwarf Galaxy candidate have been made with the Infrared Survey Facility (IRSF)[1] in Sutherland, South Africa. The observations are as yet unprocessed due to corrupt file headers. The observations are aimed to search for a the presence of an old stellar component in the Tidal Dwarf Galaxy candidate. Further efforts will be made to reduce the data reliably, however, if this is unsuccessful the observations will be repeated.

The star formation analysis can be enhanced through high resolution H_2 measurements in the core of NGC 1512. Carbon Monoxide CO (1→0) observations trace molecular hydrogen (H_2) which dominates over HI in the central parts of the majority of galaxies. A CO map of comparable resolution would enable an investigation of the relationship between star formation and the density of both neutral and molecular hydrogen, allowing a more complete view of the galaxy in both HI and H_2 dominated regimes. This is particularly relevant as the strongest star formation occurs within the central core of NGC 1512, which is likely to be H_2 dominated. Comparable spatial resolutions ($\theta \sim 24$" at $\nu_{obs} = 115.27$ GHz) can be attained with the Mopra[2] millimetre telescope near Coonabarabran, Australia. A proposal will be submitted for such an observation in the 2009 winter season for favourable atmospheric conditions.

Perhaps the most promising method to probe the Tidal Dwarf Galaxy candidacy is to search for a low column density HI connection between the TDGc and NGC 1512. This connection cannot be probed by any single dish radio telescopes due to insufficient spatial resolution. Therefore, a proposal has been submitted to the ATCA for 12 hours in a compact configuration (H214). This will attain a sensitivity of $\sim 3.5 \times 10^{17}$ cm^{-2} per 3.5 km s^{-1} channel. A connection at this level will make a strong case that the HI cloud is indeed a Tidal Dwarf Galaxy, particularly if coupled with the ground-based near-infrared observations.

Finally, the HIPASS map of NGC 1512's extended environment reveals a rich galaxy group and includes suggestive low level intergalactic HI emission. Deeper single dish observations of the field will probe the fidelity of these intergalactic detections and perhaps bring new insight into previous interactions in this dense group of galaxies. A proposal has been submitted to investigate this in the October 2008 semester. Twenty five hours with the Parkes Radio Telescope in mapping mode will achieve a column density sensitivity of $\sim 5 \times 10^{16}$ per 1.6 km s^{-1} channel in the field shown in Fig. 6.5.

[1] *http://www.z.phys.nagoya-u.ac.jp/~telescop/index.html*
[2] *http://www.narrabri.atnf.csiro.au/mopra/*

University of Cape Town

These future multi-wavelength observations may provide a view on the history of NGC 1512 and the dense group within which it is embedded. A more detailed study of this group could be a prime example of the role of minor interactions on galaxy morphology, star formation and hence evolution.

University of Cape Town

Appendix A

Channel Maps

Channel maps of NGC 1512 at 16.9" resolution. Emission is masked based on criteria outlined in Sect. 2.2. The channels are averaged into 17.5 $\mathrm{km\,s^{-1}}$ bins. The central velocity of each of these bins is displayed at the top left of each channel map. HI column density contours are drawn at $N_{\mathrm{HI}} = 1, 3, 4, 5, 6, 7, 8, 10 \times 10^{20}$ $\mathrm{cm^{-2}}$

University of Cape Town

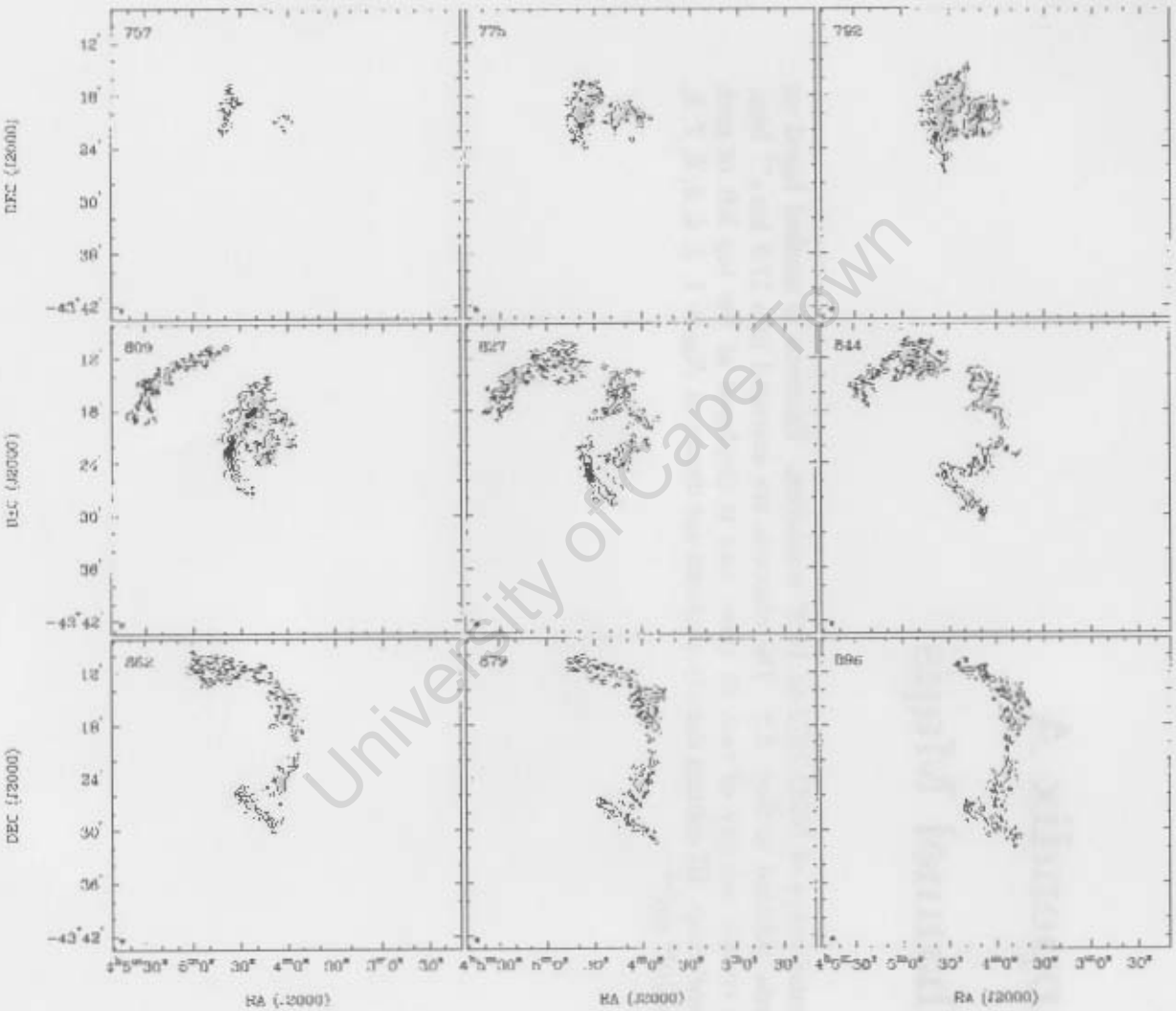

University of Cape Town

University of Cape Town

Bibliography

Aguero, E. L. and Paolantonio, S.: 1997, *Astronomical Journal* **114**, 102

Bagetakos, I., Brinks, E., Walter, F., and de Blok, E.: 2007, in B. G. Elmegreen and J. Palous (eds.), *IAU Symposium*, Vol. 237 of *IAU Symposium*, pp 393–393

Barnes, D. G., Staveley-Smith, L., de Blok, W. J. G., Oosterloo, T., Stewart, I. M., Wright, A. E., Banks, G. D., Bhathal, R., Boyce, P. J., Calabretta, M. R., Disney, M. J., Drinkwater, M. J., Ekers, R. D., Freeman, K. C., Gibson, B. K., Green, A. J., Haynes, R. F., te Lintel Hekkert, P., Henning, P. A., Jerjen, H., Juraszek, S., Kesteven, M. J., Kilborn, V. A., Knezek, P. M., Koribalski, B., Kraan-Korteweg, R. C., Malin, D. F., Marquarding, M., Minchin, R. F., Mould, J. R., Price, R. M., Putman, M. E., Ryder, S. D., Sadler, E. M., Schröder, A., Stootman, F., Webster, R. L., Wilson, W. E., and Ye, T.: 2001, *Monthly Notices of the Royal Astronomical Society* **322**, 486

Barth, A.: 2006, *The Astronomical Journal* **133**, 1085

Basilakos, S., Plionis, M., Kovač, K., and Voglis, N.: 2007, *Monthly Notices of the Royal Astronomical Society* **378**, 301

Bell, E. F. and de Jong, R. S.: 2001, *Astrophysical Journal* **550**, 212

Bigiel, F., Leroy, A., Walter, F., Brinks, E., de Blok, W., Madore, B., and Thornley, M.: 2008, *Astronomical Journal, submitted*

Binggeli, B., Sandage, A., and Tarenghi, M.: 1984, *Astronomical Journal* **89**, 64

Blitz, L., Spergel, D. N., Teuben, P. J., Hartmann, D., and Burton, W. B.: 1999, *Astrophysical Journal* **514**, 818

Bosma, A.: 1978, *Ph.D. thesis*, University of Groningen

University of Cape Town

Bothun, G., Impey, C., and Malin, D.: 1986, in *Bulletin of the American Astronomical Society*, Vol. 18 of *Bulletin of the American Astronomical Society*, pp 958–+

Bothun, G., Impey, C., and McGaugh, S.: 1997, *PASP* **109**, 745

Bothun, G. D., Geller, M. J., Kurtz, M. J., Huchra, J. P., and Schild, R. E.: 1992, *Astrophysical Journal* **395**, 347

Bothun, G. D., Impey, C. D., Malin, D. F., and Mould, J. R.: 1987, *Astronomical Journal* **94**, 23

Bothun, G. D., Schombert, J. M., Impey, C. D., Sprayberry, D., and McGaugh, S. S.: 1993, *Astronomical Journal* **106**, 530

Briggs, D. S.: 1995, in *Bulletin of the American Astronomical Society*, Vol. 27 of *Bulletin of the American Astronomical Society*, pp 1444–+

Brinks, E., Bagetakos, I., Walter, F., and de Blok, E.: 2007, in B. G. Elmegreen and J. Palous (eds.), *IAU Symposium*, Vol. 237 of *IAU Symposium*, pp 76–83

Broeils, A. H. and Rhee, M.-H.: 1997, *Astronomy and Astrophysics* **324**, 877

Calzetti, D.: 2008, *ArXiv e-prints* 801

Calzetti, D., Kennicutt, R. C., Engelbracht, C. W., Leitherer, C., Draine, B. T., Kewley, L., Moustakas, J., Sosey, M., Dale, D. A., Gordon, K. D., Helou, G. X., Hollenbach, D. J., Armus, L., Bendo, G., Bot, C., Buckalew, B., Jarrett, T., Li, A., Meyer, M., Murphy, E. J., Prescott, M., Regan, M. W., Rieke, G. H., Roussel, H., Sheth, K., Smith, J. D. T., Thornley, M. D., and Walter, F.: 2007, *Astrophysical Journal* **666**, 870

Casertano, S.: 1983, *Monthly Notices of the Royal Astronomical Society* **203**, 735

Dale, D. A., Gil de Paz, A., Gordon, K. D., Hanson, H. M., Armus, L., Bendo, G. J., Bianchi, L., Block, M., Boissier, S., Boselli, A., Buckalew, B. A., Buat, V., Burgarella, D., Calzetti, D., Cannon, J. M., Engelbracht, C. W., Helou, G., Hollenbach, D. J., Jarrett, T. H., Kennicutt, R. C., Leitherer, C., Li, A., Madore, B. F., Martin, D. C., Meyer, M. J., Murphy, E. J., Regan, M. W., Roussel, H., Smith, J. D. T., Sosey, M. L., Thilker, D. A., and Walter, F.: 2007, *Astrophysical Journal* **655**, 863

University of Cape Town

de Blok, W.: 1997, *Ph.D. thesis*, University of Groningen

de Blok, W., Walter, F., Brinks, E., Trachternach, C., Oh, S., and Kennicutt, R.: 2008, *Astrophysical Journal*

de Blok, W. J. G. and McGaugh, S. S.: 1997a, *Monthly Notices of the Royal Astronomical Society* **290**, 533

de Blok, W. J. G. and McGaugh, S. S.: 1997b, *Monthly Notices of the Royal Astronomical Society* **290**, 533

de Blok, W. J. G. and van der Hulst, J. M.: 1998, *Astronomy and Astrophysics* **336**, 49

Disney, M. J.: 1976, *Nature* **263**, 573

Disney, M. J. and Pottasch, S. R.: 1977, *Astronomy and Astrophysics* **60**, 43

Donas, J., Deharveng, J. M., Laget, M., Milliard, B., and Huguenin, D.: 1987, *Astronomy and Astrophysics* **180**, 12

D'Onghia, E., Burkert, A., Murante, G., and Khochfar, S.: 2006, *Monthly Notices of the Royal Astronomical Society* **372**, 1525

Eichendorf, W. and Nieto, J.-L.: 1984, *Astronomy and Astrophysics* **132**, 342

English, J. and Freeman, K. C.: 2001, in J. E. Hibbard, M. Rupen, and J. H. van Gorkom (eds.), *Gas and Galaxy Evolution*, Vol. 240 of *Astronomical Society of the Pacific Conference Series*, pp 858–+

Feretti, L. and Venturi, T.: 2002, in L. Feretti, I. M. Gioia, and G. Giovannini (eds.), *Merging Processes in Galaxy Clusters*, Vol. 272 of *Astrophysics and Space Science Library*, pp 163–195

Gil de Paz, A., Boissier, S., Madore, B. F., Seibert, M., Joe, Y. H., Boselli, A., Wyder, T. K., Thilker, D., Bianchi, L., Rey, S.-C., Rich, R. M., Barlow, T. A., Conrow, T., Forster, K., Friedman, P. G., Martin, D. C., Morrissey, P., Neff, S. G., Schiminovich, D., Small, T., Donas, J., Heckman, T. M., Lee, Y.-W., Milliard, B., Szalay, A. S., and Yi, S.: 2007, *Astrophysics Journal Supplement* **173**, 185

Goldsmith, P. F., Li, D., and Krčo, M.: 2007, *Astrophysical Journal* **654**, 273

University of Cape Town

Gordon, K. D., Pérez-González, P. G., Misselt, K. A., Murphy, E. J., Bendo, G. J., Walter, F., Thornley, M. D., Kennicutt, Jr., R. C., Rieke, G. H., Engelbracht, C. W., Smith, J.-D. T., Alonso-Herrero, A., Appleton, P. N., Calzetti, D., Dale, D. A., Draine, B. T., Frayer, D. T., Helou, G., Hinz, J. L., Hines, D. C., Kelly, D. M., Morrison, J. E., Muzerolle, J., Regan, M. W., Stansberry, J. A., Stolovy, S. R., Storrie-Lombardi, L. J., Su, K. Y. L., and Young, E. T.: 2004, *Astrophysical Journal Supplement* **154**, 215

Hawarden, T., van Woerden, H., mebold, U., Goss, W., and Peterson, B.: 1979, *Astronomy and Astrophysics* **76**, 230

Helfer, T., Thornley, M., Regan, M., Wong, T., Sheth, K., Vogel, S., Blitz, L., and Bock, D.-J.: 2003, *ApJS* **145**, 259

Hickson, P.: 1999, in J. E. Barnes and D. B. Sanders (eds.), *Galaxy Interactions at Low and High Redshift*, Vol. 186 of *IAU Symposium*, pp 367–+

Hogeveen, S. J.: 1990, *Concept of a LaTeX style package for the Astronomy and Astrophysics publications*, Technical report, Astronomical Institute 'Anton Pannekoek', Amsterdam

Holdaway, M. and Helfer, T.: 1999, *ASP Conference Series* **180**, 537

Impey, C. and Bothun, G.: 1989, *Astrophysical Journal* **341**, 89

Impey, C. and Bothun, G.: 1997, *Annual Review of Astronomy and Astrophysics* **35**, 267

Impey, C. D., Sprayberry, D., Irwin, M. J., and Bothun, G. D.: 1996, *Astrophysics Journal Supplement* **105**, 209

Jarrett, T. H., Chester, T., Cutri, R., Schneider, S. E., and Huchra, J. P.: 2003, *Astronomical Journal* **125**, 525

Jones, C. and Forman, W.: 1990, *Advances in Space Research* **10**, 209

Kennicutt, R. C., Bendo, G., Engelbracht, C., Gordon, K., Li, A., Rieke, G. H., Rieke, M. J., Smith, J. D., Armus, L., Helou, G., Jarrett, T. H., Roussel, H., Calzetti, D., Leitherer, C., Malhotra, S., Meyer, M., Regan, M. W., Dale, D. A., Draine, B., Grauer, A. D., Hollenbach, D. J., Kewley, L. J., Murphy, E., Thornley, M. D., and Walter, F.: 2003, in *Bulletin of the American Astronomical Society*, Vol. 35 of *Bulletin of the American Astronomical Society*, pp 1351–+

University of Cape Town

Kennicutt, Jr., R. C.: 1998, *Astrophysical Journal* **498**, 541

Kennicutt, Jr., R. C.: 2008, in R.-R. Chary, H. I. Teplitz, and K. Sheth (eds.), *Infrared Diagnostics of Galaxy Evolution*, Vol. 381 of *Astronomical Society of the Pacific Conference Series*, pp 103–+

Kim, S., Rosolowsky, E., Lee, Y., Kim, Y., Jung, Y. C., Dopita, M. A., Elmegreen, B. G., Freeman, K. C., Sault, R. J., Kesteven, M., McConnell, D., and Chu, Y.-H.: 2007, *Astrophysics Journal Supplement* **171**, 419

Kinman, T. D.: 1978, *Astronomical Journal* **83**, 764

Knezek, P.: 1993, *Ph.D. thesis*, University of Masschusetts

Knezek, P.: 1999, in J. I. Davies, C. Impey, and S. Phillips (eds.), *The Low Surface Brightness Universe*, Vol. 170 of *Astronomical Society of the Pacific Conference Series*, pp 191–+

Koribalski, B. S., Staveley-Smith, L., Kilborn, V. A., Ryder, S. D., Kraan-Korteweg, R. C., Ryan-Weber, E. V., Ekers, R. D., Jerjen, H., Henning, P. A., Putman, M. E., Zwaan, M. A., de Blok, W. J. G., Calabretta, M. R., Disney, M. J., Minchin, R. F., Bhathal, R., Boyce, P. J., Drinkwater, M. J., Freeman, K. C., Gibson, B. K., Green, A. J., Haynes, R. F., Juraszek, S., Kesteven, M. J., Knezek, P. M., Mader, S., Marquarding, M., Meyer, M., Mould, J. R., Oosterloo, T., O'Brien, J., Price, R. M., Sadler, E. M., Schröder, A., Stewart, I. M., Stootman, F., Waugh, M., Warren, B. E., Webster, R. L., and Wright, A. E.: 2004, *Astronomical Journal* **128**, 16

Kroupa, P.: 2001, *Monthly Notices of the Royal Astronomical Society* **322**, 231

Leroy, A., Bigiel, F., Walter, F., Brinks, E., de Blok, W. J. G., and Madore, B.: 2008, in H. Beuther, H. Linz, and T. Henning (eds.), *Massive Star Formation: Observations Confront Theory*, Vol. 387 of *Astronomical Society of the Pacific Conference Series*, pp 408–+

McGaugh, S. and Bothun, G.: 1994, *The Astronomical Journal* **107**, 530

McGaugh, S. S., Schombert, J. M., Bothun, G. D., and de Blok, W. J. G.: 2000, *Astrophysics Journal Letter* **533**, L99

Mengel, S., Lehnert, M. D., Thatte, N. A., Vacca, W. D., Whitmore, B., and Chandar, R.: 2008, *ArXiv e-prints* 805

University of Cape Town

Meyer, M. J., Zwaan, M. A., Webster, R. L., Staveley-Smith, L., Ryan-Weber, E., Drinkwater, M. J., Barnes, D. G., Howlett, M., Kilborn, V. A., Stevens, J., Waugh, M., Pierce, M. J., Bhathal, R., de Blok, W. J. G., Disney, M. J., Ekers, R. D., Freeman, K. C., Garcia, D. A., Gibson, B. K., Harnett, J., Henning, P. A., Jerjen, H., Kesteven, M. J., Knezek, P. M., Koribalski, B. S., Mader, S., Marquarding, M., Minchin, R. F., O'Brien, J., Oosterloo, T., Price, R. M., Putman, M. E., Ryder, S. D., Sadler, E. M., Stewart, I. M., Stootman, F., and Wright, A. E.: 2004, *Monthly Notices of the Royal Astronomical Society* **350(4)**, 1195

Mo, H. J., McGaugh, S. S., and Bothun, G. D.: 1994, *Monthly Notices of the Royal Astronomical Society* **267**, 129

Moore, B., Ghigna, S., Governato, F., Lake, G., Quinn, T., Stadel, J., and Tozzi, P.: 1999, *Astrophysical Journal* **524**, L19

Morganti, R., Oosterloo, T., Tadhunter, C., and Emonts, B.: 2003, *"New Astronomy Review"* **47**, 273

Navarro, J. F., Frenk, C. S., and White, S. D. M.: 1996, *Astrophysical Journal* **462**, 563

Oey, M. S.: 2002, in A. R. Taylor, T. L. Landecker, and A. G. Willis (eds.), *Seeing Through the Dust: The Detection of HI and the Exploration of the ISM in Galaxies*, Vol. 276 of *Astronomical Society of the Pacific Conference Series*, pp 295–+

Oh, S.-H., de Blok, W., Brinks, E., and Walter, F.: 2008, *submitted*

O'Neil, K., Bothun, G., Cornell, M., and Impey, C.: 1997, *The Astronomical Journal*

O'Neil, K., Bothun, G., van Driel, W., and Monnier Ragaigne, D.: 2004, *Astronomy and Astrophysics* **428**, 823

O'Neil, K., Bothun, G. D., Schombert, J., Cornell, M. E., and Impey, C. D.: 1997, *Astronomical Journal* **114**, 2448

Pickering, T., Impey, C., van Gorkom, J., and Bothun, G.: 1997, *The Astronomical Journal* **114**, 1858

University of Cape Town

Rahman, N., Howell, J. H., Helou, G., Mazzarella, J. M., and Buckalew, B.: 2007, *Astrophysical Journal* **663**, 908

Rieke, G. H. and MIPS Team: 2004, in *Bulletin of the American Astronomical Society*, Vol. 36 of *Bulletin of the American Astronomical Society*, pp 700–+

Roberts, M. S. and Haynes, M. P.: 1994, *Annual Review of Astronomy and Astrophysics* **32**, 115

Rubin, V. C., Thonnard, N., and Ford, Jr., W. K.: 1978, *Astrophysics Journal Letter* **225**, L107

Salim, S., Rich, R. M., Charlot, S., Brinchmann, J., Johnson, B. D., Schiminovich, D., Seibert, M., Mallery, R., Heckman, T. M., Forster, K., Friedman, P. G., Martin, D. C., Morrissey, P., Neff, S. G., Small, T., Wyder, T. K., Bianchi, L., Donas, J., Lee, Y.-W., Madore, B. F., Milliard, B., Szalay, A. S., Welsh, B. Y., and Yi, S. K.: 2007, *Astrophysics Journal Supplement* **173**, 267

Sandage, A., Binggeli, B., and Tammann, G. A.: 1985, in O.-G. Richter and B. Binggeli (eds.), *ESO Workshop on the Virgo Cluster*, pp 239–293

Sault, R. J., Staveley-Smith, L., and Brouw, W. N.: 1996, *Astronomy and Astrophysics Supplement* **120**, 375

Schmidt, M.: 1959, *Astrophysical Journal* **129**, 243

Schombert, J., Bothun, G., Impey, C., and Mundy, L.: 1990, *The Astronomical Journal* **100**, 1523

Schombert, J. M., Bothun, G. D., Schneider, S. E., and McGaugh, S. S.: 1992, *Astronomical Journal* **103**, 1107

Schulmann, E., Bregman, J., and Roberts, M.: 1994, *The Astrophysical Journal* **423**, 180

Searle, L.: 1971, *Astrophysical Journal* **168**, 327

Spergel, D. N., Bean, R., Doré, O., Nolta, M. R., Bennett, C. L., Dunkley, J., Hinshaw, G., Jarosik, N., Komatsu, E., Page, L., Peiris, H. V., Verde, L., Halpern, M., Hill, R. S., Kogut, A., Limon, M., Meyer, S. S., Odegard, N., Tucker, G. S., Weiland, J. L., Wollack, E., and Wright, E. L.: 2007, *Astrophysics Journal Supplement* **170**, 377

University of Cape Town

Sprayberry, D., Impey, C. D., Bothun, G. D., and Irwin, M. J.: 1995, *Astronomical Journal* **109**, 558

Steer, D. G., Dewdney, P. E., and Ito, M. R.: 1984, *Astronomy and Astrophysics* **137**, 159

Thilker, D. A., Bianchi, L., Meurer, G., Gil de Paz, A., Boissier, S., Madore, B. F., Boselli, A., Ferguson, A. M. N., Muñoz-Mateos, J. C., Madsen, G. J., Hameed, S., Overzier, R. A., Forster, K., Friedman, P. G., Martin, D. C., Morrissey, P., Neff, S. G., Schiminovich, D., Seibert, M., Small, T., Wyder, T. K., Donas, J., Heckman, T. M., Lee, Y.-W., Milliard, B., Rich, R. M., Szalay, A. S., Welsh, B. Y., and Yi, S. K.: 2007, *Astrophysics Journal Supplement* **173**, 538

Thompson, A. R.: 1999, in G. B. Taylor, C. L. Carilli, and R. A. Perley (eds.), *Synthesis Imaging in Radio Astronomy II*, Vol. 180 of *Astronomical Society of the Pacific Conference Series*, pp 11–+

Trachternach, C., de Blok, W., Brink, E., and Walter, F.: 2008, *Astrophysical Journal*

van Albada, T. S. and Sancisi, R.: 1986, *Royal Society of London Philosophical Transactions Series A* **320**, 447

van der Kruit, P. C. and Searle, L.: 1981a, *Astronomy and Astrophysics* **95**, 105

van der Kruit, P. C. and Searle, L.: 1981b, *Astronomy and Astrophysics* **95**, 116

Walter, Brinks, and Kennicutt: 2008, *Astrophysical Journal* **70**, 100

Walter, F., Cannon, J. M., Roussel, H., Bendo, G. J., Calzetti, D., Dale, D. A., Draine, B. T., Helou, G., Kennicutt, Jr., R. C., Moustakas, J., Rieke, G. H., Armus, L., Engelbracht, C. W., Gordon, K., Hollenbach, D. J., Lee, J., Li, A., Meyer, M. J., Murphy, E. J., Regan, M. W., Smith, J.-D. T., Brinks, E., de Blok, W. J. G., Bigiel, F., and Thornley, M. D.: 2007, *Astrophysical Journal* **661**, 102

Willner, S. P., Ashby, M. L. N., Barmby, P., Fazio, G. G., Pahre, M., Smith, H. A., Kennicutt, Jr., R. C., Calzetti, D., Dale, D. A., Draine, B. T., Regan, M. W., Malhotra, S., Thornley, M. D., Appleton, P. N., Frayer, D., Helou, G., Stolovy, S., and Storrie-Lombardi, L.: 2004, *Astrophysics Journal Supplement* **154**, 222

University of Cape Town

Wrobel, J. and Walker, R.: 1999, *ASP Conference Series* **180**, 171

Wrobel, J. M. and Walker, R. C.: 1999, in G. B. Taylor, C. L. Carilli, and R. A. Perley (eds.), *Synthesis Imaging in Radio Astronomy II*, Vol. 180 of *Astronomical Society of the Pacific Conference Series*, pp 171–+

Wyder, T. K., Martin, D. C., Schiminovich, D., Seibert, M., Budavári, T., Treyer, M. A., Barlow, T. A., Forster, K., Friedman, P. G., Morrissey, P., Neff, S. G., Small, T., Bianchi, L., Donas, J., Heckman, T. M., Lee, Y.-W., Madore, B. F., Milliard, B., Rich, R. M., Szalay, A. S., Welsh, B. Y., and Yi, S. K.: 2007, *Astrophysics Journal Supplement* **173**, 293

Yun, M. S., Ho, P. T. P., and Lo, K. Y.: 1994, *Nature* **372**, 530

Zwaan, M. A., van der Hulst, J. M., de Blok, W. J. G., and McGaugh, S. S.: 1995, *Monthly Notices of the Royal Astronomical Society* **273**, L35

Zwicky, F.: 1937, *Astrophysical Journal* **86**, 217

University of Cape Town

Wrobel, J. and Walker, R.: 1999, *ASP Conference Series* **180**, 171

Wrobel, J. M. and Walker, R. C.: 1999, in G. B. Taylor, C. L. Carilli, and R. A. Perley (eds.), *Synthesis Imaging in Radio Astronomy II*, Vol. 180 of *Astronomical Society of the Pacific Conference Series*, pp 171–+

Wyder, T. K., Martin, D. C., Schiminovich, D., Seibert, M., Budavári, T., Treyer, M. A., Barlow, T. A., Forster, K., Friedman, P. G., Morrissey, P., Neff, S. G., Small, T., Bianchi, L., Donas, J., Heckman, T. M., Lee, Y.-W., Madore, B. F., Milliard, B., Rich, R. M., Szalay, A. S., Welsh, B. Y., and Yi, S. K.: 2007, *Astrophysics Journal Supplement* **173**, 293

Yun, M. S., Ho, P. T. P., and Lo, K. Y.: 1994, *Nature* **372**, 530

Zwaan, M. A., van der Hulst, J. M., de Blok, W. J. G., and McGaugh, S. S.: 1995, *Monthly Notices of the Royal Astronomical Society* **273**, L35

Zwicky, F.: 1937, *Astrophysical Journal* **86**, 217

University of Cape Town